AdVanced Aerodynamic Tools for lArge Rotors

Effects of rotational speed on performance and loads

G. Sieros (Ed), NTUA

June 30, 2017

Agreement n.:	FP7-ENERGY-2013-1 / n^o 608396
Duration:	November 2013 to November 2017
Coordinator:	ECN Wind Energy, Petten, The Netherlands

supported by:

This project has received funding from the European Union's Seventh Programme for research, technological development and demonstration under grand agreement No FP7-ENERGY-2013-1/n° 608396

AdVanced Aerodynamic Tools for lArge Rotors

Document Information

Document Name:	D4.11 Effects of rotational speed on performance and loads
Confidentiality Class:	PU
Document Number:	D4.11
Editor:	Giorgos Sieros (NTUA)
Contributions:	Néstor Ramos Garcia, Rasmus Monk Holm (DTU), Petros Chasapogiannis, Alkis Milidis (NTUA), Marion Reijierk, Thierry Maeder (GE)
Review:	Spyros Voutsinas (NTUA)
Date:	June 30, 2017
WP:	WP4 Aeroelastic Analysis of Large and Flexible Blades
Task:	Task 4.3: Parametric Study on the effect of critical parameters

AdVanced Aerodynamic Tools for lArge Rotors

Table of contents

List of Figures

List of Tables

Acronyms

AVATAR AdVanced Aerodynamic Tools for lArge Rotors.

BEM Blade Element Momentum.

C_P Power Coefficient.

C_T Rotor Thrust Coefficient.

ETM Extreme Turbulence Model.

GAST General Aerodynamic and Structural Tool.

GENUVP GENeral Unsteady Vortex Particle code.

HAWC2 Horizontal Axis Wind turbine simulation Code 2nd generation.

hGAST GAST with additional capabilities in hydro-servo-aero-elastic simulations.

LIR Low Induction Rotor.

MIRAS Method for Interactive Rotor Aerodynamic Simulations.

NTM Normal Turbulence Model.

RWT Reference Wind Turbine.

TSR Tip Speed Ratio – λ.

1 Introduction

In the context of Task 4.3, a series of parametric studies are performed, in order to investigate the performance sensitivity on different design parameters. In the present deliverable, the effect of rotational speed on rotor performance and loading is studied.

Two variants of the AVATAR RWT (Reference Wind Turbine) are further considered, namely the “high-speed” rotor, with a speed increased by 10 % to 10.57 RPM at rated conditions, and the “low-speed” rotor with a speed decreased to 8.64 RPM at rated conditions. The three rotors have the same nominal power diameter and therefore power density ($s = 300\,\mathrm{W/m^2}$).

We initially present the design choices for the two rotors and then proceed to the presentation of the methods used for the evaluation and the relevant results. In this deliverable code comparison is not a main target, as we are mostly interested in finding the effect of design choices on the performance and loads.

2 Design Parameters

The purpose of the parametric study is to isolate the effect of rotational speed, as much as possible. Therefore a series of constraints have been imposed, in order to make the resulting blades comparable to the reference blade.

- Design power is retained
- The turbine loading remains at similar levels (bending moment at the hub, overall thrust)
- The loading of the blades remains at similar levels along their span. This last constraint is used in order to have similar design conditions. Using this constraint the resulting planform is as shown in fig. 1, where a larger chord is used for the low-speed rotor.

The high- and low- speed aerodynamic designs have been obtained with the following procedure. In a first step we define the design TSR (Tip Speed Ratio – λ) assuming that the design wind speed of the AVATAR RWT is retained. For the current parametric study we have chosen to use a $\pm 10\,\%$ variation, resulting in the main characteristics listed in Table 1.

	Reference	Low Speed	High Speed
RPM	9.60	8.64	10.56
Tip Speed [m/s]	103	113	93

Table 1: Design parameters for high and low speed variations of the AVATAR rotor

The theoretical background is given in A. In short, using the corresponding TSR value we calculate from Eq. A.9 the induction level a that maintains the aerodynamic out-of-plane root bending moment of the reference blade. Using a and λ we then define the distribution of the non-dimensional lift $\Lambda(a, \lambda, x)$ and the flow angle $\varphi(a, \lambda, x)$ from Eqs. A.5 and A.6. Retaining the design lift coefficient distribution along the blade span we obtain the corresponding chord distribution from the definition of Λ. The actual chord and twist distributions are slightly different, so as to retain the necessary similarity to the reference blade.

The next step was to modify the structural properties for every variant. For the structural adaptation of the blades their properties were chosen so as to provide similar non-dimensional (with respect to the rated rotational speed) eigenfrequencies to the reference blade. There is no actual design of the blade internal structure at this step. This means that the resulting weight and stiffness combination is based on simple scaling rules, combined with the experience gained from the reference blade design. We *assume* that:

- The high speed rotor, where a stiffer blade is required, will probably utilise larger amounts of carbon, resulting in a stiffer and lighter construction.
- The low-speed rotor, where we need to lower the eigenfrequencies, will utilise more glass, resulting in a heavier construction.

The intention of this modification is to retain the stability characteristics of the reference wind turbine, as seen in fig. 2. This means that we need to lower the eigenfrequencies of the low-speed rotor and increase the ones of the high-speed rotor, so that their relation to the wind turbine rotating speed remains the same. An iterative modification of these quantities was performed

to ensure the appropriate placement of the 1st flap natural frequency. The main characteristics of the resulting blades are plotted in fig 2

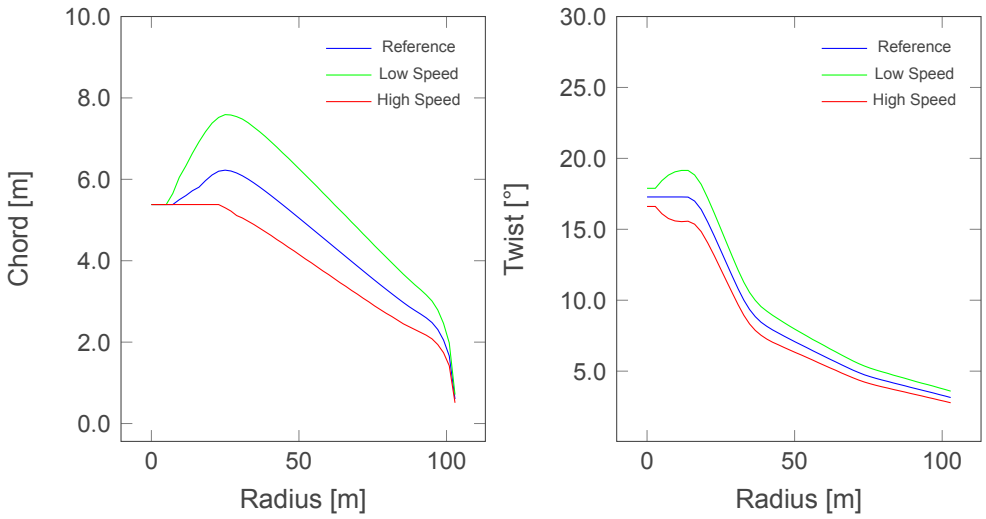

Figure 1: Chord and twist compared to the reference rotor

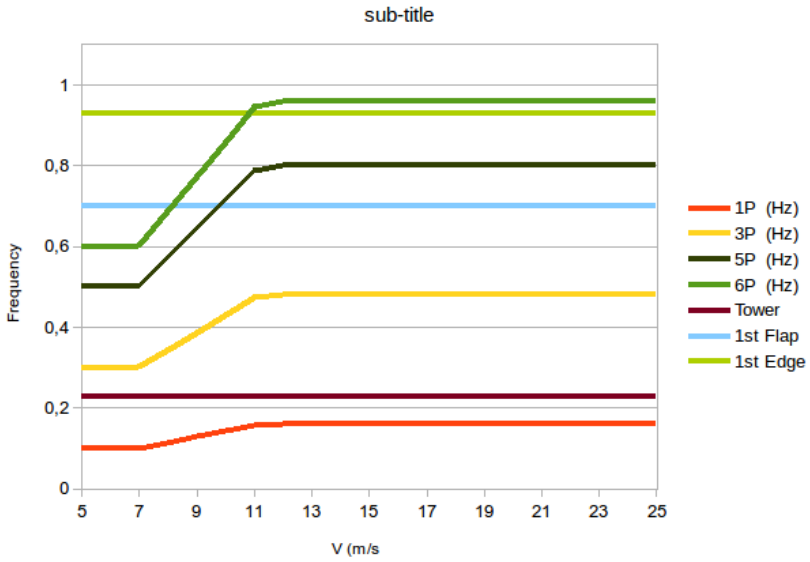

Figure 2: Eigenfrequency distribution for the reference rotor

The schedule for the operation of the modified rotors is shown in figs. 4 to 5. The power curve is practically the same for all three variations of the rotor, with the tip speed ratio shifted to higher and lower values.

Finally, in order to be able to evaluate the dynamic behaviour of the resulting designs, the controller parameters must be updated, based on the new design conditions. The controller that is implemented is described in [1], while the basic changes for the AVATAR rotor are described in [2]. The additional changes that were needed here include

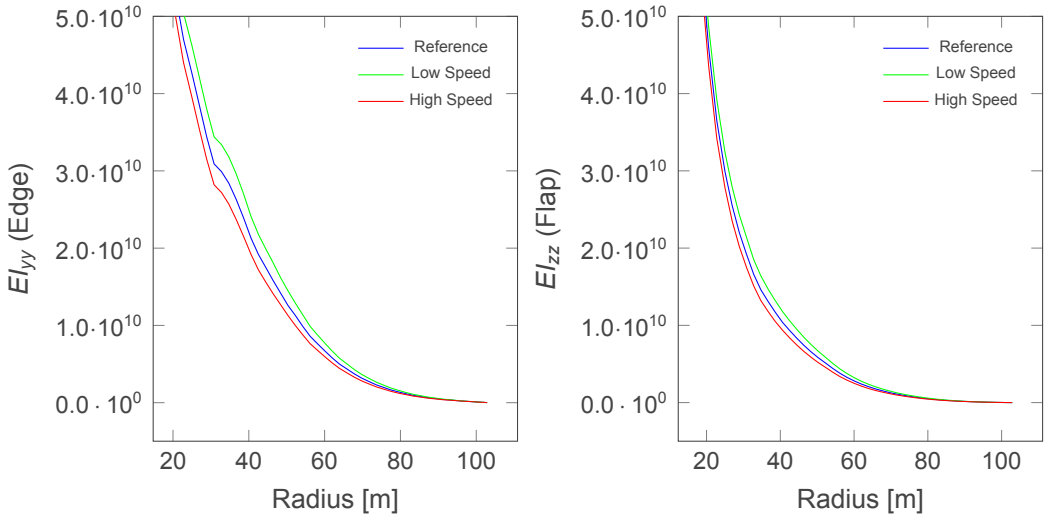

Figure 3: Flapwise and Edgewise stiffness compared to the reference rotor

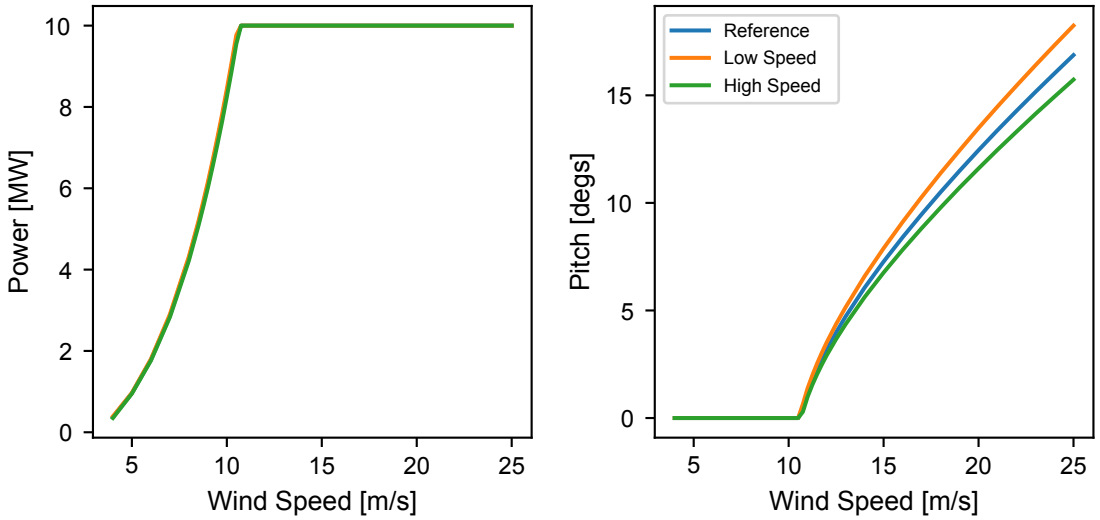

Figure 4: Power and pitch variation for the low- and high-speed rotors, compared to the reference design

- Modification of the minimum and maximum allowed rotor speed, to be compatible with the new operating regime
- Modification of the maximum allowable generator torque
- Modification of the C_P tracking factor k, which defines the desired C_P below rated conditions, based on the definition

$$k = \eta \frac{1}{2} \rho A C_{P_{des}} \frac{R^3}{\lambda^3} \tag{1}$$

For a proper tuning of the controller, the Proportional and Integral gains of the torque controller should also be adjusted to the new blade characteristics, but it was assumed that the required changes would be relatively small. A detailed list of the parameters that were employed is given

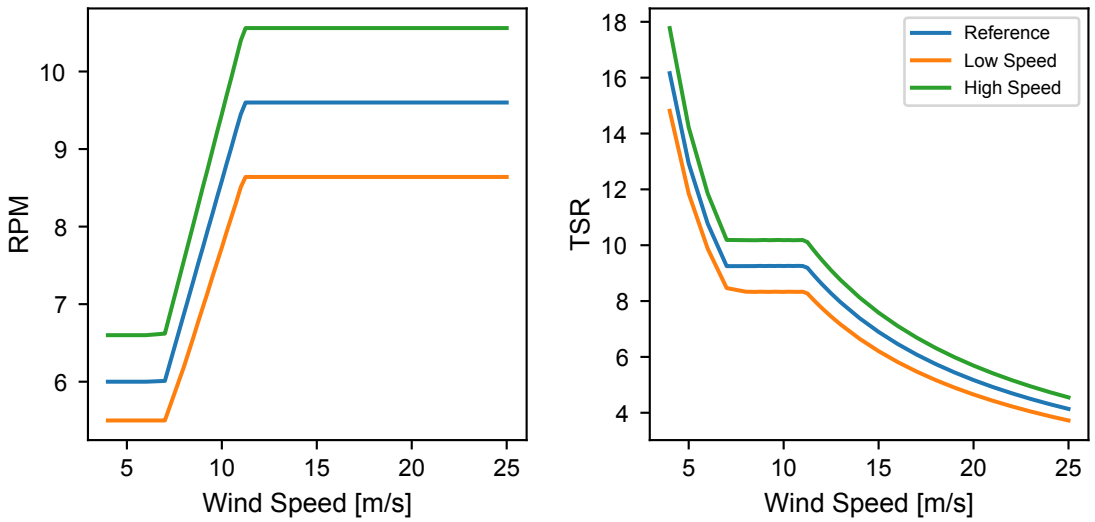

Figure 5: RPM and TSR variation for the low- and high-speed rotors, compared to the reference design in appendix B

3 Methodology

The evaluation of the changes was performed using aeroelastic simulations, provided by three partners, using four different codes. All of the codes provide loads and displacements at the required points for the provided input wind time series. The description of the codes used is given in the following.

3.1 DTU aeroelastic simulations

The simulations performed by DTU are based on variations of the HAWC2 (Horizontal Axis Wind turbine simulation Code 2nd generation) code, which has been developed at Risø National Laboratory of Denmark (now DTU Wind Energy) over the last more than 10 years. The structural part of the code is a multi-body formulation based on the floating frame of reference method as described in [3, 4]. In the particular formulation of the code, the turbine structure is subdivided into a number of bodies where each body has its own coordinate system. Within each body, the structure consists of an assembly of linear Timoshenko beam elements. The non-linear effects of the body motion (rotations and deformations) are accounted for in the coupling constraints in between the individual bodies, ensuring small deflections within the linear beam elements. This means that effects of large rotations and deflections are included using a proper subdivision of a blade to a number of bodies. The suggested method has been validated with another existing non-linear multi-body formulation with the classical spin-up manoeuvre example [3]. The aerodynamic part of the code is based on the BEM (Blade Element Momentum) theory, however is implemented in a way that is comparable with an actuator disc. It means that the BEM equation at each time step is evaluated in a number of so-called grid points over the rotor disc and not on an annular element with one single value of the induction factor over that element. The present approach was chosen to improve accuracy in cases with non-uniform loading over the rotor disc [5] as caused by wind shear and half wake operation.

Dynamic inflow, dynamic stall and skew inflow effects are simulated by sub-models. The dynamic stall model [6] consists of a modified Beddoes–Leishman model [7] that includes the effects from shed vorticity from the trailing edge [8] and the effects of stall separation lag caused by an instationary trailing edge separation point. Additional corrections are used for sheared flow [5] and rotors with substantial cone and/or tilt [9]

The yaw model in HAWC2 has two main components as originally proposed by Glauert [10], namely a correction of the mean axial induction for skewed inflow and an azimuthal correction of induced velocity. Details about the implementation of the yaw model are given in [11].

For a higher fidelity simulation, the in-house solver MIRAS (Method for Interactive Rotor Aerodynamic Simulations) has been employed to simulate the rotors. The MIRAS solver has been recently developed and extensively validated for small and medium size wind turbine rotors in [12, 13]. Due to its young age the solver is under a continuous process of improvement.

MIRAS is a computational model for predicting the aerodynamic behavior of wind turbine wakes and blades subjected to unsteady motions and viscous effects. The solver is based on a three-dimensional panel method using a surface distribution of quadrilateral sources and doublets to model the wind turbine geometry. Viscous and rotational effects inside the boundary layer are taken into account via the transpiration velocity concept, which is applied using a strip theory

approach with the cross sectional angle of attack as coupling parameter. The transpiration velocity is obtained from the solution of the integral boundary layer equations, which in the present version of the code is externally calculated by using the viscous-inviscid solver Q^3UIC [12]

The required input data for MIRAS simulations are: blade geometry, incoming wind speed, tip speed ratio, type of transition (free or forced transition) and the transition location in case of forced transition.

A free wake model is used to simulate the wake behind the wind turbine by releasing at the trailing edge of the blades a set of vortex filaments that carry on the trailing and shed vorticity. A large variety of time stepping schemes have been implemented in MIRAS for the wake update (PCC, PC2B, ABM4, etc.). However as a first approach, a simple Euler method has been used in the present simulations.

A surface mesh consisting of 21 span-wise cells and 150 chord-wise cells has been employed in the present computations, with 20 wake revolutions simulated with an azimuthal discretization of 10 degrees.

For the transitional simulations, the e^N envelope transition method with Mack's modification to account for the turbulent intensity has been employed [14]. In the present simulations the turbulent intensity has been set to 0.1% of the free stream.

Stability calculations are performed with HAWCStab2, a tool developed at DTU Wind Energy. HAWCStab2 is an improved version of HAWCStab [15] with a different kinematic model. The model is an analytical linearisation of a non-linear finite beam element model. The beam model is coupled with an unsteady blade element momentum model of the blade aerodynamic. The aerodynamic model includes shed vorticity, dynamic stall, and dynamic inflow [16]. A validation and analysis of the open-loop performances are provided by Sønderby and Hansen [17] for a version of HAWCStab2 without the present dynamic inflow model. A description of the linearised controller implemented in HAWCStab2 is provided by Tibaldi et al. [18].

3.2 NTUA aeroelastic simulations

NTUA is using the hGAST (GAST with additional capabilities in hydro-servo-aero-elastic simulations) simulation platform in its version for land based wind turbines. hGAST is a hydro-servo-aero-elastic time domain solver for the fully coupled wind turbine system [19]. For the structural part, a multi-body formulation is applied combined with a sub-body Timoshenko beam model.

For the aerodynamic part two options are considered:

1) A BEM model, accounting for dynamic inflow conditions based on the ONERA model. It follows the usual guidelines of BEM modelling and contains tip and/or hub losses, 3D correction of the 2D polars (if not included already in the tables) and yaw misalignment corrections. Dynamic induction modelling is employed solving the momentum equations separately for each blade.
2) A free-wake 3D model, GENUVP (GENeral Unsteady Vortex Particle code), using vortex particles. It combines a panel representation of the solid surfaces with a vortex parti-

cle approximation of the wake. Solid surfaces can take one of the following representations: non-lifting bodies represented by sources (the tower), open lifting surfaces carrying dipoles and shedding vorticity along their edges (blades), closed lifting surfaces carrying sources and dipoles (thick blades).

Specifically for yaw misalignment in BEM modelling modifications are introduced to the effective wind speed, described in detail in [11]. In the vortex model there is no special consideration regarding yaw since the evolution of the wake is included in the simulation and its effect on the blade inflow conditions is considered analytically.

For the vortex simulation a “hybrid wake” is used when the main interest is in the rotor region. The basic idea is to keep in fully active form only a limited part of the wake (“near part”) covering a downstream length of 1–2D. Because vorticity must be conserved, it is necessary to also include the effect of the rest of wake in some approximate way. In steady state conditions it can be verified [20], that the effect of the remaining of the wake on the “near” region can be approximated by an extra wake length of 2–3D provided that it contains the starting vortex or equivalently that vorticity is conserved. Clearly during the evolution of the wake, the starting vortex will be convected downstream rotor region and therefore its effect will decay. However as the staring vortex is convected additional vorticity will be added in the wake which will balance this decay and therefore on average the overall effect will remain constant and will correspond to the steady state to be attained. Details of the implementation are found in [11, 21, 22]

For stability calculations NTUA uses the in-house tool GAST (General Aerodynamic and Structural Tool). GAST is a servo-aero-elastic eigenvalue stability tool [23, 24] wherein the structural modelling of the complete wind turbine is based on a multi-body approach and a finite element discretisation of all flexible bodies [25]. Each component is introduced separately and specific kinematic and dynamic joint conditions are implemented to account for the connections of the body with the remaining structure. For the case of a wind turbine, such joint conditions are applied at the rotor hub and at the tower top. The kinematic degrees of freedom at the joints as well as the d.o.f. related to the controls of the wind turbine (pitch angle, generator speed, yaw angle of the nacelle) appear separately in the final system of the dynamic equations and appropriate equations are formulated for these additional d.o.f. For each body, dynamic equations of motion are expressed with respect to a body fixed coordinate system, which means that in the case of a rotating blade, analysis is performed in the rotating coordinate system. In the stability version of GAST the concept of the “aeroelastic element” is introduced. The dynamic equations of motion of the beam element are supplemented by the equations of ONERA model for the aerodynamic d.o.f (lift, drag and moment), linearised about a reference state. This way the equations of every beam element, apart from the elastic d.o.f. (elastic deflections and rotations), also include the aerodynamic d.o.f. [26]. The input then required for the purpose of the stability analysis is the inflow parameters, including the induction effects, at the reference state, which can be selected to be either the deformed or the undeformed state.

3.3 GE aeroelastic simulations

An in-house BEM-type model is used by GE for aeroelastic simulations. For the aerodynamics the implementation of the BEM equations follows AeroDyn [27], where the aggregate of all blade element within the annulus are balanced with a full annular streamtube. A Beddoes-Leishman

dynamic stall implementation [27] is used. Engineering models are employed for

- Wake modelling (Hansen-type)
- Tip loss (Prandtl)
- Skewed inflow model (Hansen-type)
- Dynamic wake (Øye [28])
- High induction correction (Glauert [10])

The structural model uses Euler-Bernoulli beams without torsional deformation. A constant term for the overall rotational inertia along pitch axis, independent of deformation, is used. The solution is marched in time using “loose” coupling between the structural and aerodynamic parts (no aero sub-cycling, so that the aerodynamic states are concealed from the system solver)

4 Results

The evaluation of the effect of higher and lower rotational speeds on the performance and loads was done through a series of tests, that included

- Changes in eigenfrequencies and stability results
- Changes in the power and thrust
- Changes in the dynamic behaviour

We summarize the findings from these tests in the following, trying to identify the changes from the reference wind turbine. A full description of the test cases is given in [29]. A description of the sensors recorded is given in `AVATAR_WP4_T4.3 List of Sensors.xls`. In the AVATAR team site all the results are available in the form of time series for the complete list of sensors.

4.1 Power Curve Verification

The first test was intended to verify that the power curves of the three wind turbines (reference, high-speed and low-speed) is similar. This is necessary for the following comparisons to be meaningful, as they need to refer to similar levels of power production.

The main parameter that we need to verify is the correct setting of the controller, ensuring that we get comparable power outputs for all three configurations. The results for the low-speed rotor and the high-speed rotor are given in figs. 6 to 7 and figs. 8 to 9 respectively. The design requirement is labeled as ”Design”, RES1 and RES2 correspond to two different BEM based simulations out of which the latter was run in stiff and flexible mode. There are some small deviations from the design requirement, especially near the rated wind speed, where the controller switches from the partial to the full power mode. The results are nevertheless sufficiently close to the design requirements for the purpose of the current study.

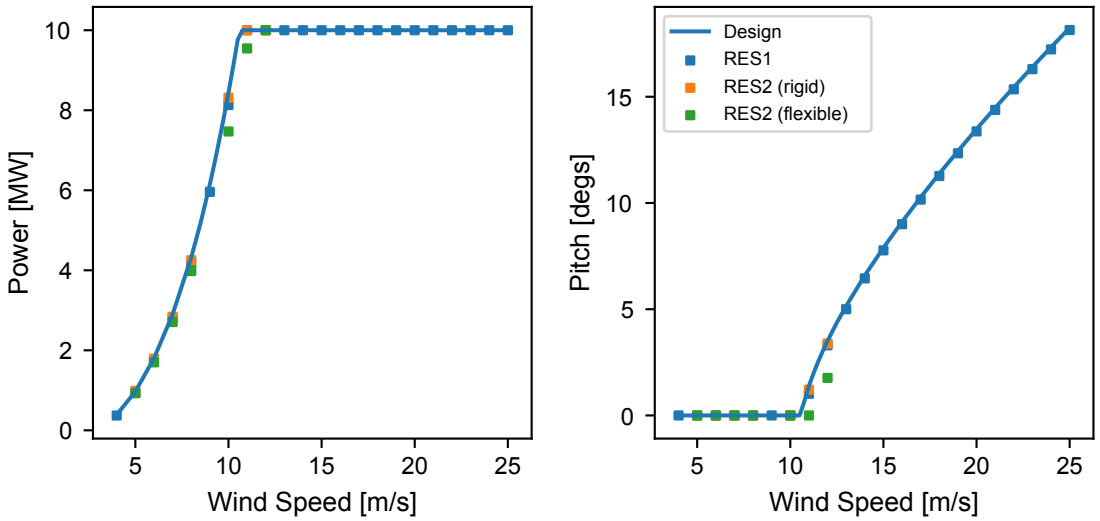

Figure 6: Power and pitch variation for the low-speed rotor, compared to the design requirement

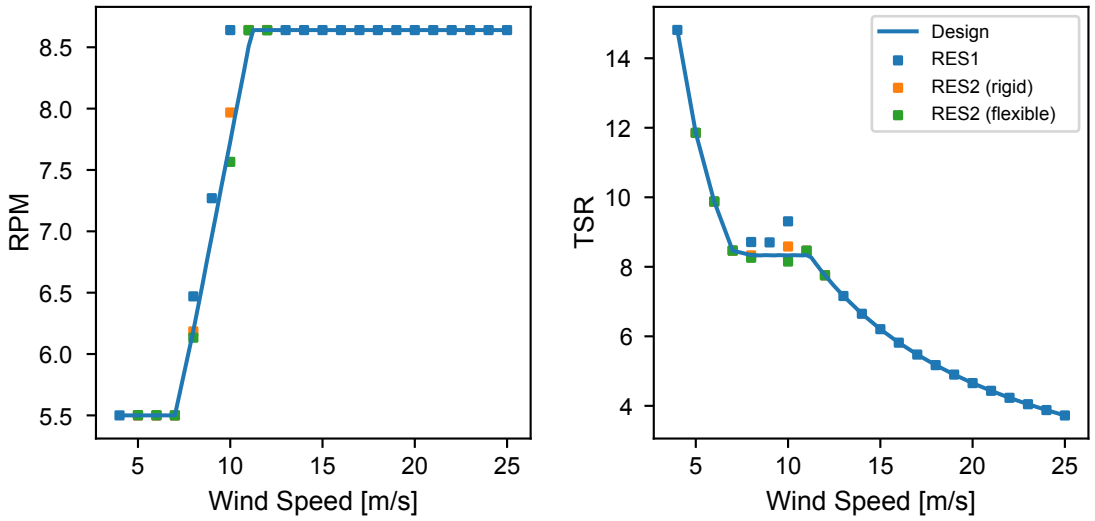

Figure 7: RPM and TSR variation for the low-speed rotor, compared to the design requirement

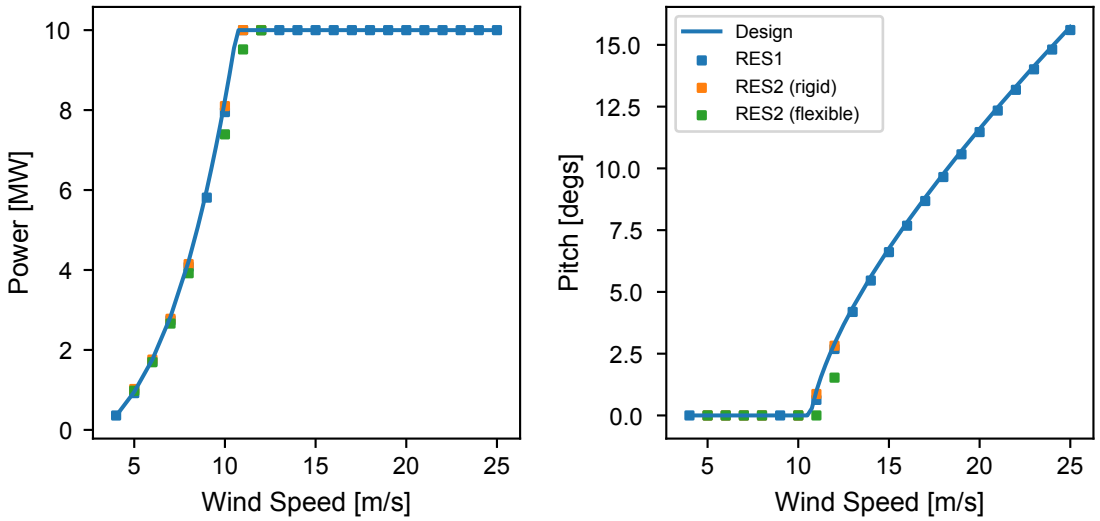

Figure 8: Power and pitch variation for the high-speed rotor, compared to the design requirement.

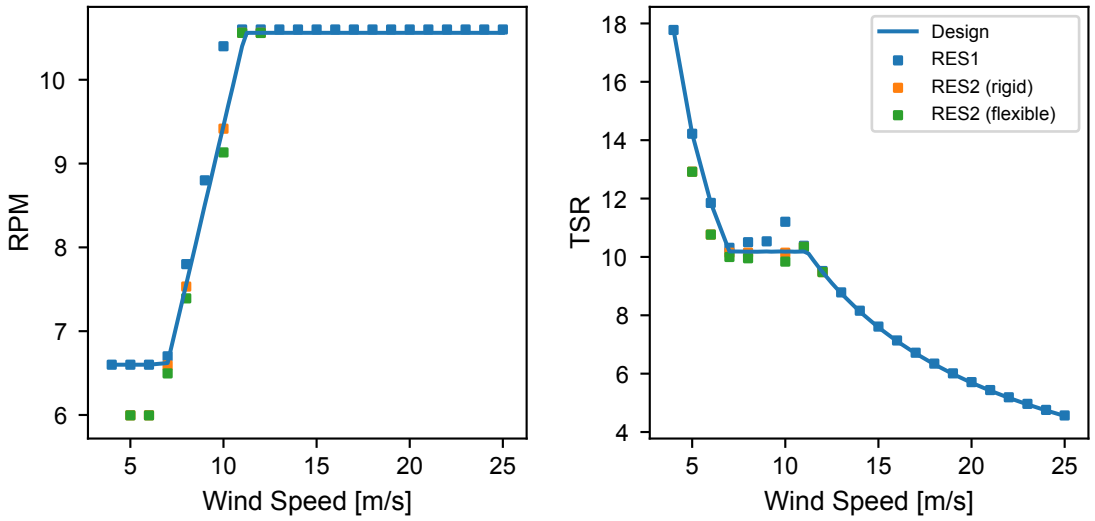

Figure 9: RPM and TSR variation for the high-speed rotor, compared to the design requirement

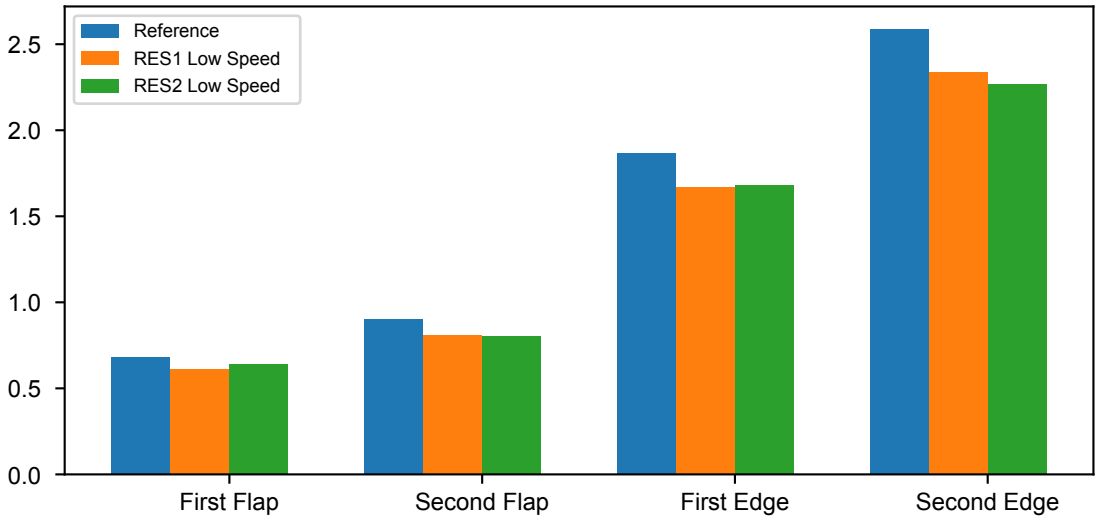

Figure 10: Eigenfrequencies of the blades for the low-speed rotor, compared to the reference design

4.2 Stability Results

A simplified stability analysis was performed for the two different rotors, operating at high and low speeds. It was not the intention of this study to investigate the details of the dynamic behaviour of the two systems, or focus on the discrepancies between the different calculation methods, as these issues have been covered in detail in e.g. [30].

In this case we simply verified that the placement of the eigenfrequencies was properly performed, so that there will not be an instability influencing the results in real turbulent wind operation and obscuring the changes that are actually due to the rotating speed difference. As seen in figs. 10 to 11, the target of shifting the eigenfrequencies by approximately the change in rotating speed is met.

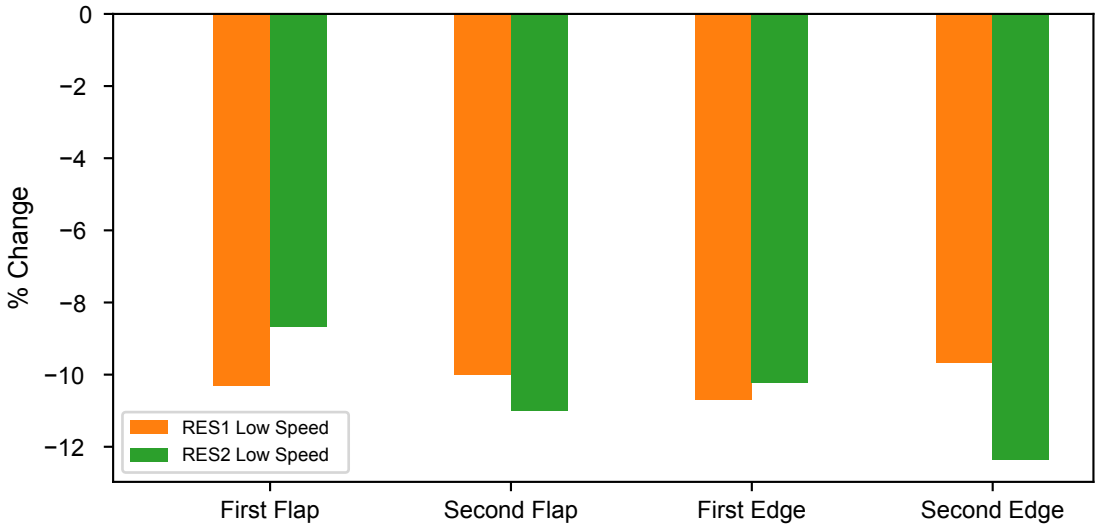

Figure 11: Eigenfrequencies of the blades for the low-speed rotor, compared to the reference design

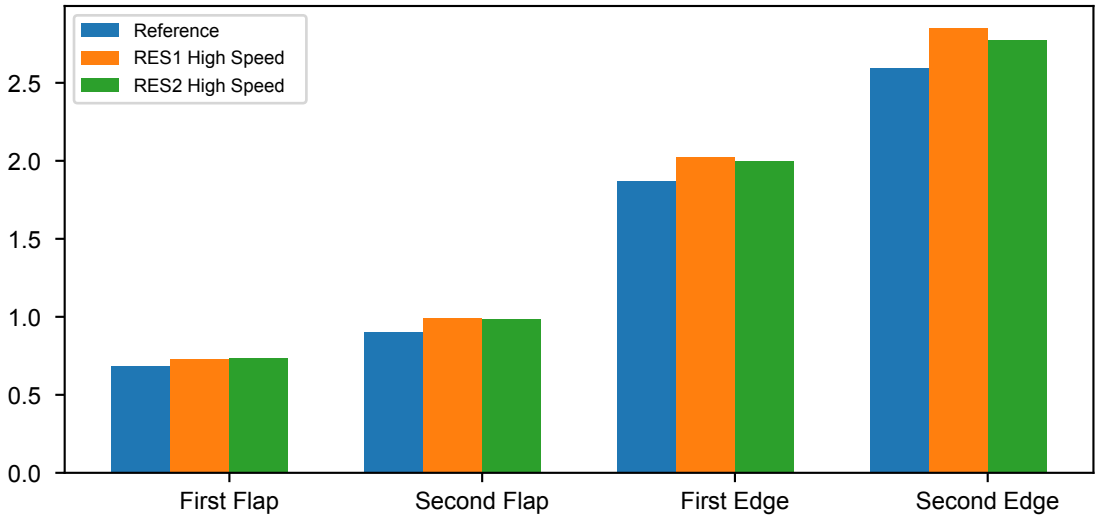

Figure 12: Eigenfrequencies of the blades for the high-speed rotor, compared to the reference design

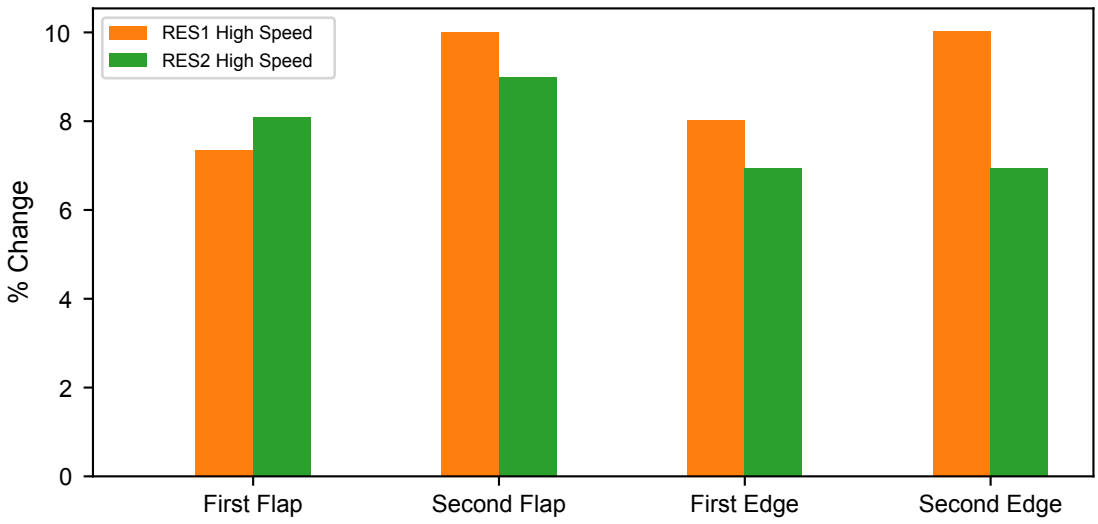

Figure 13: Eigenfrequencies of the blades for the high-speed rotor, compared to the reference design

4.3 Unsteady Runs

For the evaluation of the unsteady behaviour of the high and low speed versions of the AVATAR rotor, two design load cases were evaluated.

- Case DLC1.2, corresponding to normal operation with the NTM (Normal Turbulence Model). This was used to assess the effect of rotational speed on normal operating loads and fatigue.
- Case DLC1.3, corresponding to operation using the ETM (Extreme Turbulence Model). This was used to assess the effect of rotational speed on maximum loads due to turbulence.

In both cases we have not used the full IEC procedure but a “simplified” variation, where

- A single seed is used, common for all the partners, for each wind speed
- A limited set of wind speeds is examined, at 6.0 m/s, 9.0 m/s, 10.75 m/s, 18.0 m/s and 20.0 m/s

The purpose of the evaluation is to quantify the effect of the rotational speed on the various loads. To this end we utilize the maximum values from DLC1.3 and the standard deviation from DLC1.2 (indicative of the fatigue loads). In all cases the mean values are also given. Differences between the different sets are not specifically discussed. Such a code-to-code comparison was done in previous tasks within WP4.

4.3.1 Overall Performance

The overall performance is evaluated through the predictions of aerodynamic thrust torque and power for the two rotors, compared to the reference AVATAR rotor. Looking at the mean torque values, (fig. 14) it is apparent that there is an increase of $\sim$10 % for the low-speed rotor and a similar decrease for the high-speed rotor. This is in-line with the design principle, as the power curve is supposed to be similar between the three designs. For normal operation there is also a decrease of the torque variation with the high-speed design (fig. 15). The same trends appear when the ETM simulation is performed, with the torque variation becoming more pronounced for the low-speed rotor (figs. 16 to 18)

For the thrust and power, the mean values are mostly the same in all three rotors, while the variations again seem to become larger for the low-speed rotor (figs. 19 to 28)

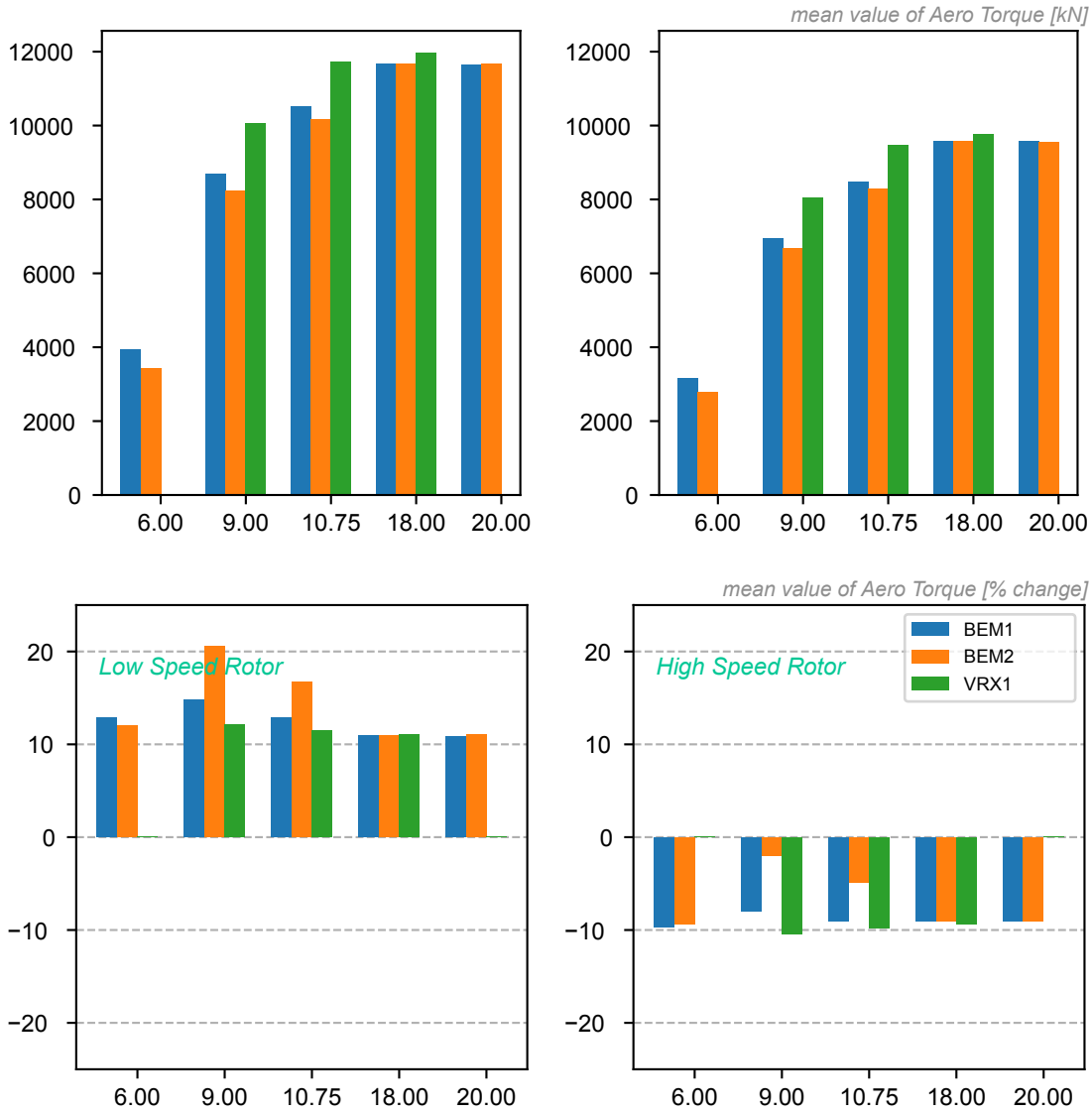

Figure 14: Absolute and Relative effect of rotational speed on the mean value of the Aero Torque for DLC1.2

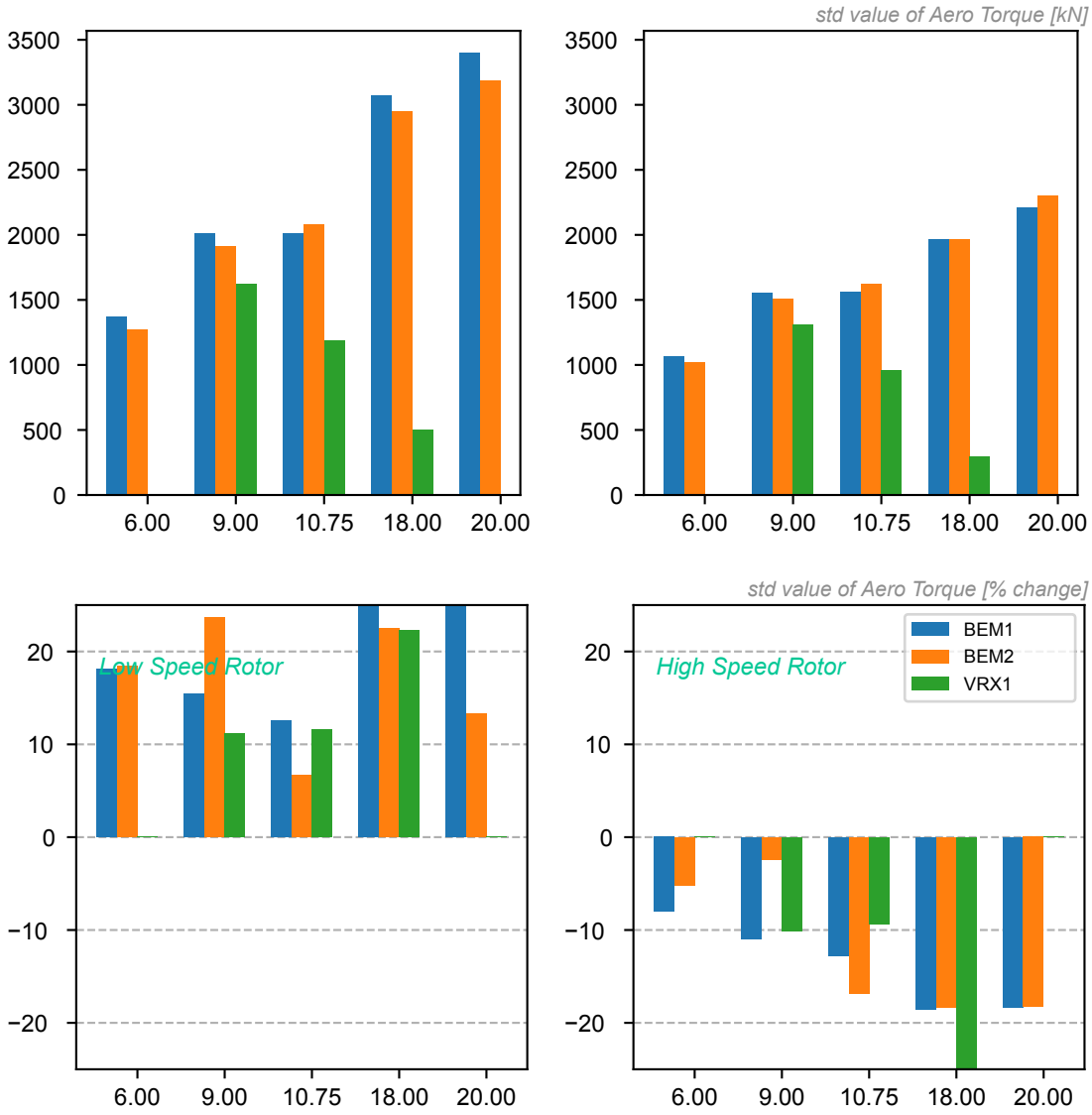

Figure 15: Absolute and Relative effect of rotational speed on the sdv value of the Aero Torque for DLC1.2

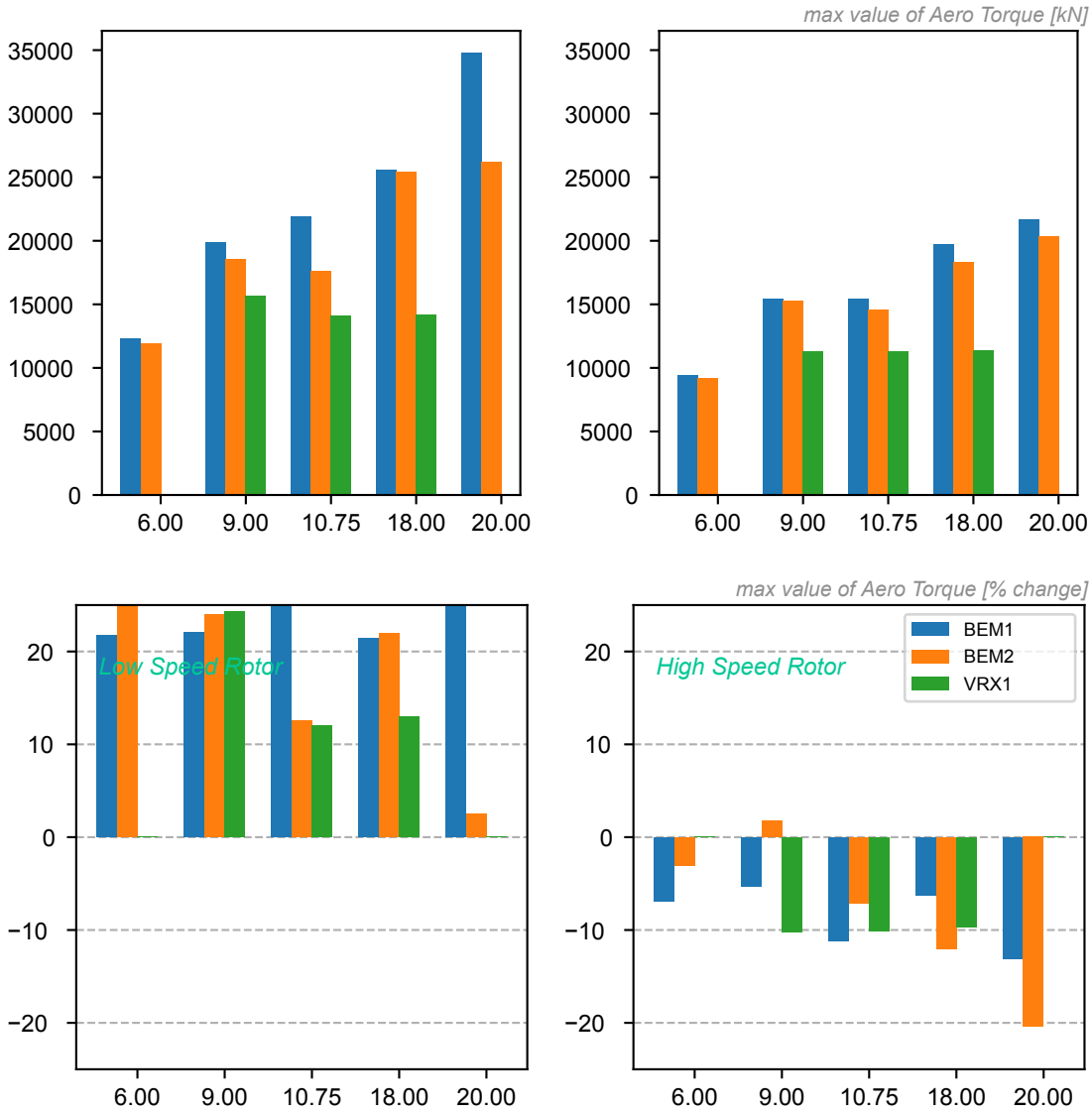

Figure 16: Absolute and Relative effect of rotational speed on the max value of the Aero Torque for DLC1.3

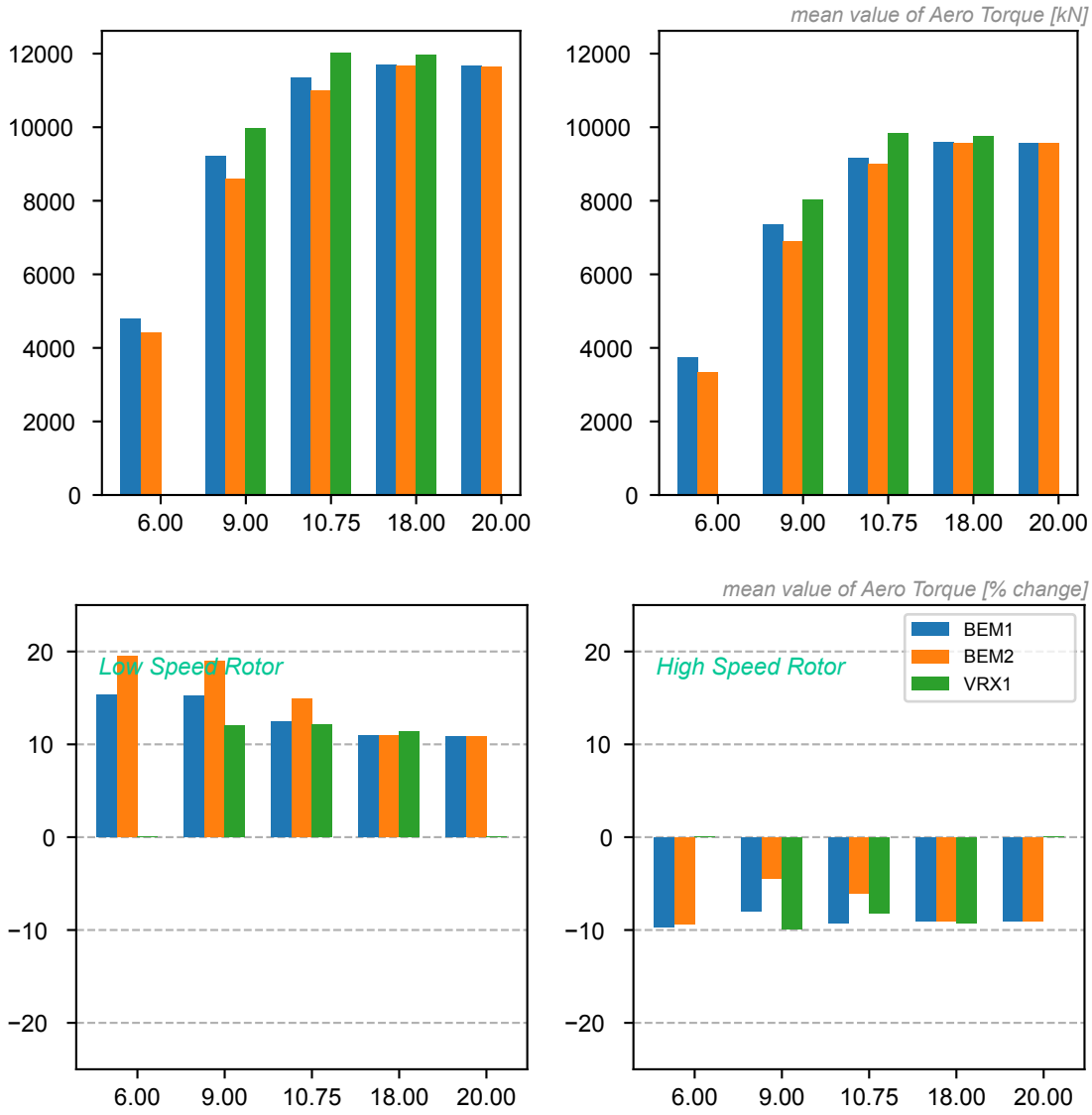

Figure 17: Absolute and Relative effect of rotational speed on the mean value of the Aero Torque for DLC1.3

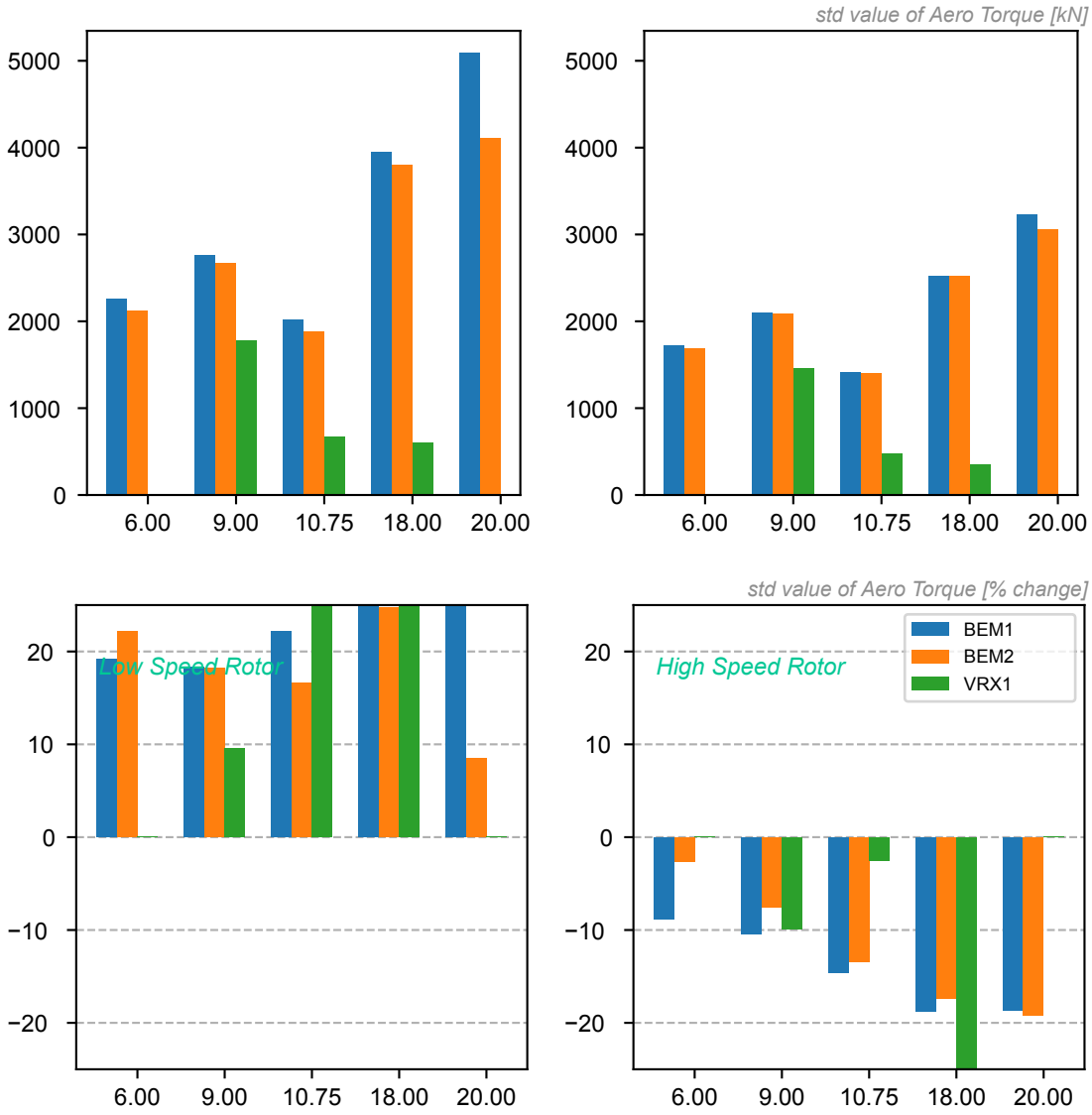

Figure 18: Absolute and Relative effect of rotational speed on the sdv value of the Aero Torque for DLC1.3

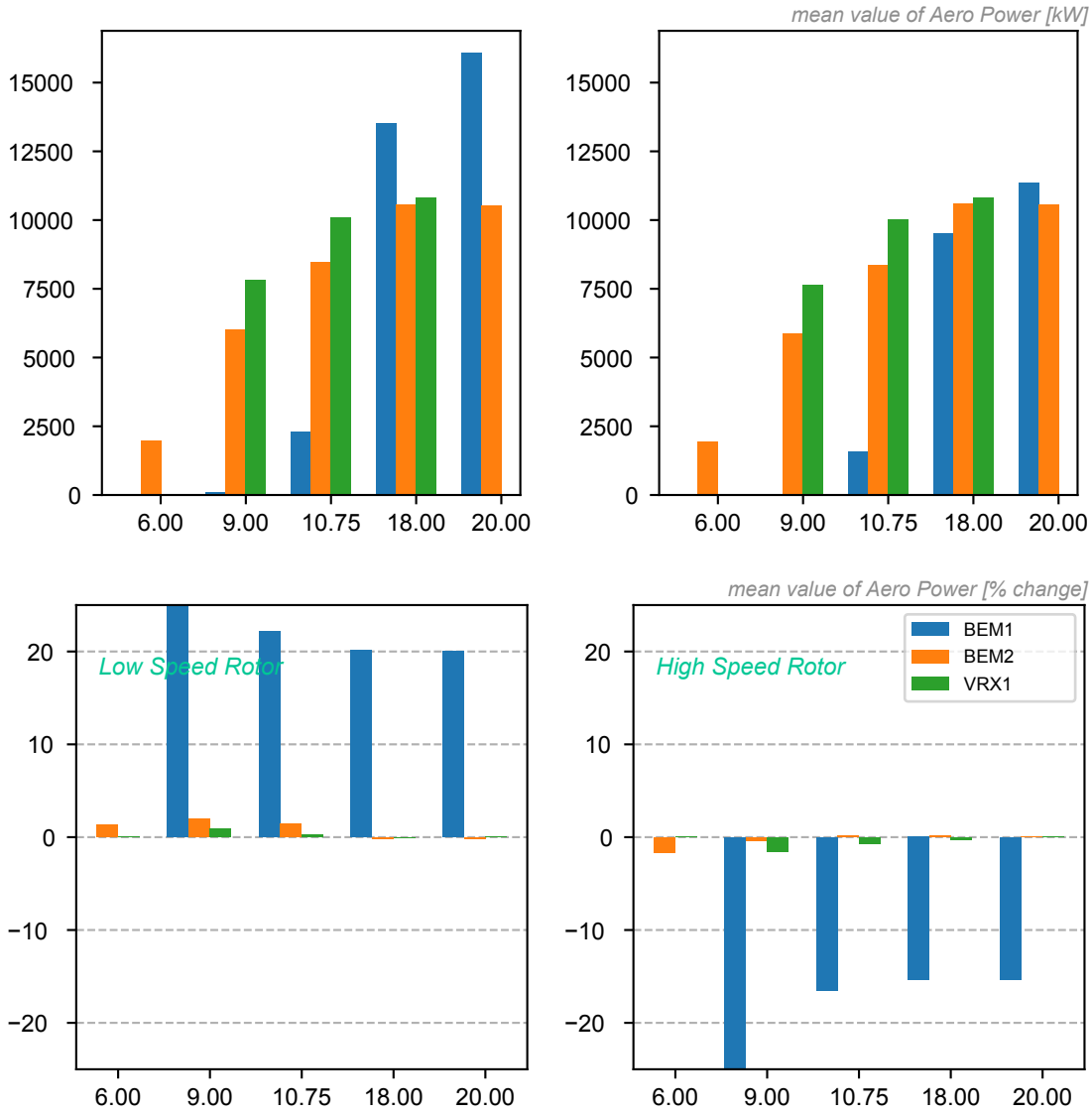

Figure 19: Absolute and Relative effect of rotational speed on the mean value of the Aero Power for DLC1.2

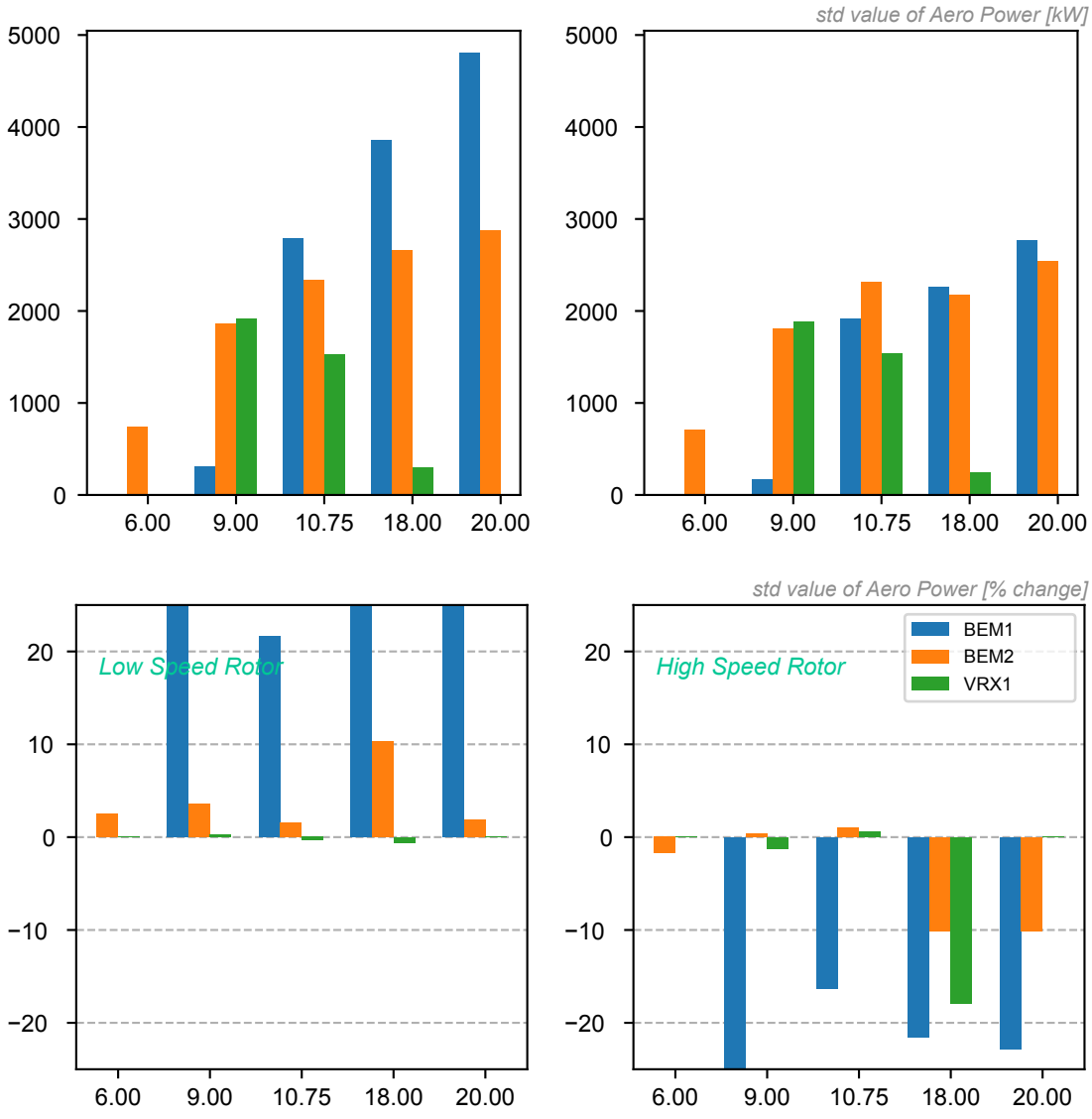

Figure 20: Absolute and Relative effect of rotational speed on Aero Power for DLC1.2

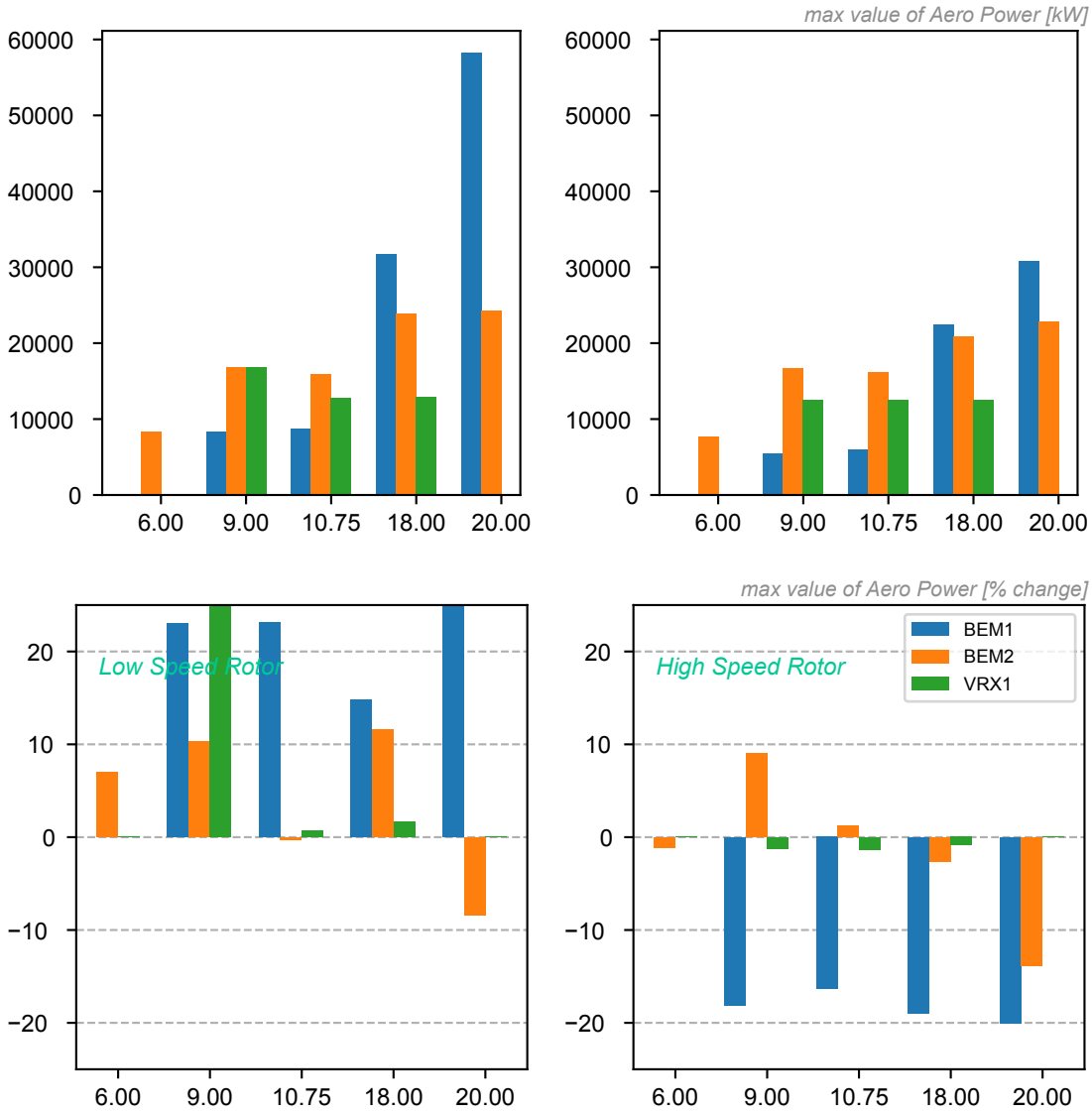

Figure 21: Absolute and Relative effect of rotational speed on the max value of the Aero Power for DLC1.3

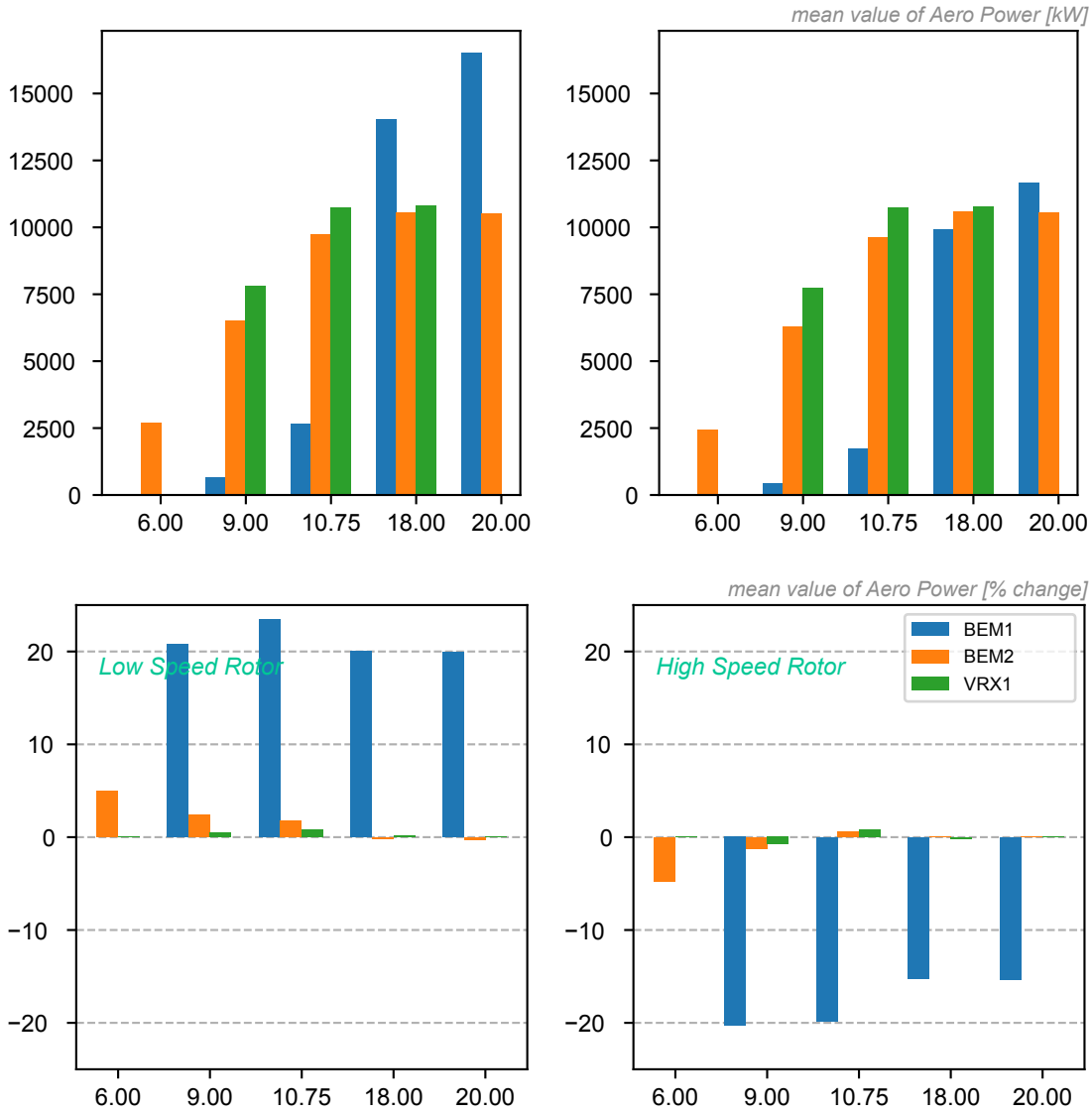

Figure 22: Absolute and Relative effect of rotational speed on the mean value of the Aero Power for DLC1.3

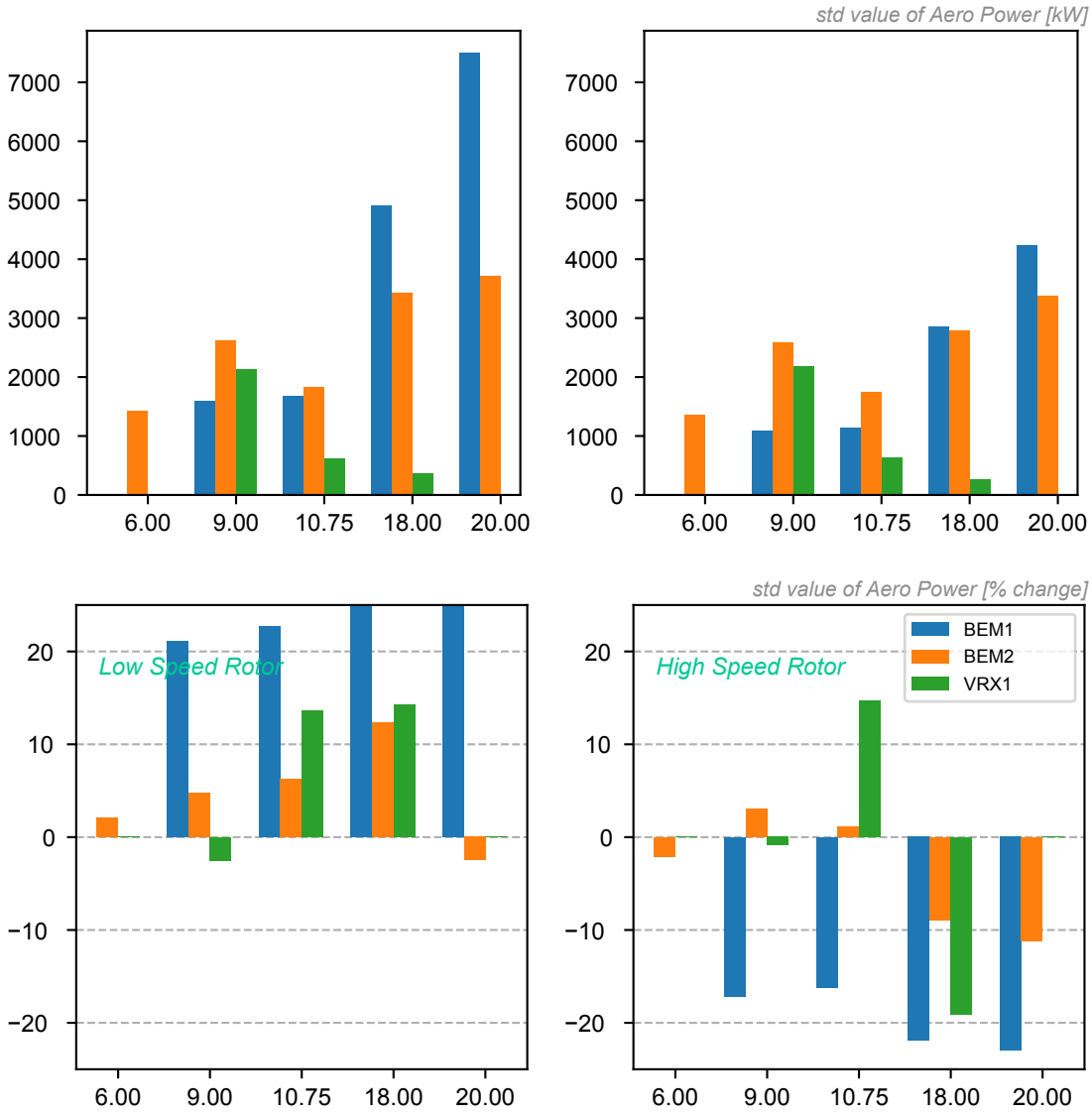

Figure 23: Absolute and Relative effect of rotational speed on Aero Power for DLC1.3

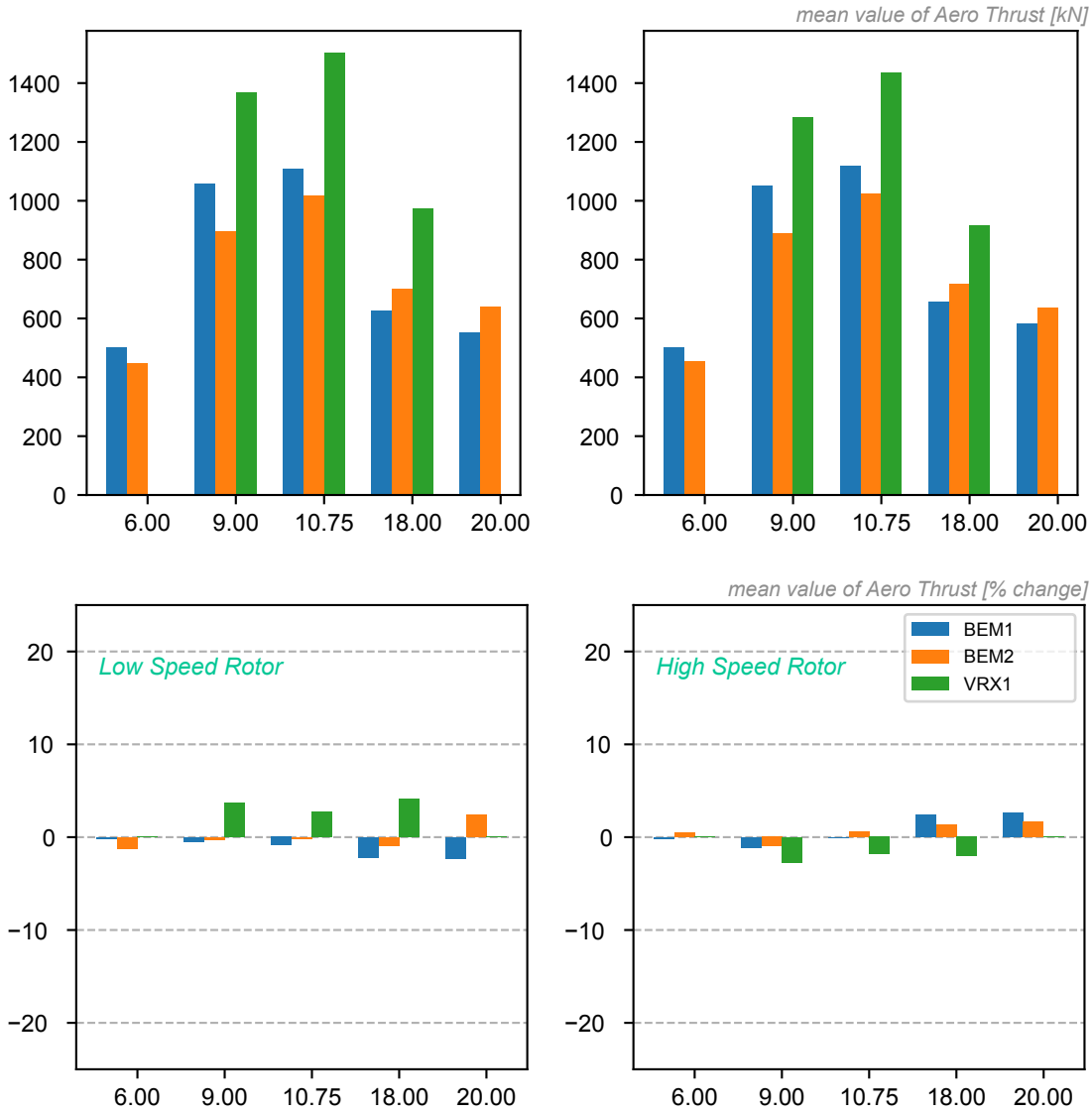

Figure 24: Absolute and Relative effect of rotational speed on the mean value of the Aero Thrust for DLC1.2

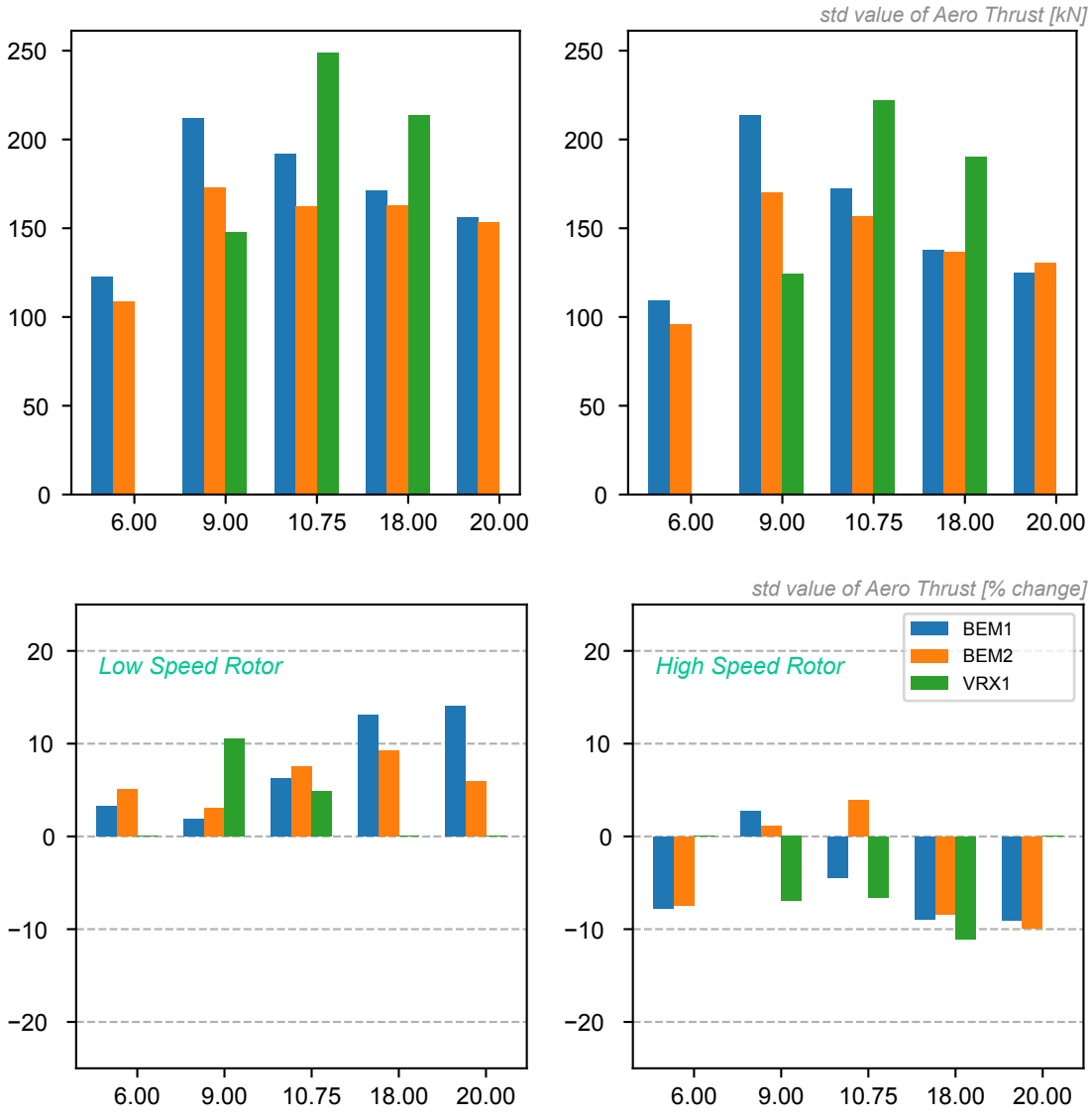

Figure 25: Absolute and Relative effect of rotational speed on Aero Thrust for DLC1.2

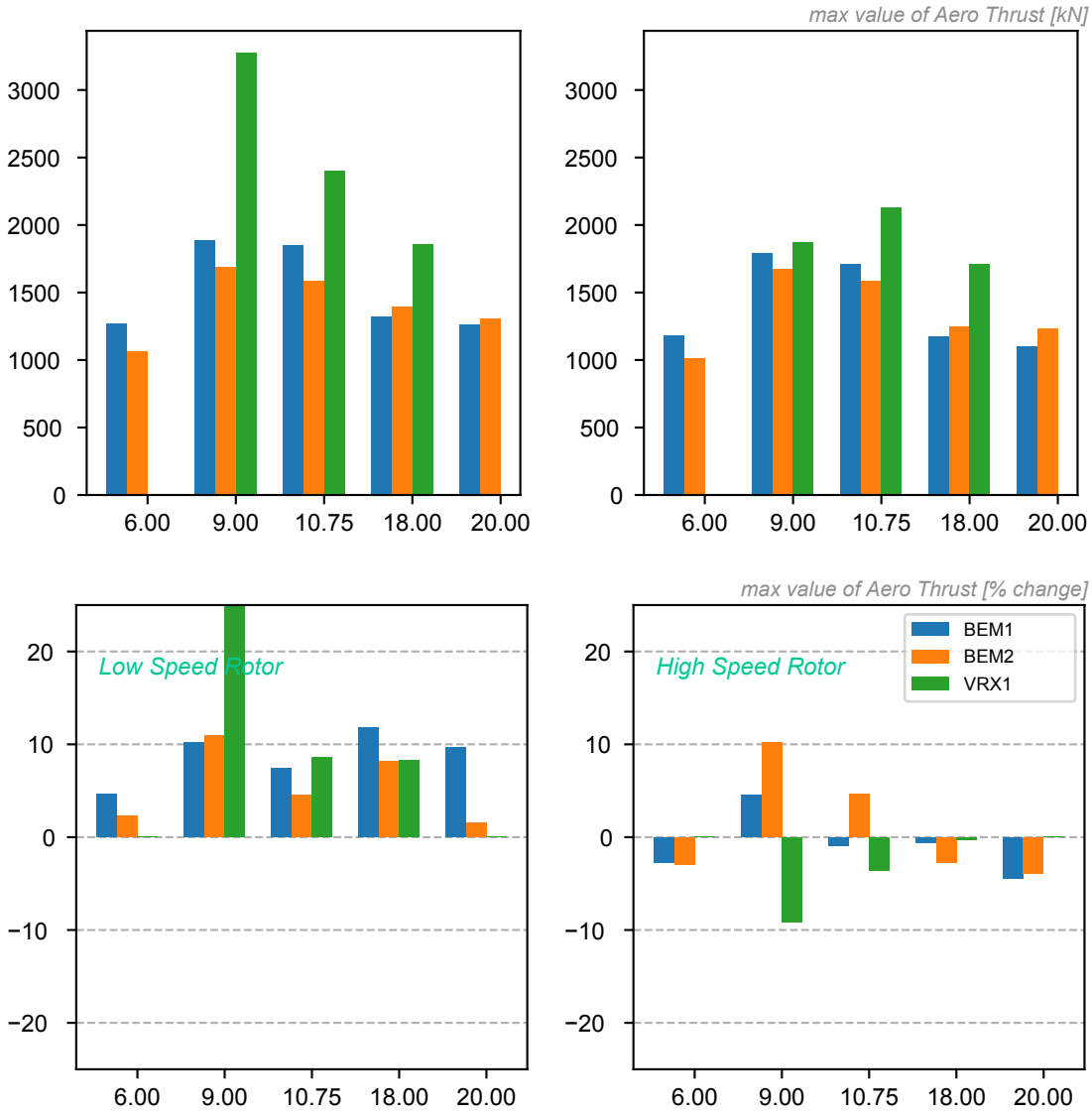

Figure 26: Absolute and Relative effect of rotational speed on the max value of the Aero Thrust for DLC1.3

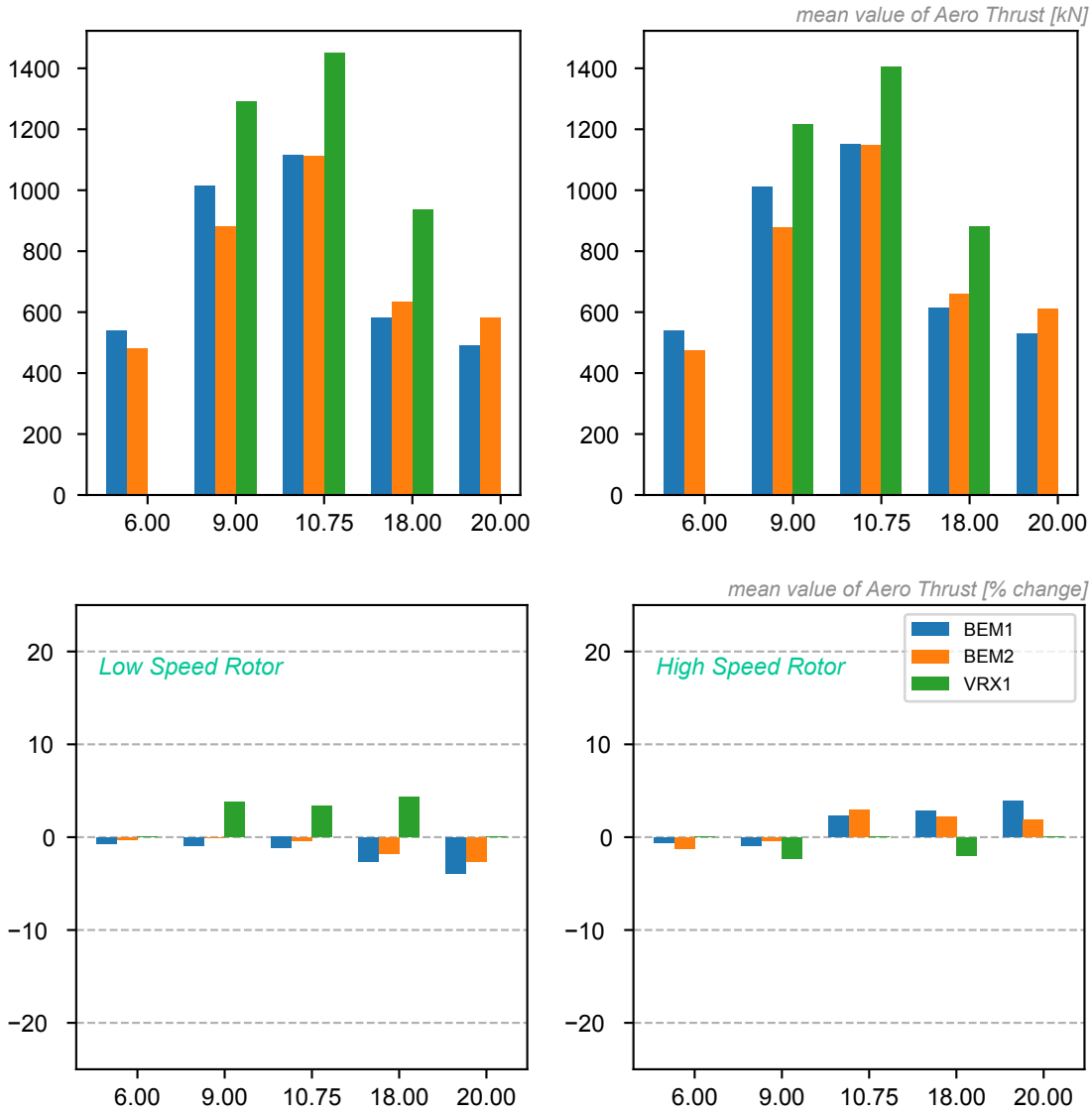

Figure 27: Absolute and Relative effect of rotational speed on the mean value of the Aero Thrust for DLC1.3

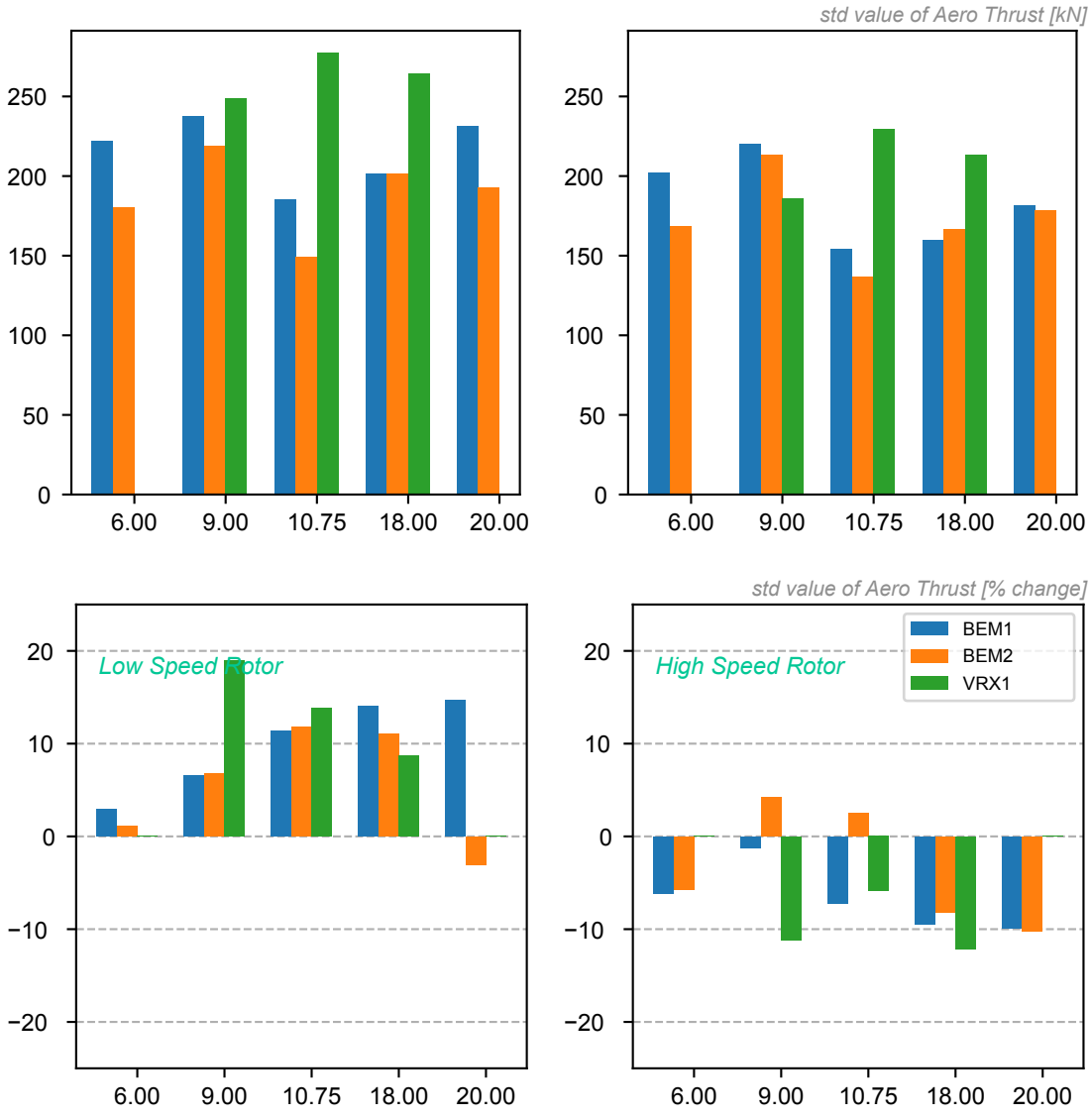

Figure 28: Absolute and Relative effect of rotational speed on Aero Thrust for DLC1.3

4.3.2 Tower Loads

The change in the loading of the tower was also examined in the context of this comparison. The fore-aft, side-to-side and yawing moments at the tower bottom are presented as representative of the overall effect. Deflections at the tower top are also given.

The change in mean value of the fore-aft and yawing moments does not show a clear trend, while the side-to-side bending moment decreases with rotating speed. The variations are generally smaller for the high-speed rotor.

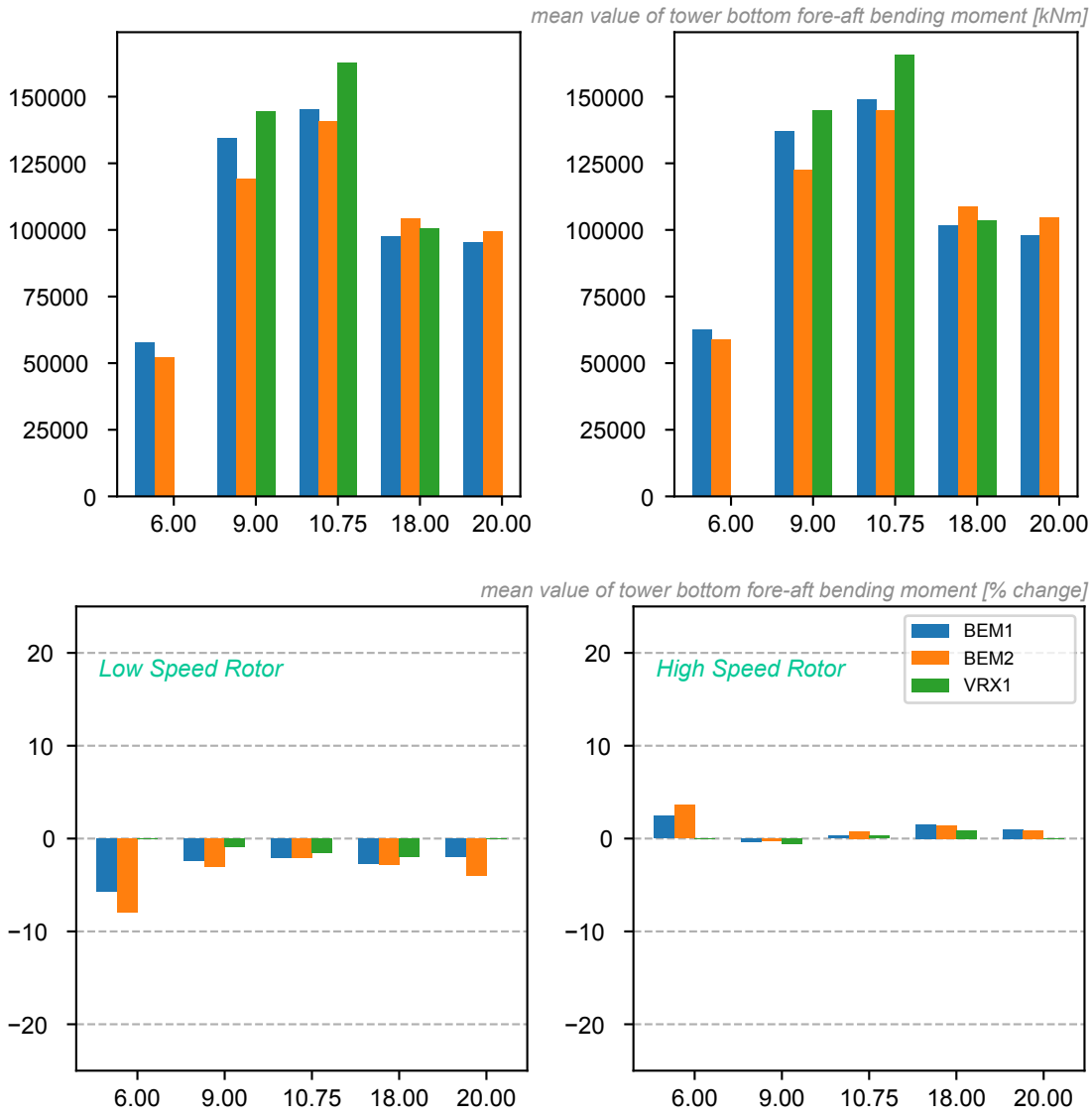

Figure 29: Absolute and Relative effect of rotational speed on the mean value of the tower bottom fore-aft bending moment for DLC1.2

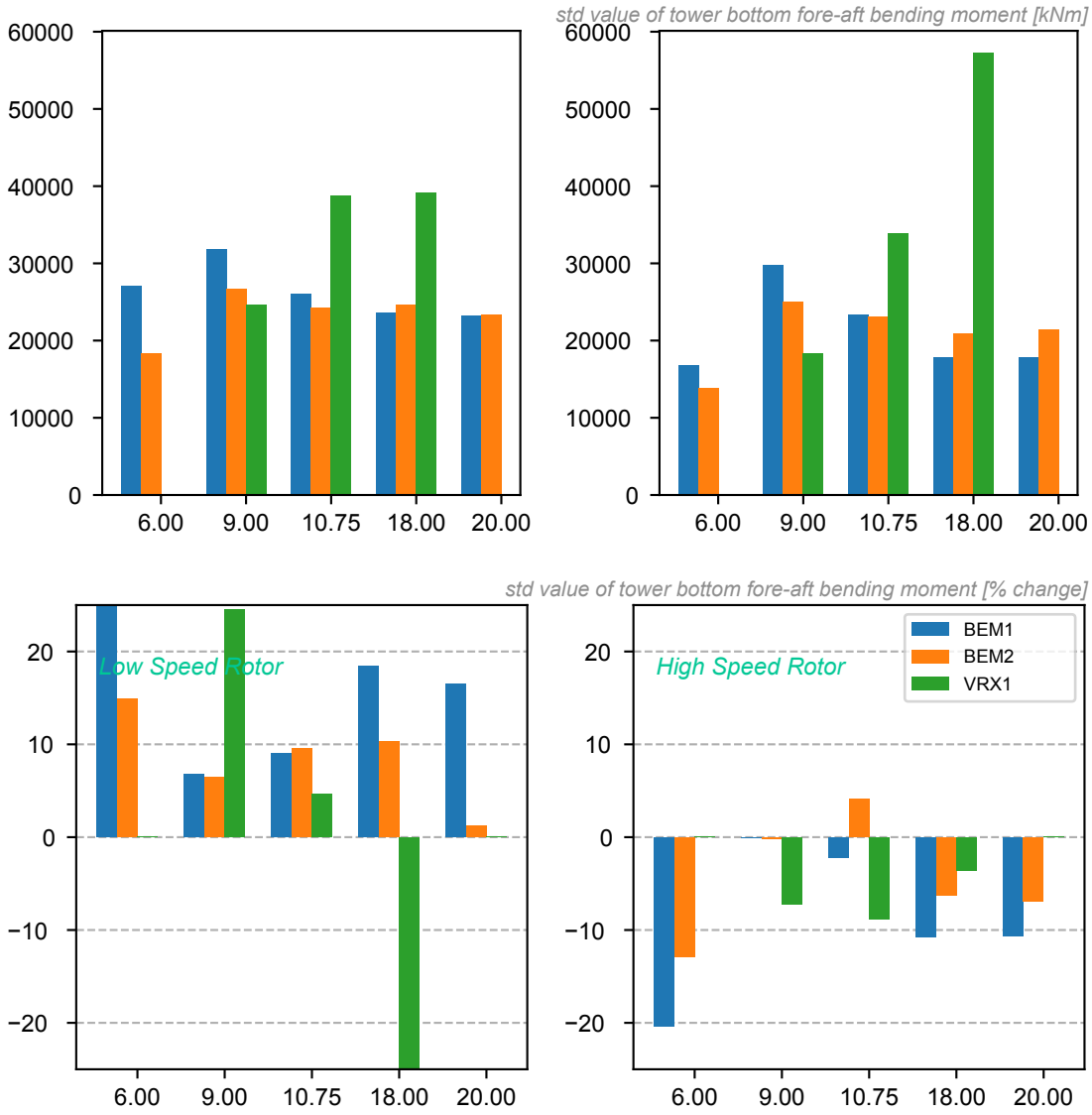

Figure 30: Absolute and Relative effect of rotational speed on tower bottom fore-aft bending moment for DLC1.2

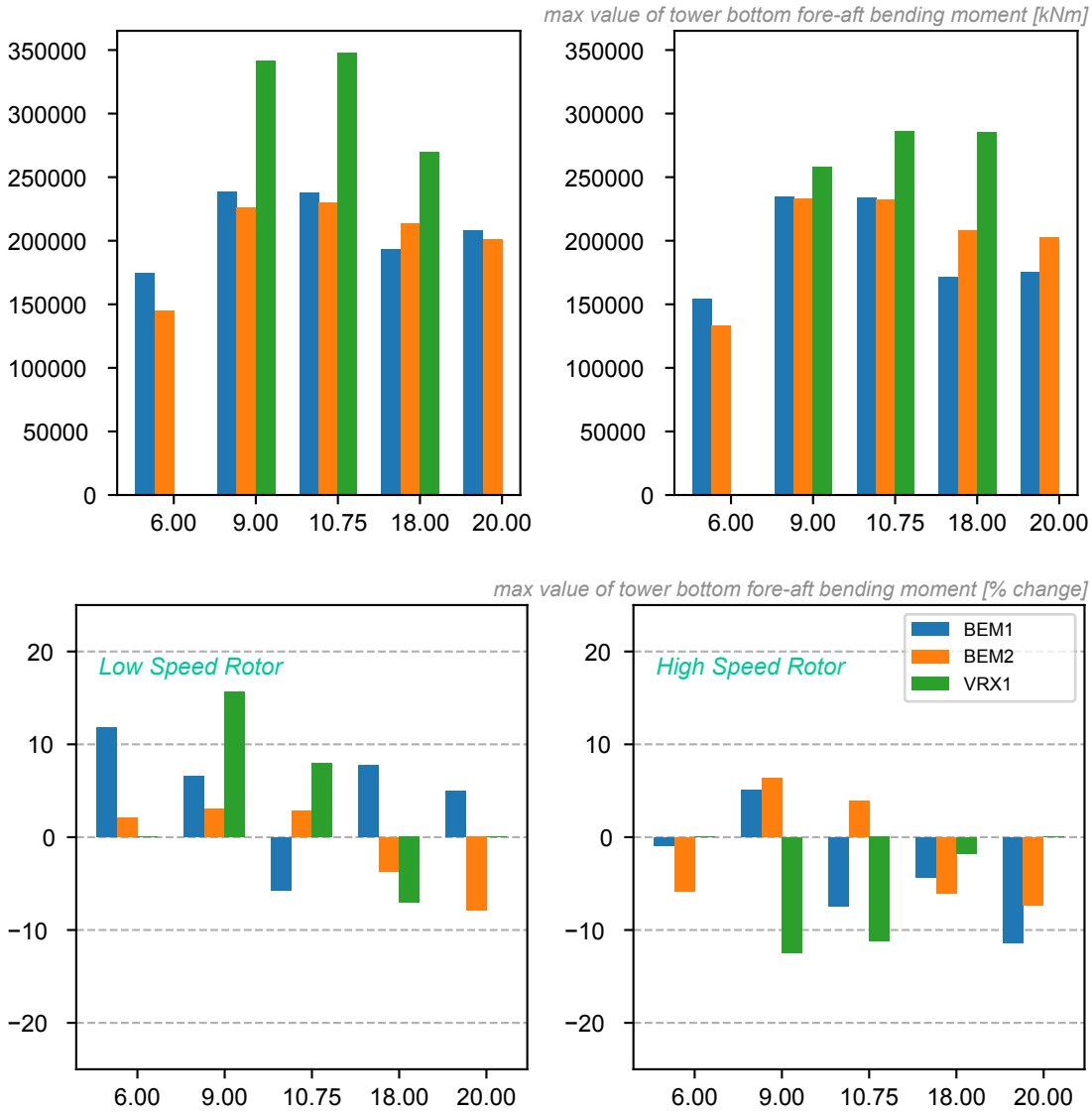

Figure 31: Absolute and Relative effect of rotational speed on the max value of the tower bottom fore-aft bending moment for DLC1.3

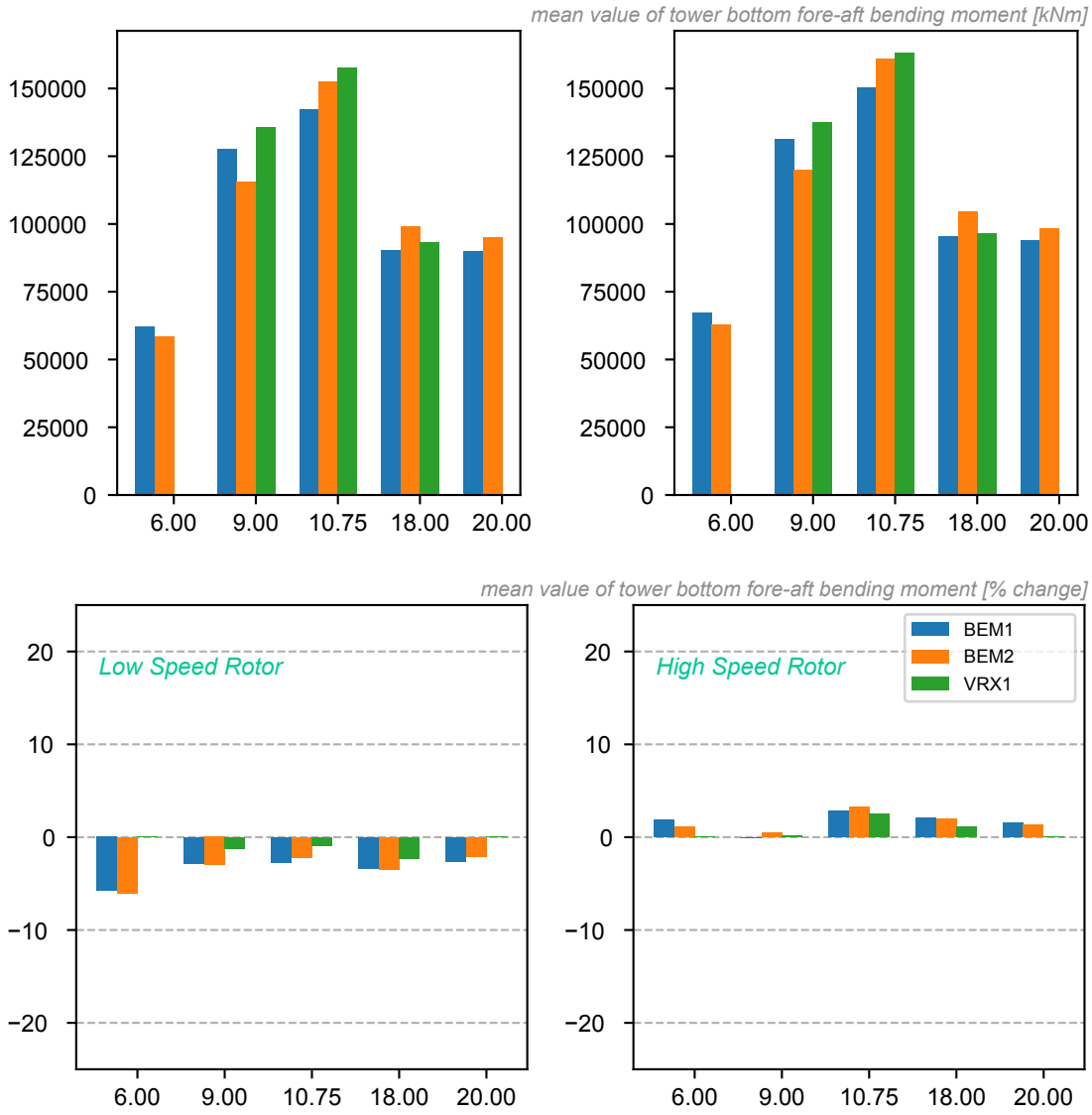

Figure 32: Absolute and Relative effect of rotational speed on the mean value of the tower bottom fore-aft bending moment for DLC1.3

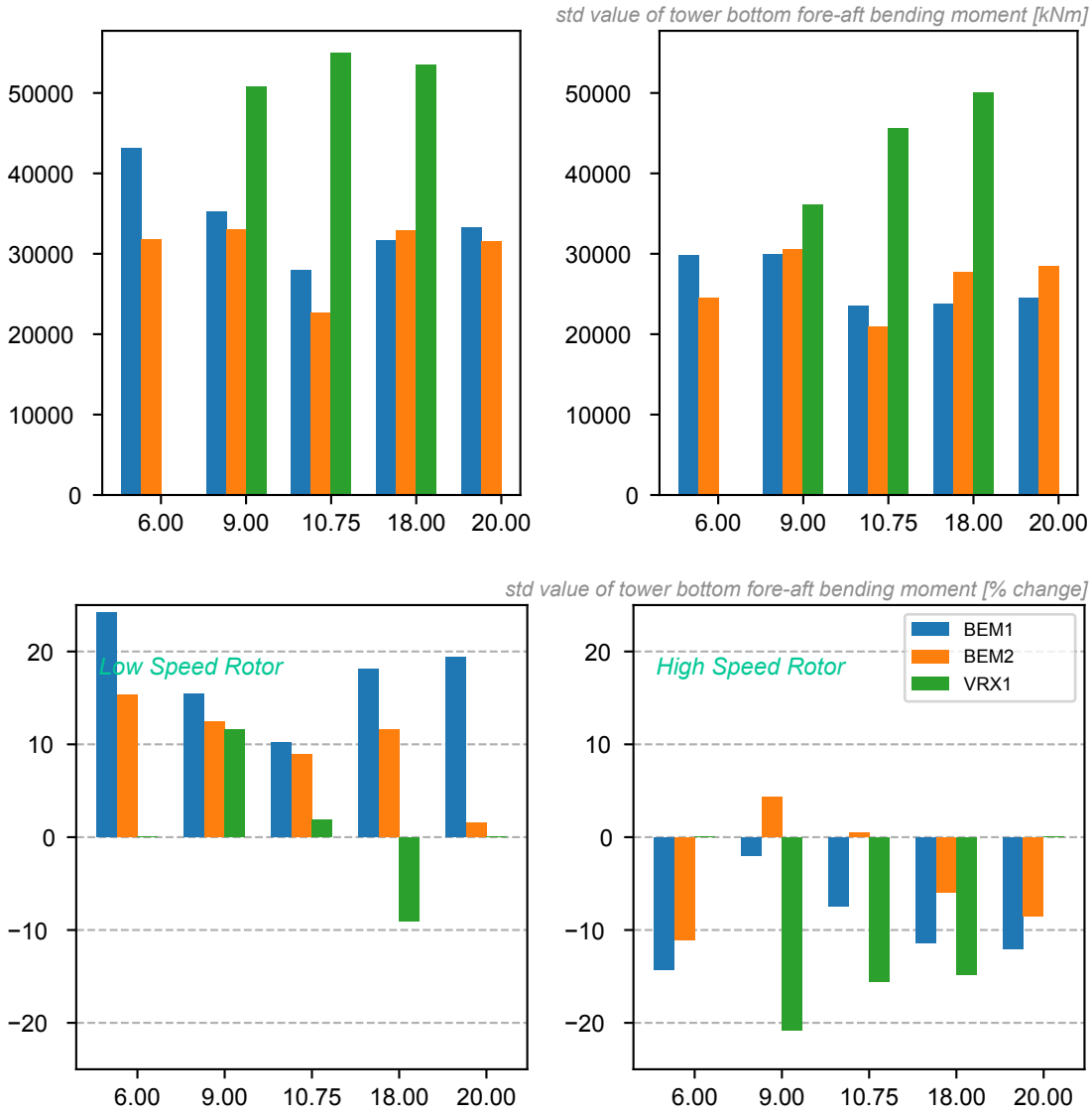

Figure 33: Absolute and Relative effect of rotational speed on tower bottom fore-aft bending moment for DLC1.3

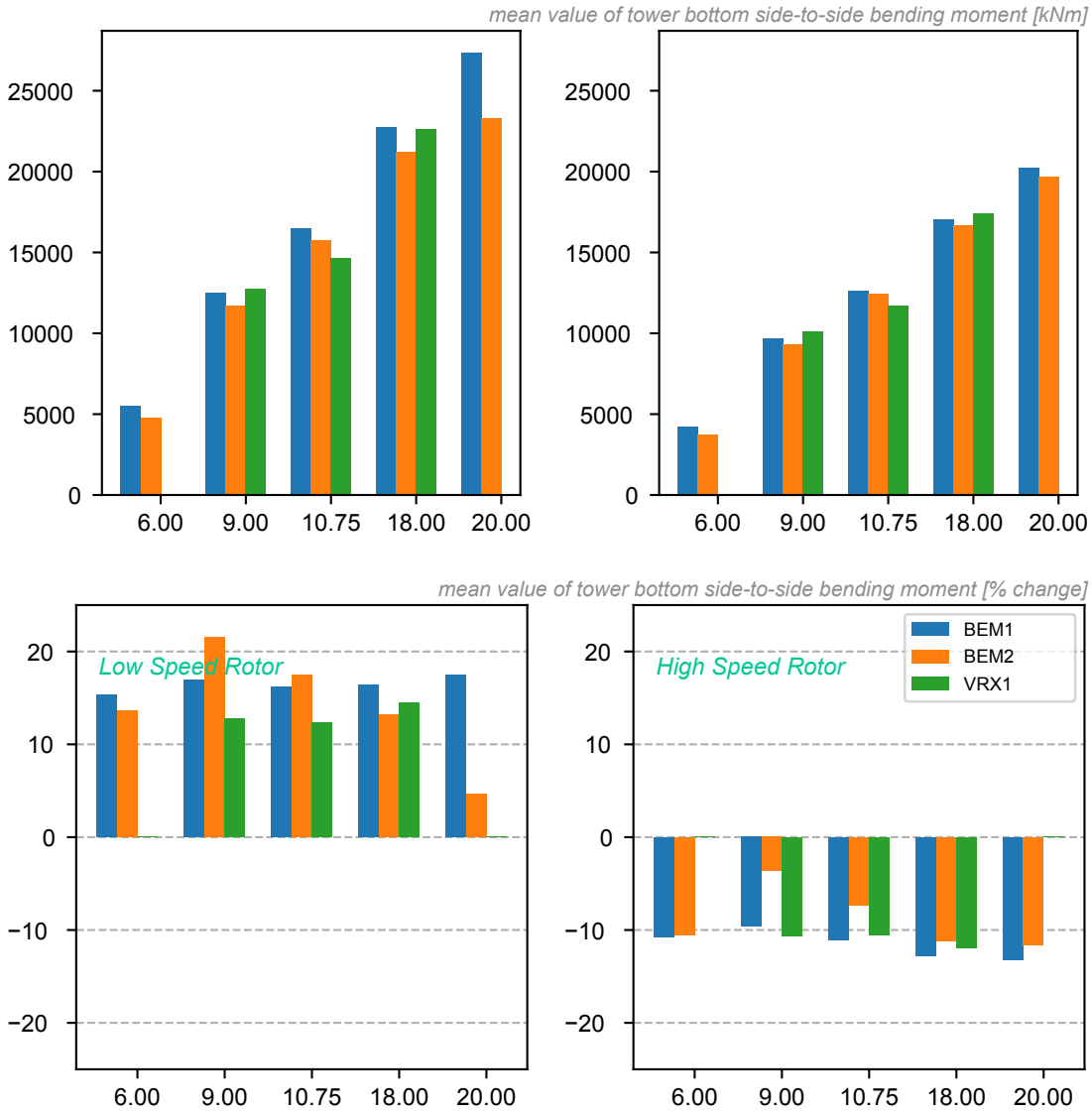

Figure 34: Absolute and Relative effect of rotational speed on the mean value of the tower bottom side-to-side bending moment for DLC1.2

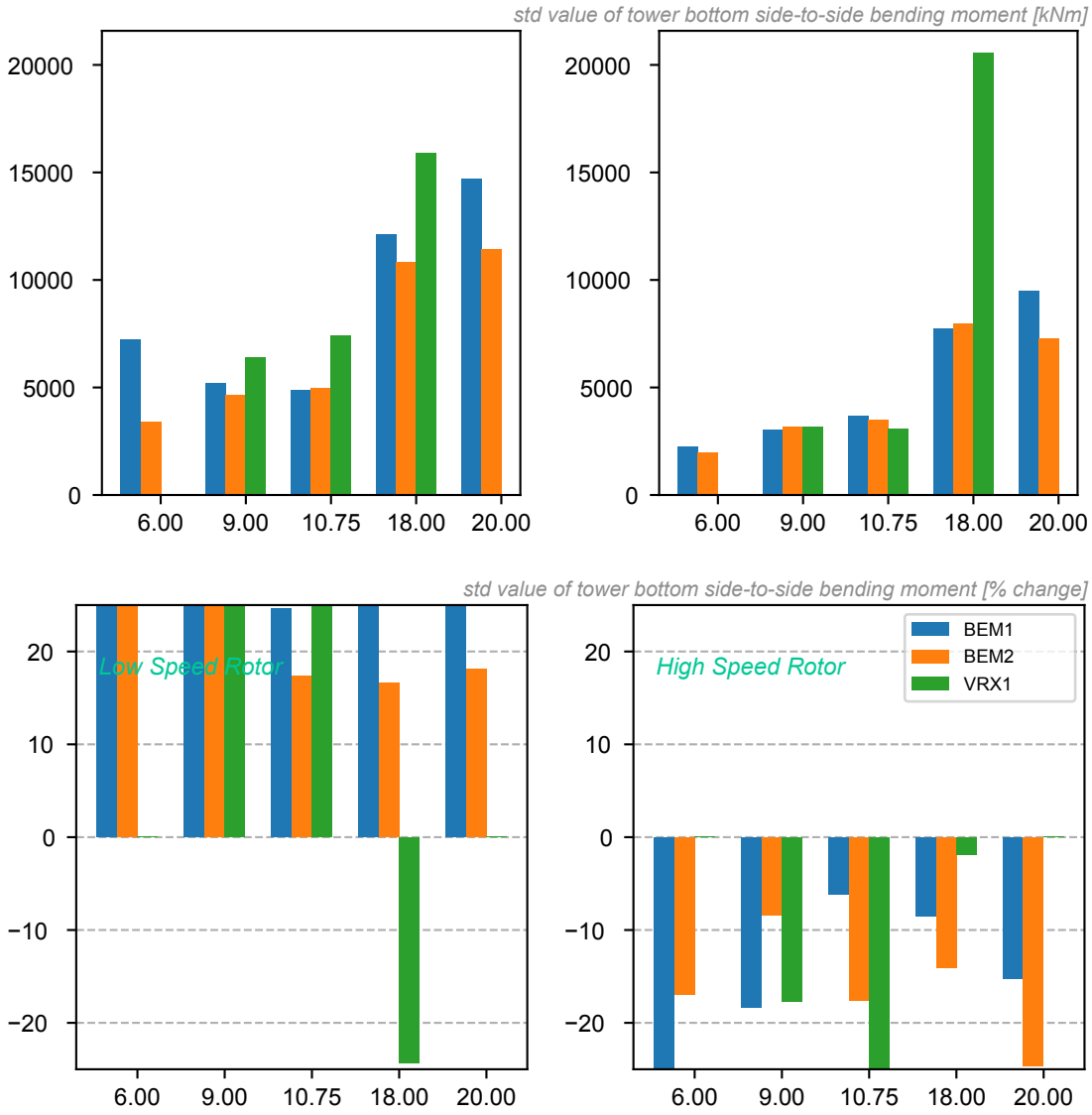

Figure 35: Absolute and Relative effect of rotational speed on tower bottom side-to-side bending moment for DLC1.2

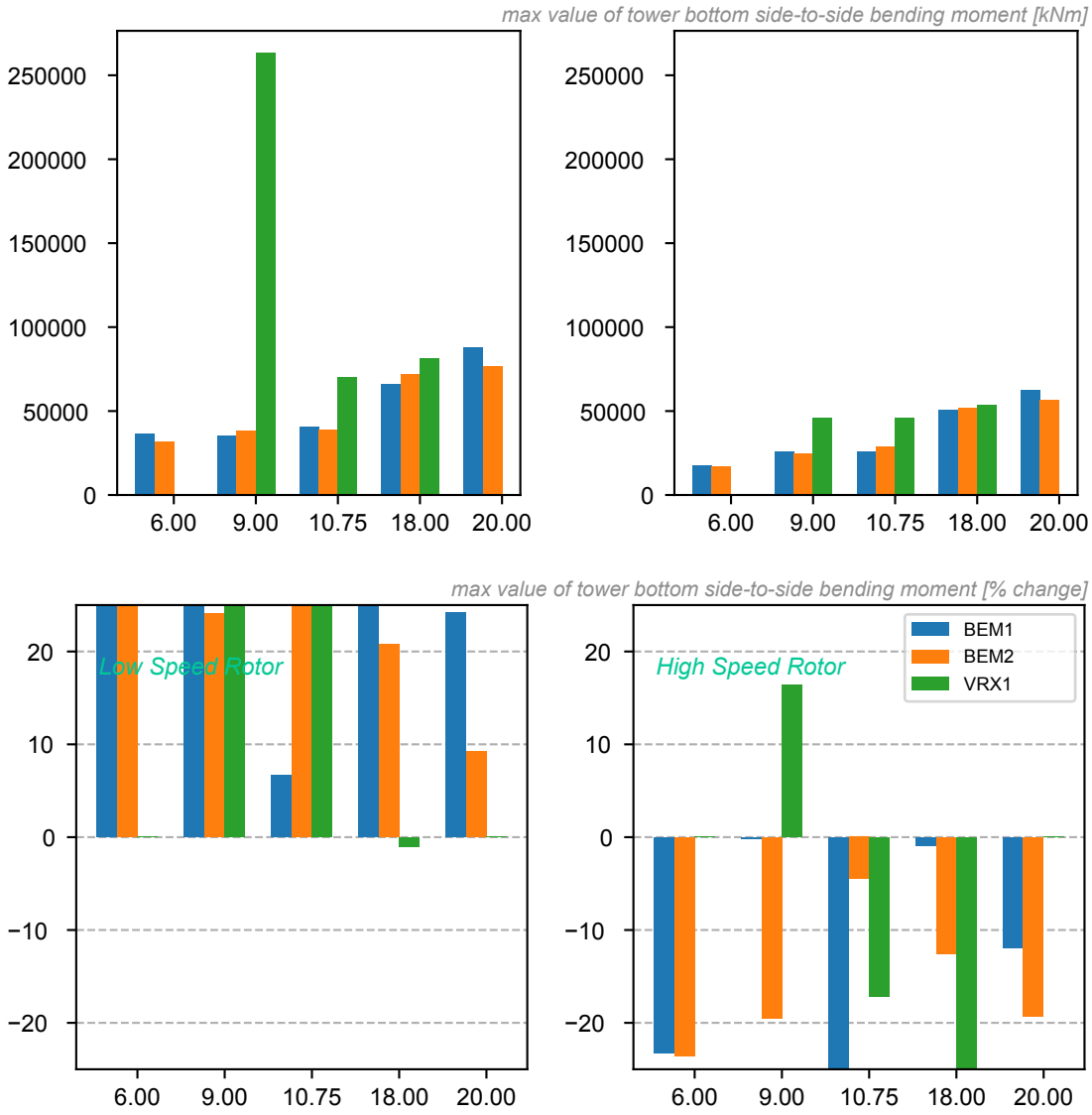

Figure 36: Absolute and Relative effect of rotational speed on the max value of the tower bottom side-to-side bending moment for DLC1.3

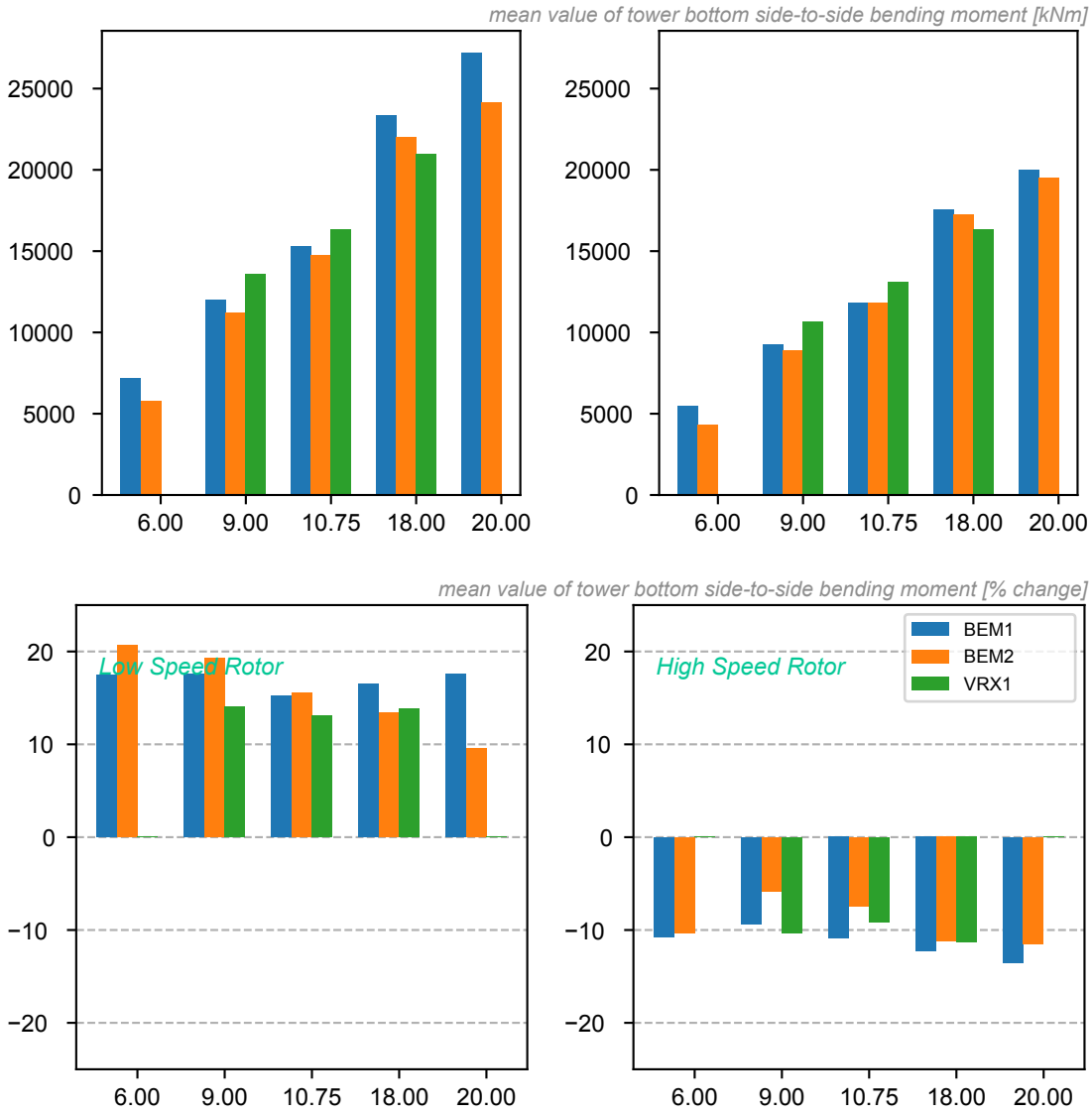

Figure 37: Absolute and Relative effect of rotational speed on the mean value of the tower bottom side-to-side bending moment for DLC1.3

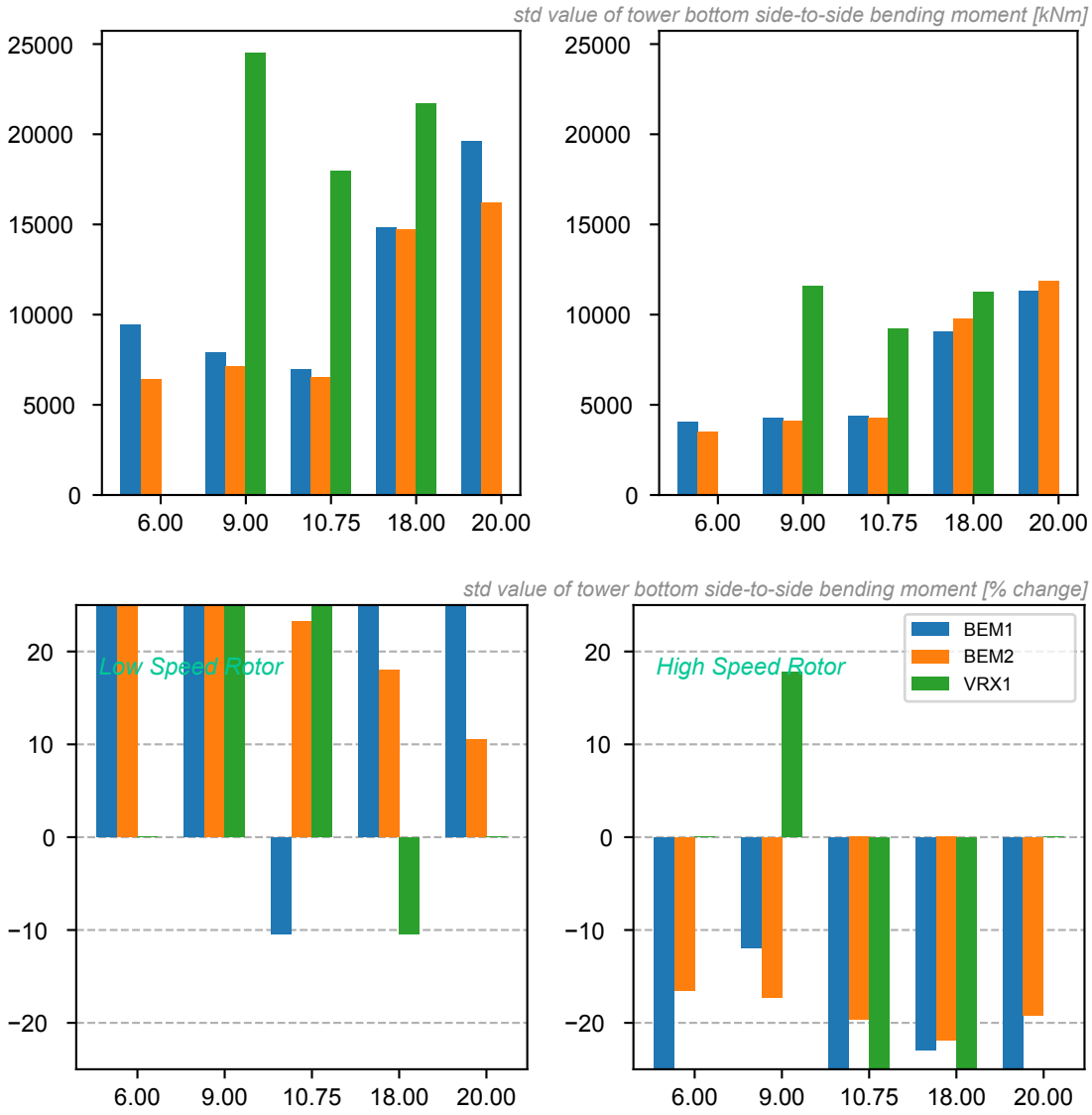

Figure 38: Absolute and Relative effect of rotational speed on tower bottom side-to-side bending moment for DLC1.3

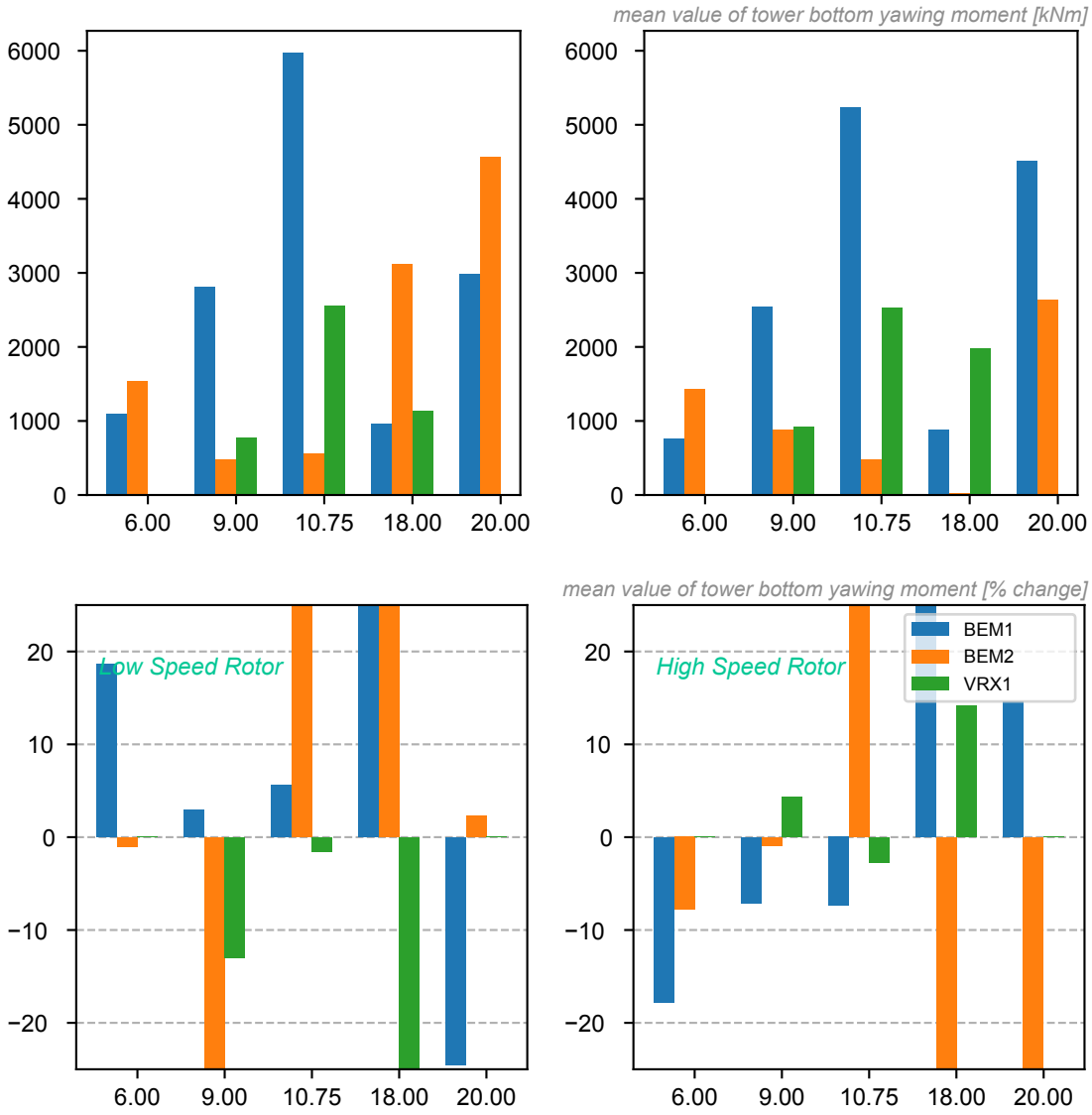

Figure 39: Absolute and Relative effect of rotational speed on the mean value of the tower bottom yawing moment for DLC1.2

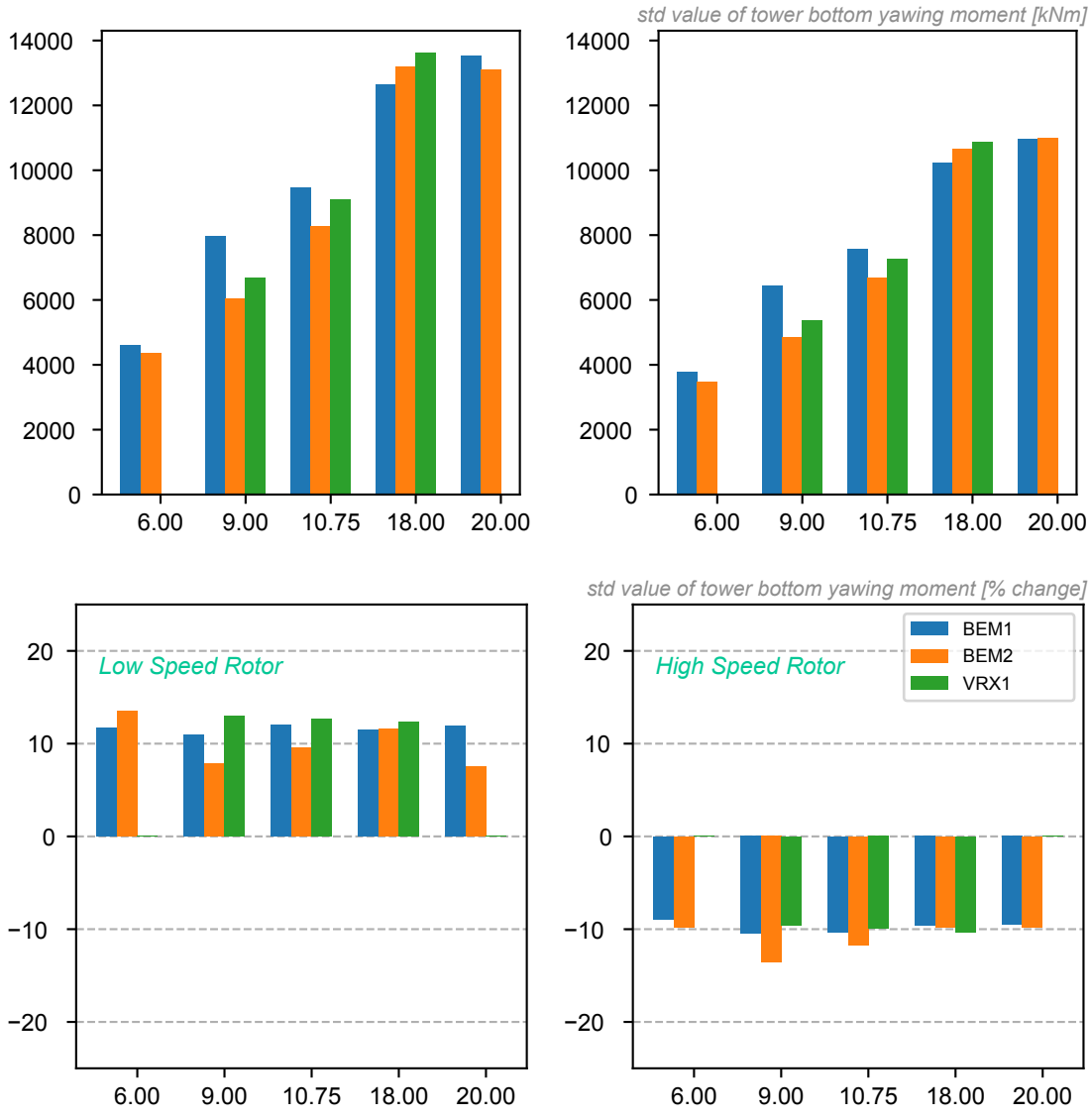

Figure 40: Absolute and Relative effect of rotational speed on tower bottom yawing moment for DLC1.2

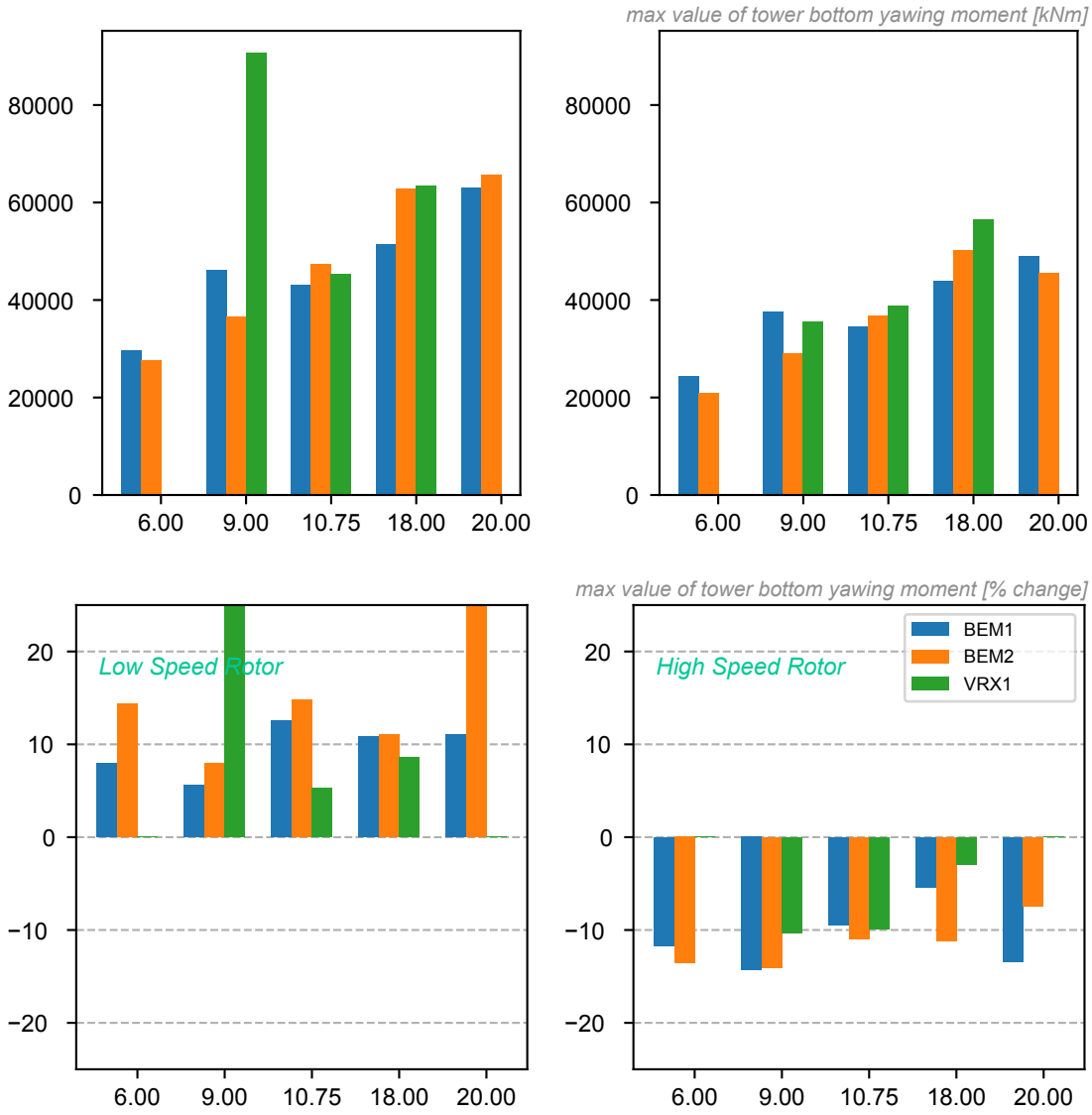

Figure 41: Absolute and Relative effect of rotational speed on the max value of the tower bottom yawing moment for DLC1.3

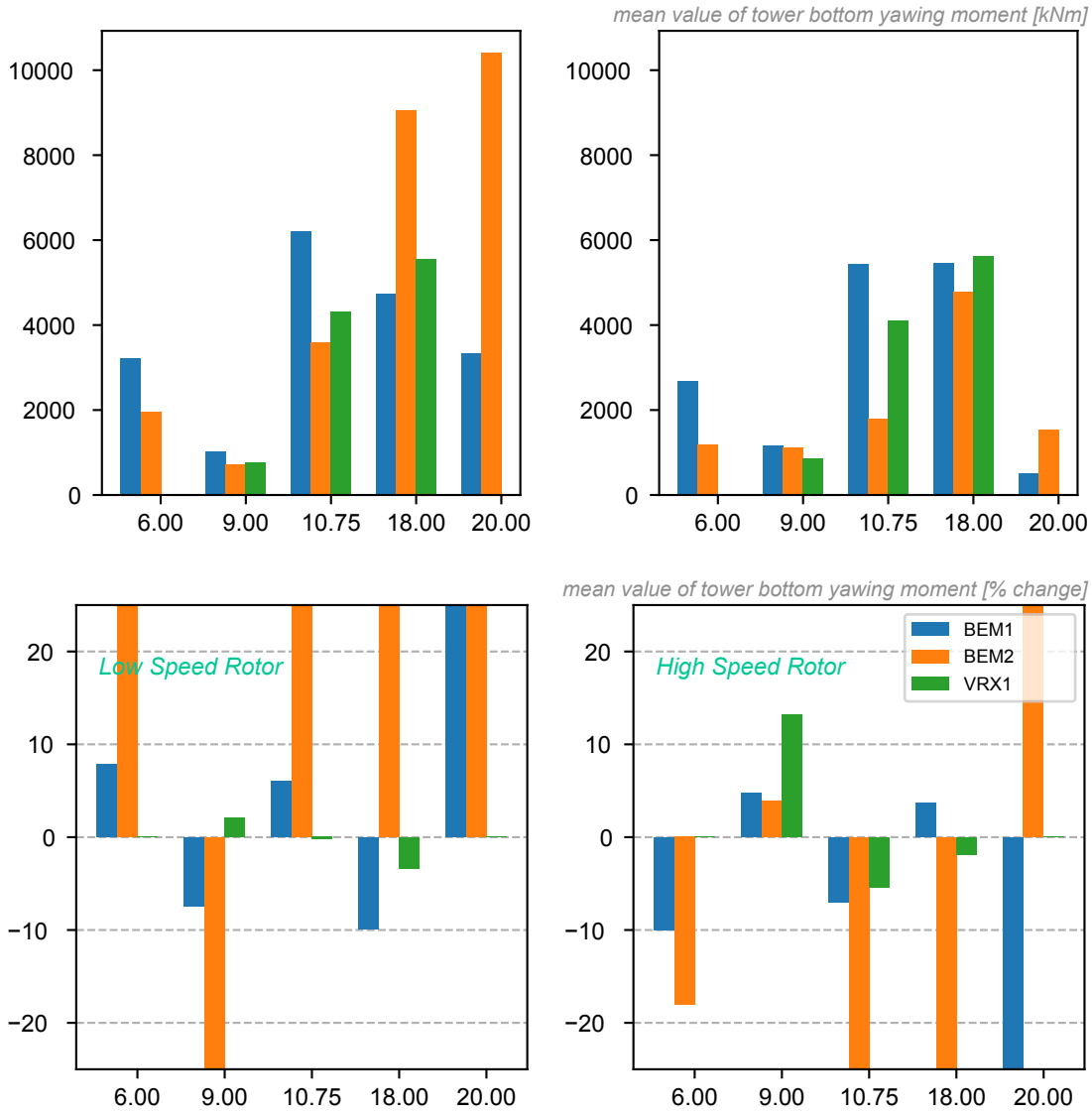

Figure 42: Absolute and Relative effect of rotational speed on the mean value of the tower bottom yawing moment for DLC1.3

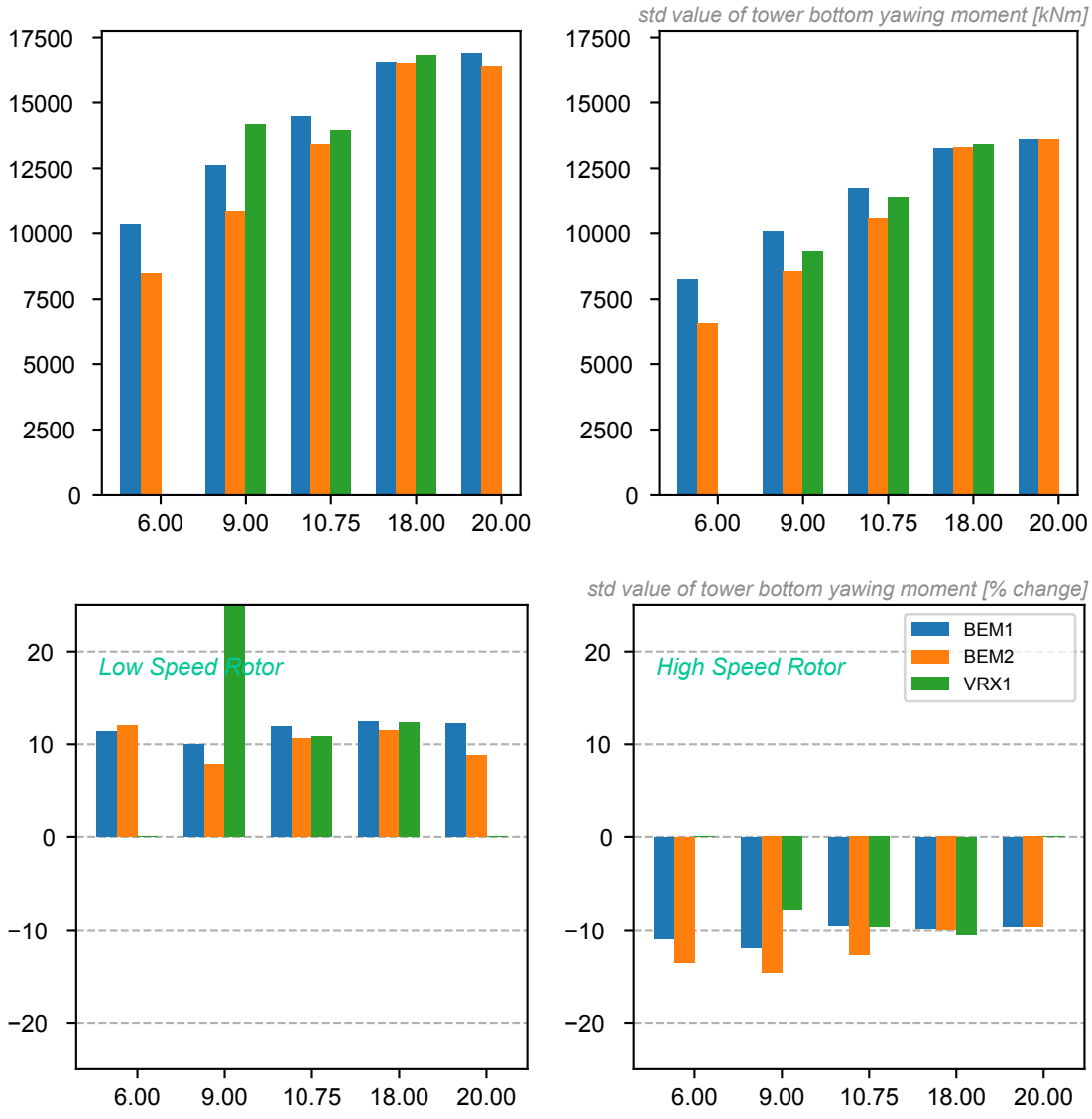

Figure 43: Absolute and Relative effect of rotational speed on tower bottom yawing moment for DLC1.3

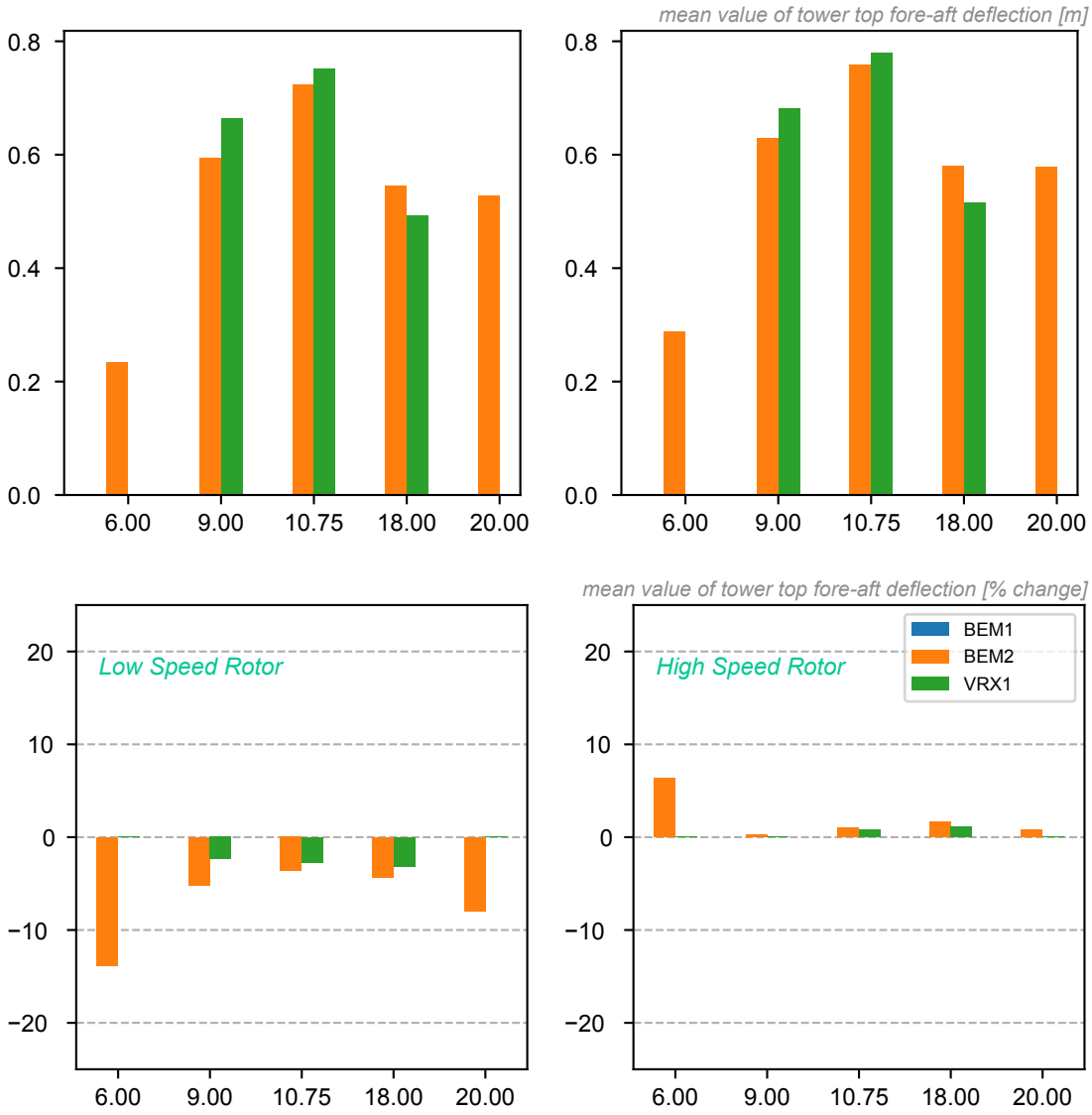

Figure 44: Absolute and Relative effect of rotational speed on the mean value of the tower top fore-aft deflection for DLC1.2

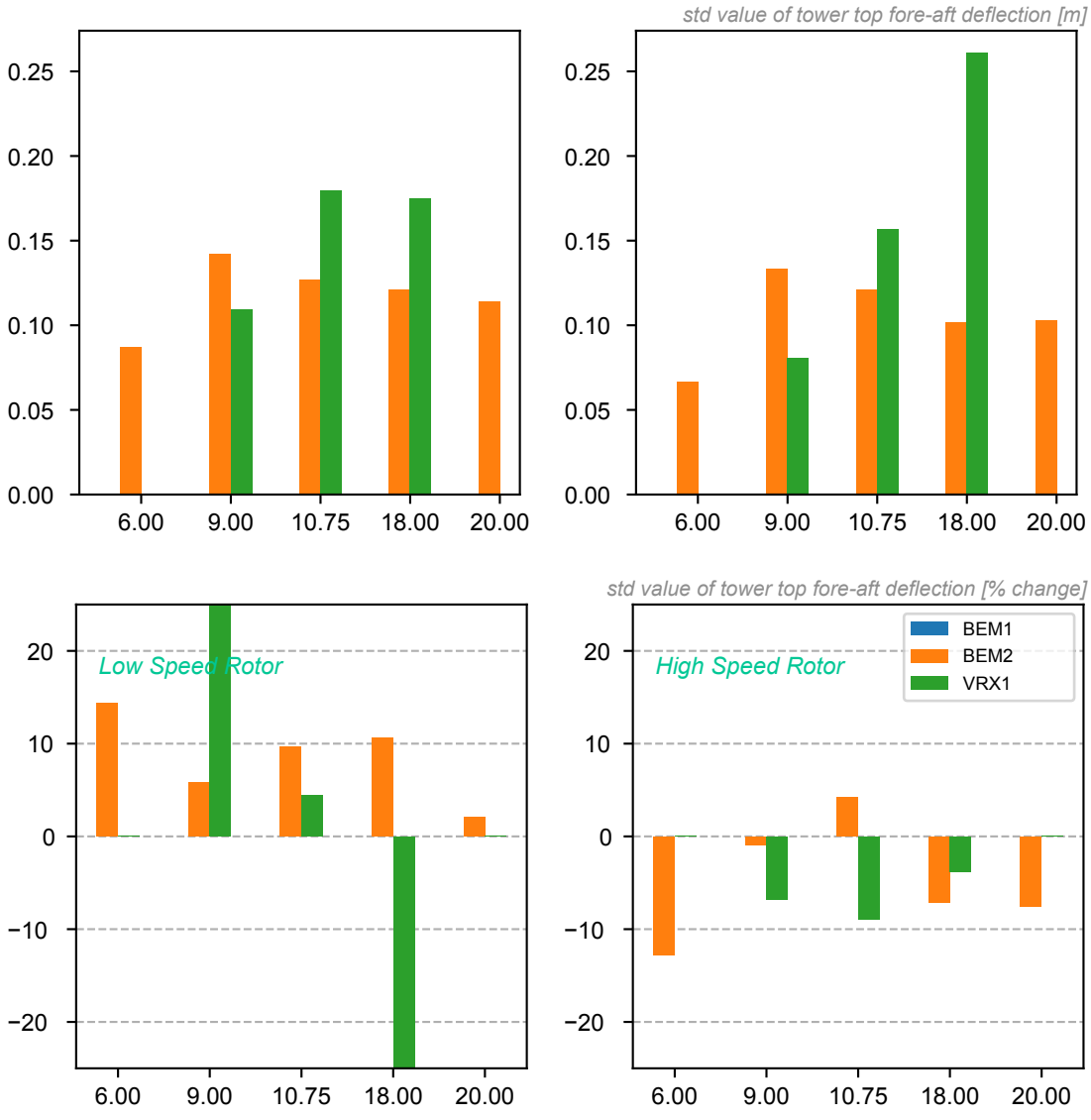

Figure 45: Absolute and Relative effect of rotational speed on tower top fore-aft deflection for DLC1.2

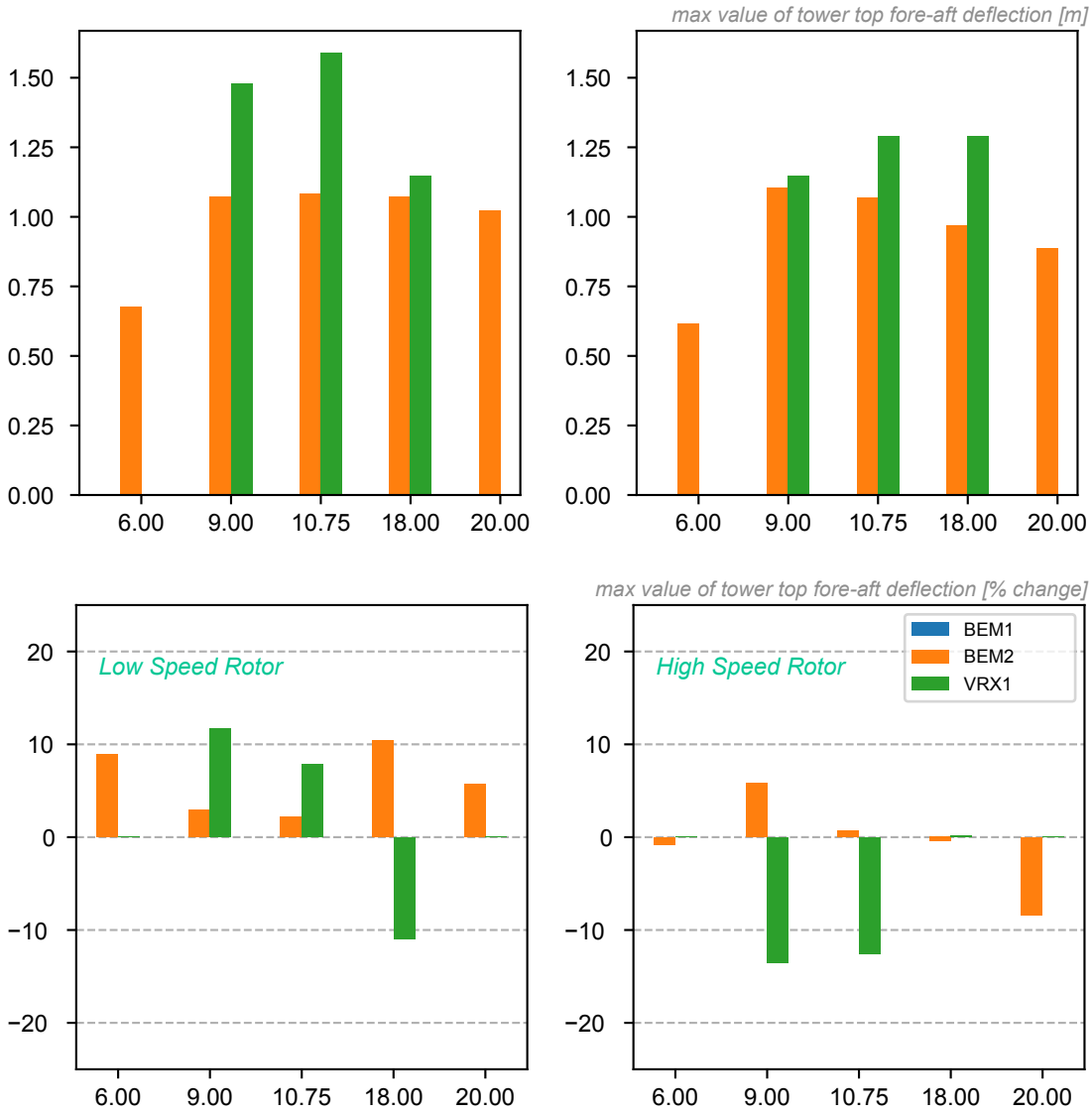

Figure 46: Absolute and Relative effect of rotational speed on the max value of the tower top fore-aft deflection for DLC1.3

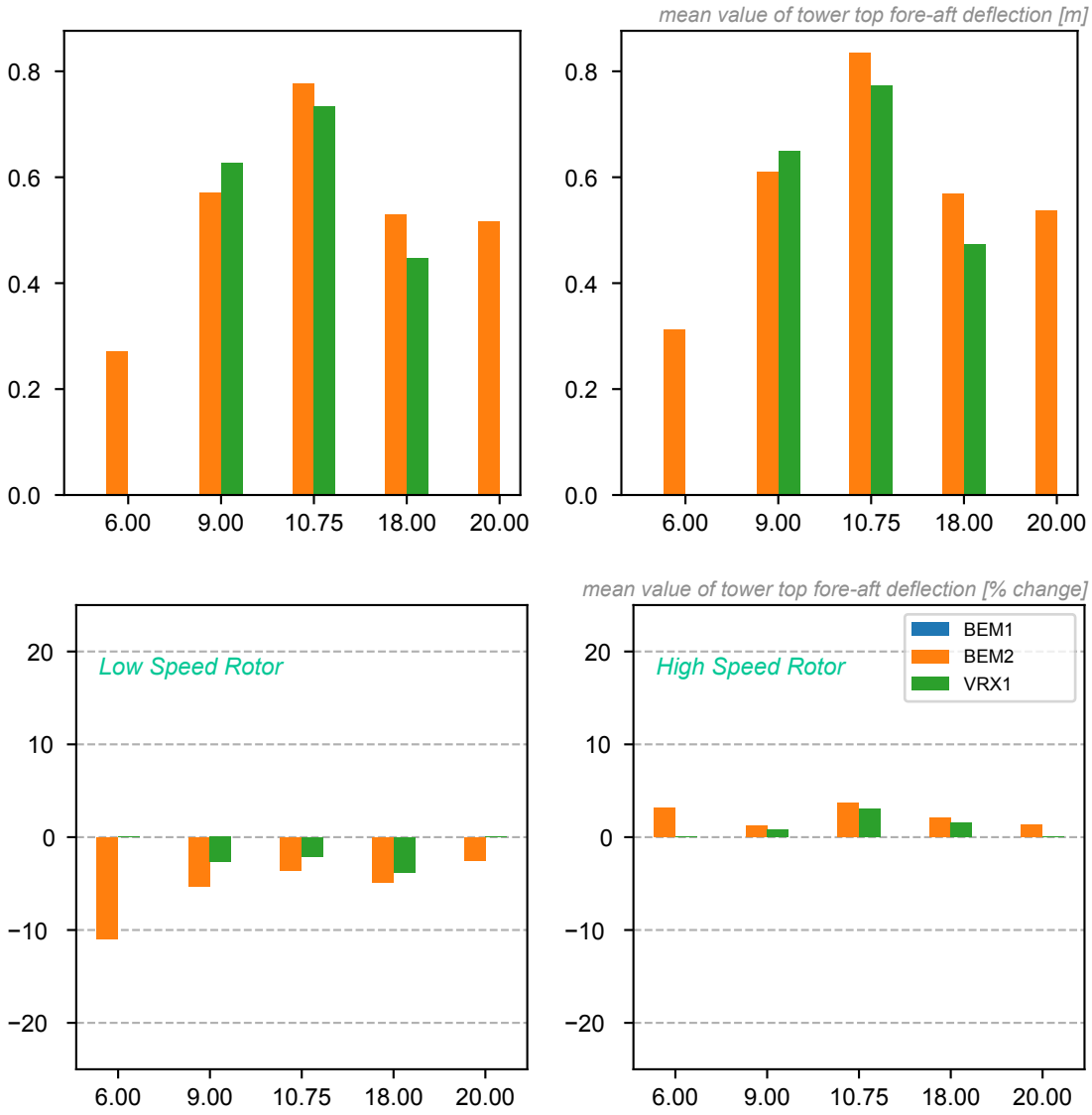

Figure 47: Absolute and Relative effect of rotational speed on the mean value of the tower top fore-aft deflection for DLC1.3

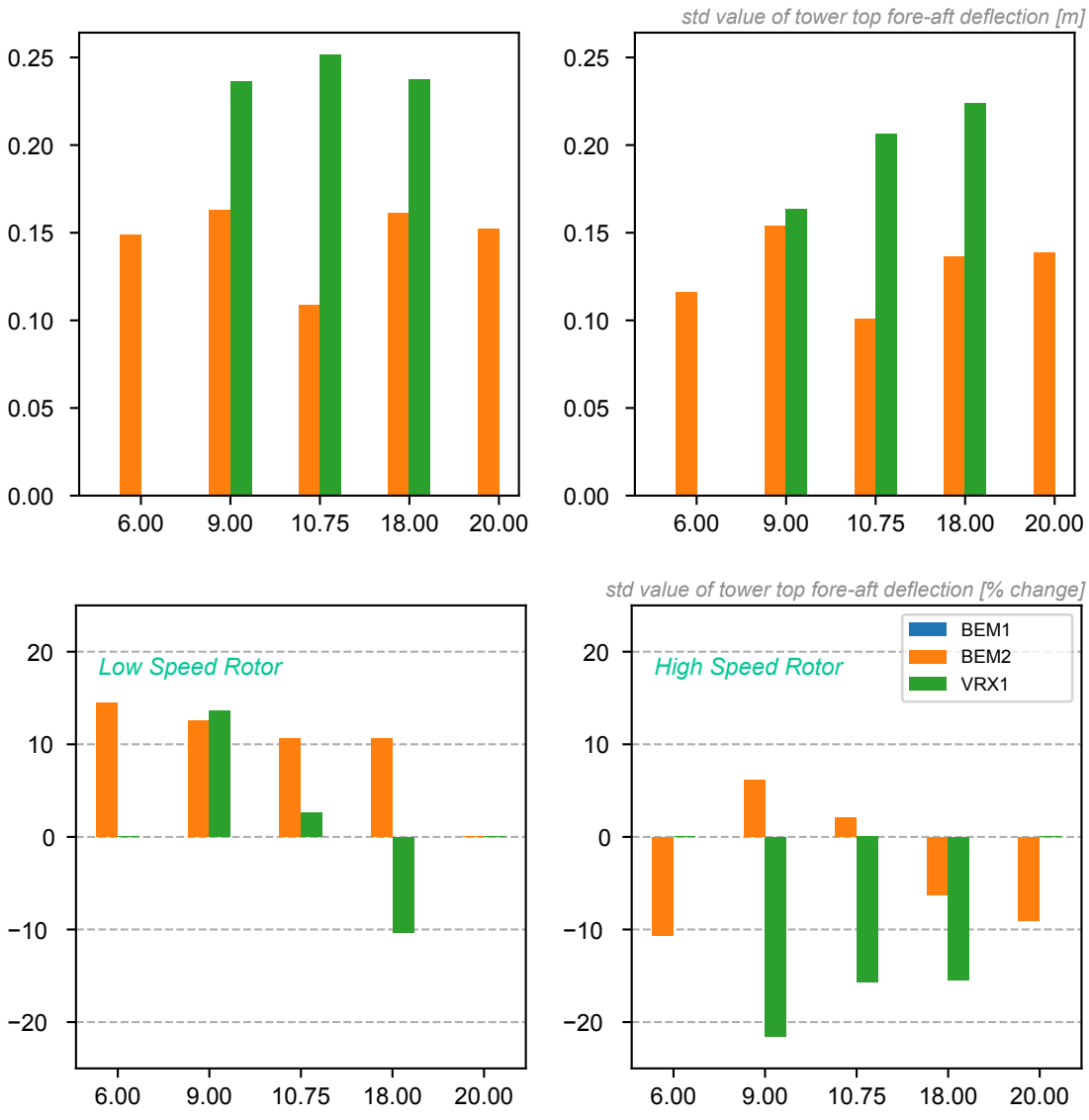

Figure 48: Absolute and Relative effect of rotational speed on tower top fore-aft deflection for DLC1.3

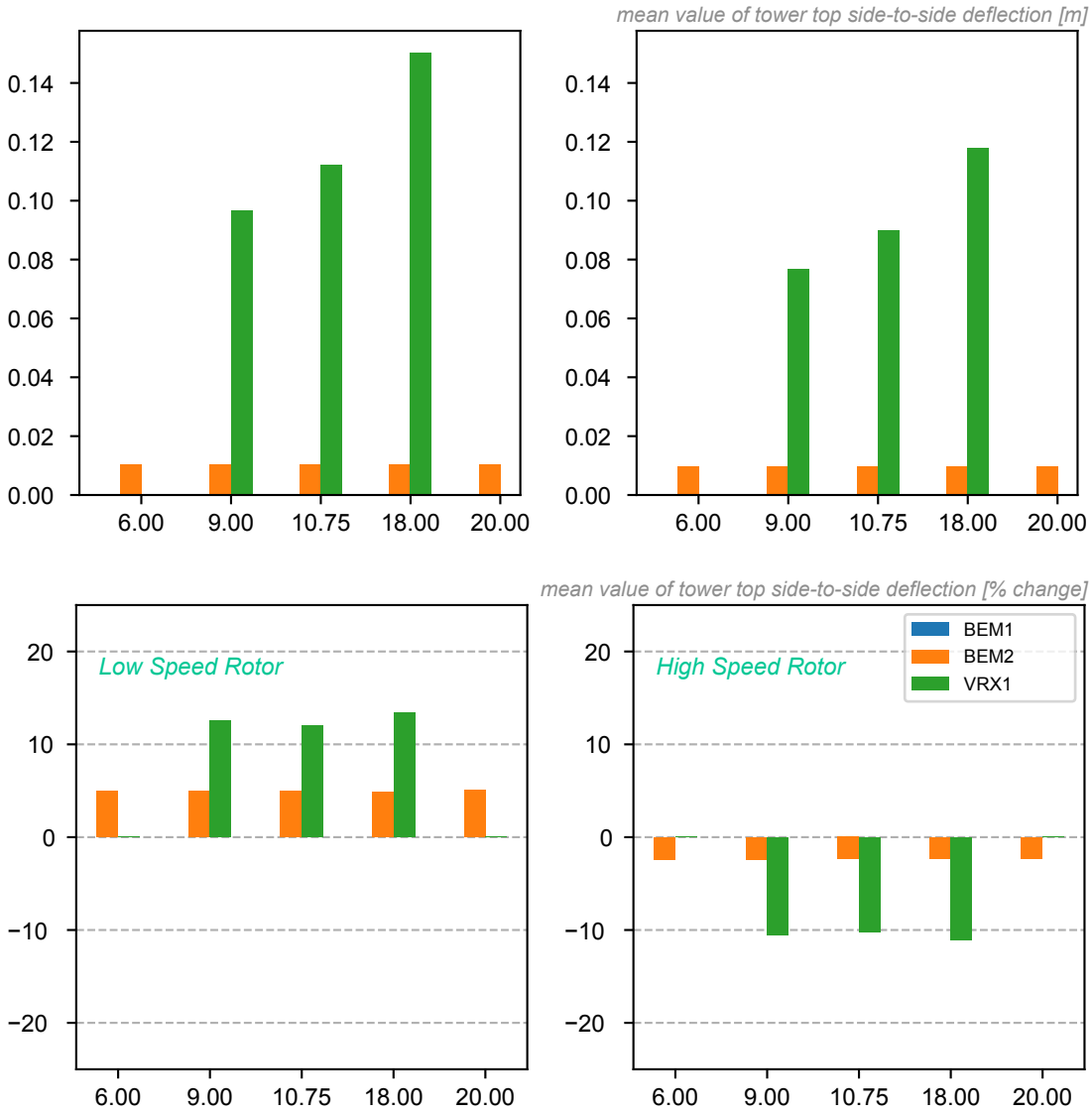

Figure 49: Absolute and Relative effect of rotational speed on the mean value of the tower top side-to-side deflection for DLC1.2

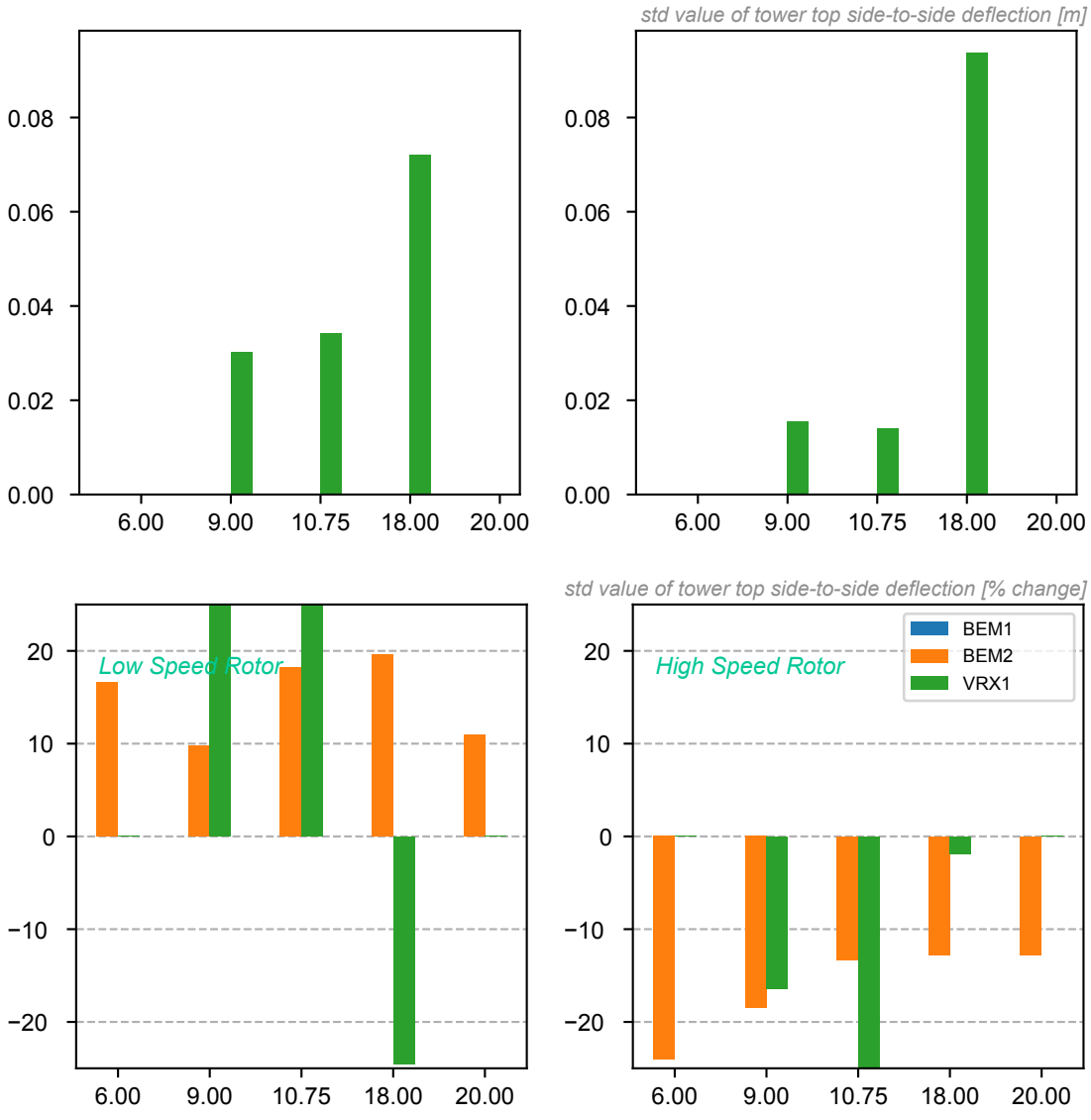

Figure 50: Absolute and Relative effect of rotational speed on tower top side-to-side deflection for DLC1.2

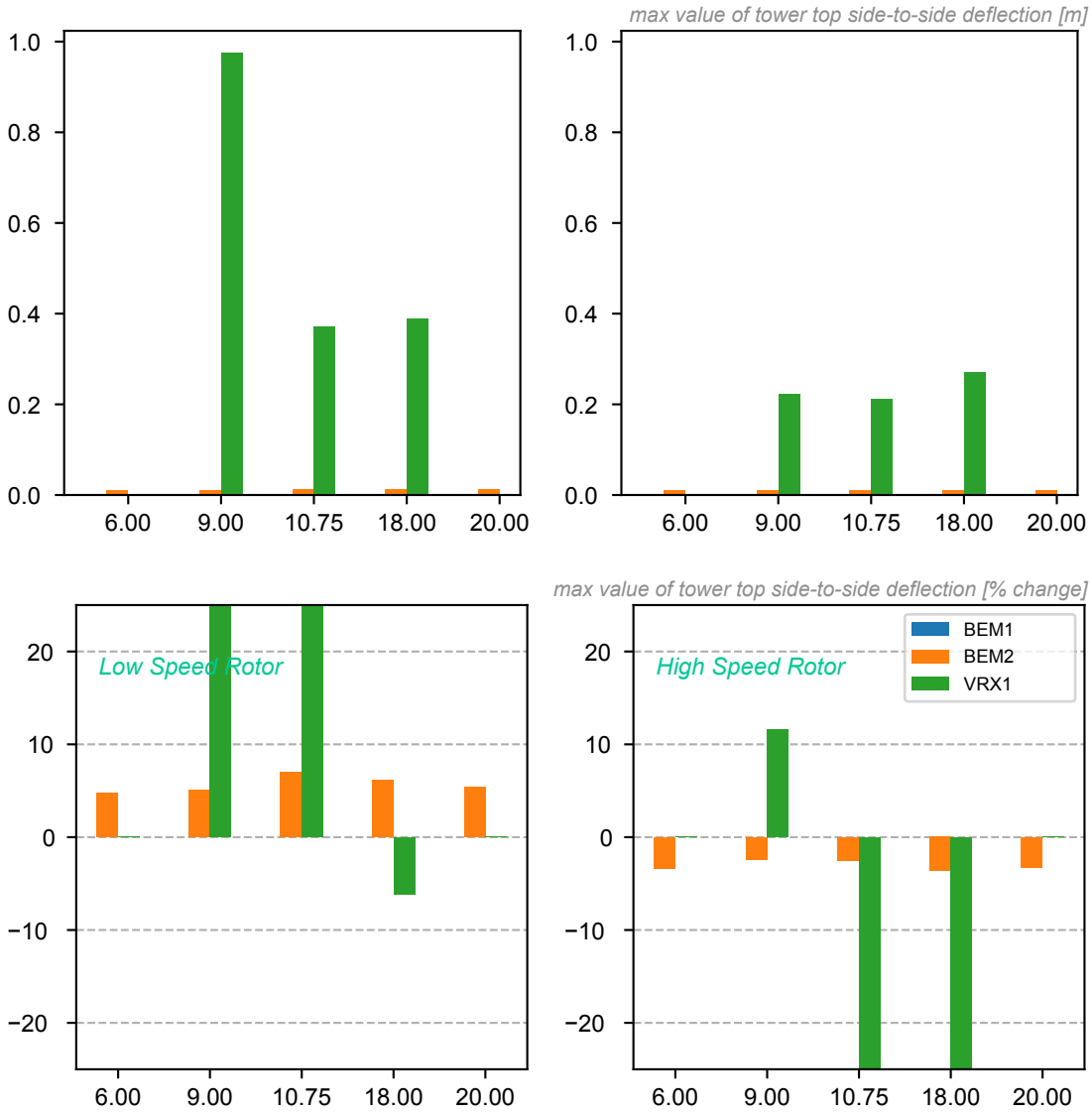

Figure 51: Absolute and Relative effect of rotational speed on the max value of the tower top side-to-side deflection for DLC1.3

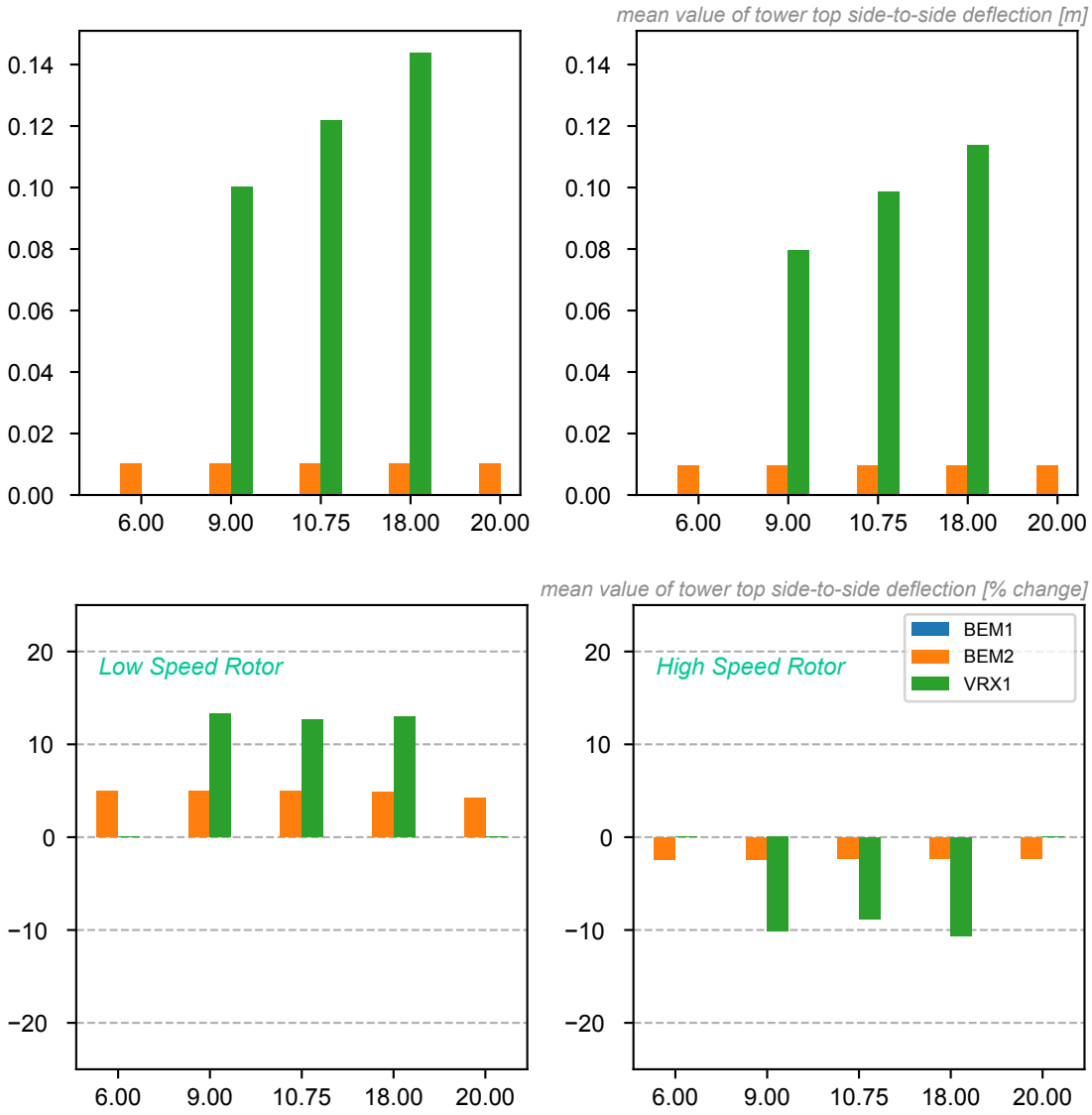

Figure 52: Absolute and Relative effect of rotational speed on the mean value of the tower top side-to-side deflection for DLC1.3

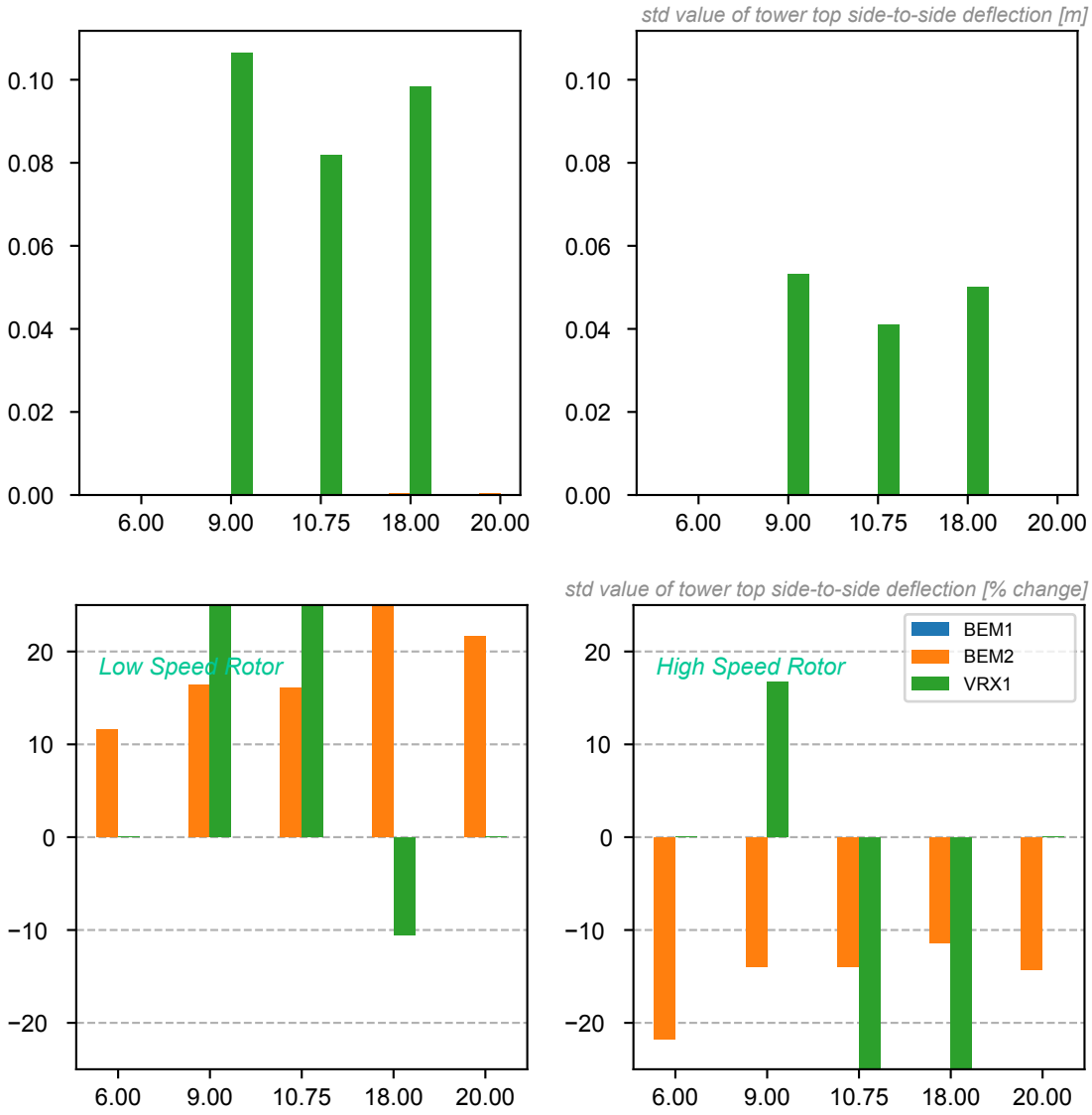

Figure 53: Absolute and Relative effect of rotational speed on the sdv value of the tower top side-to-side deflection for DLC1.3

4.3.3 Shaft Loads

The calculated torque at the shaft is given in the following. The results are consistent with the design procedure, showing an increase of ∼10 % for the low-speed rotor and a similar decrease for the high-speed rotor. This applies to both normal and extreme turbulence simulations, for mean and maximum torque values (figs. 54, 56 and 57). There are larger deviations between the codes in the simulation of the standard deviation of the torque (figs. 55 and 58), but the trend appears similar.

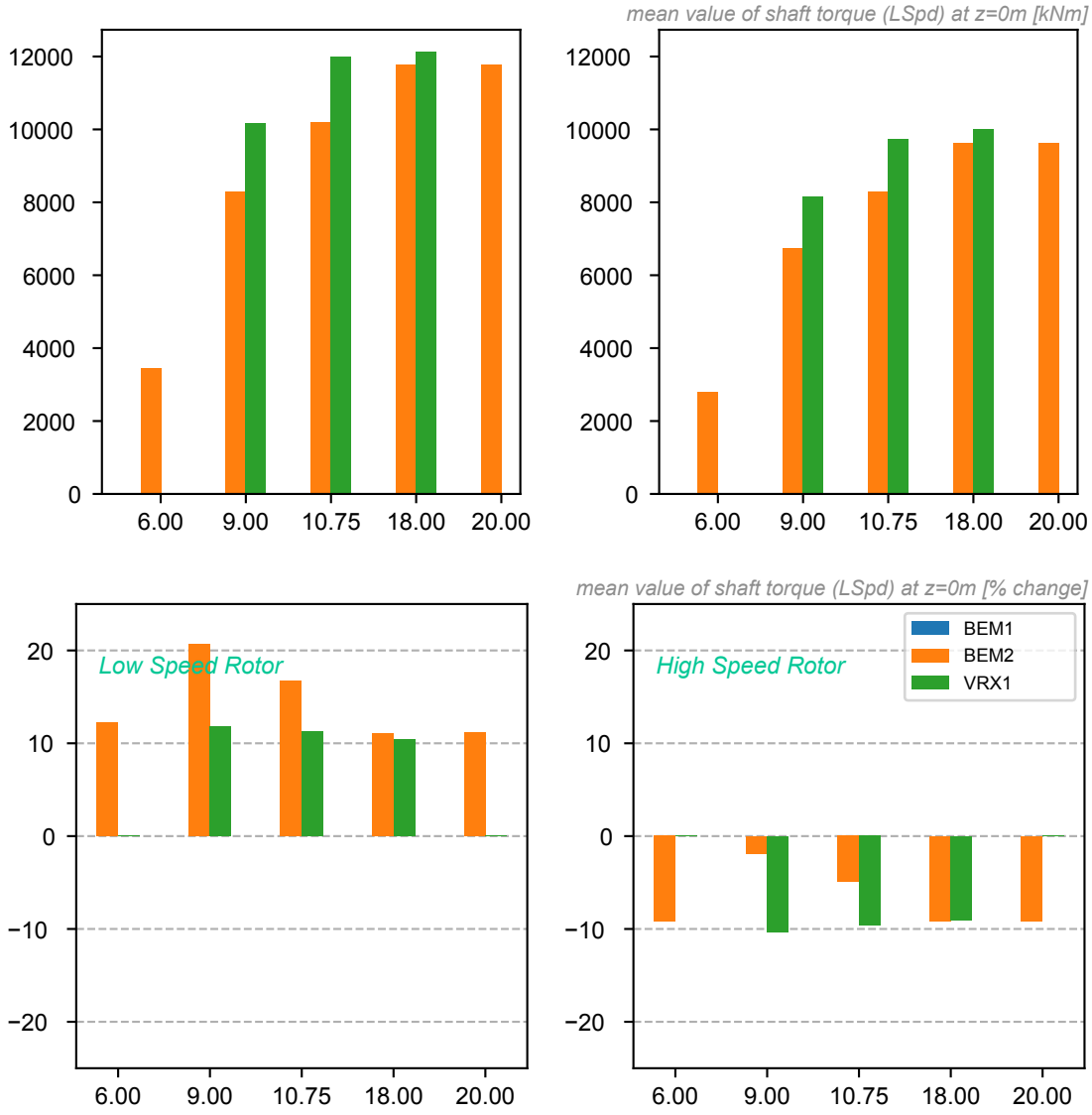

Figure 54: Absolute and Relative effect of rotational speed on the mean value of the shaft torque (LSpd) at z=0m for DLC1.2

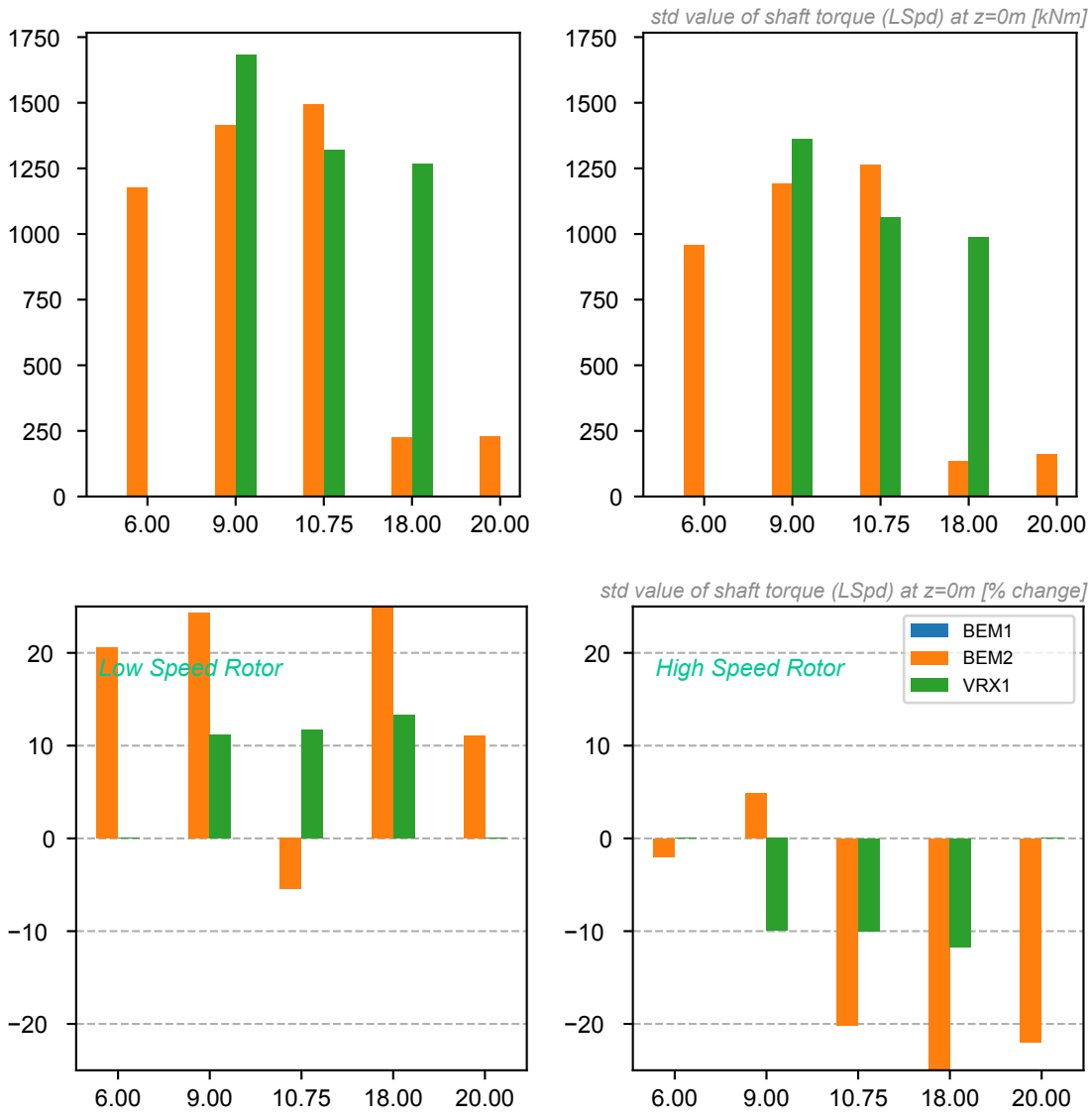

Figure 55: Absolute and Relative effect of rotational speed on shaft torque (LSpd) at z=0m for DLC1.2

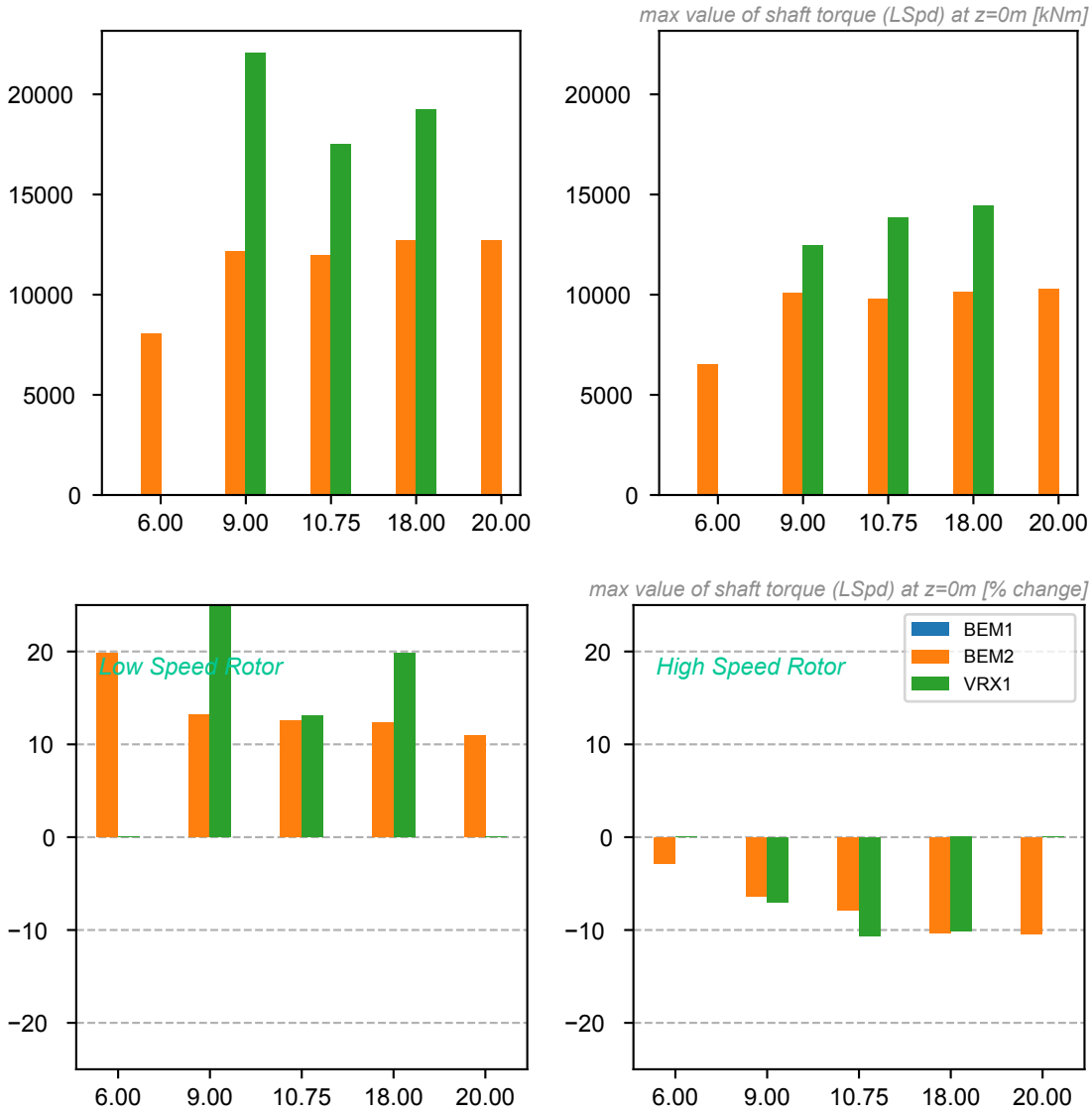

Figure 56: Absolute and Relative effect of rotational speed on the max value of the shaft torque (LSpd) at z=0m for DLC1.3

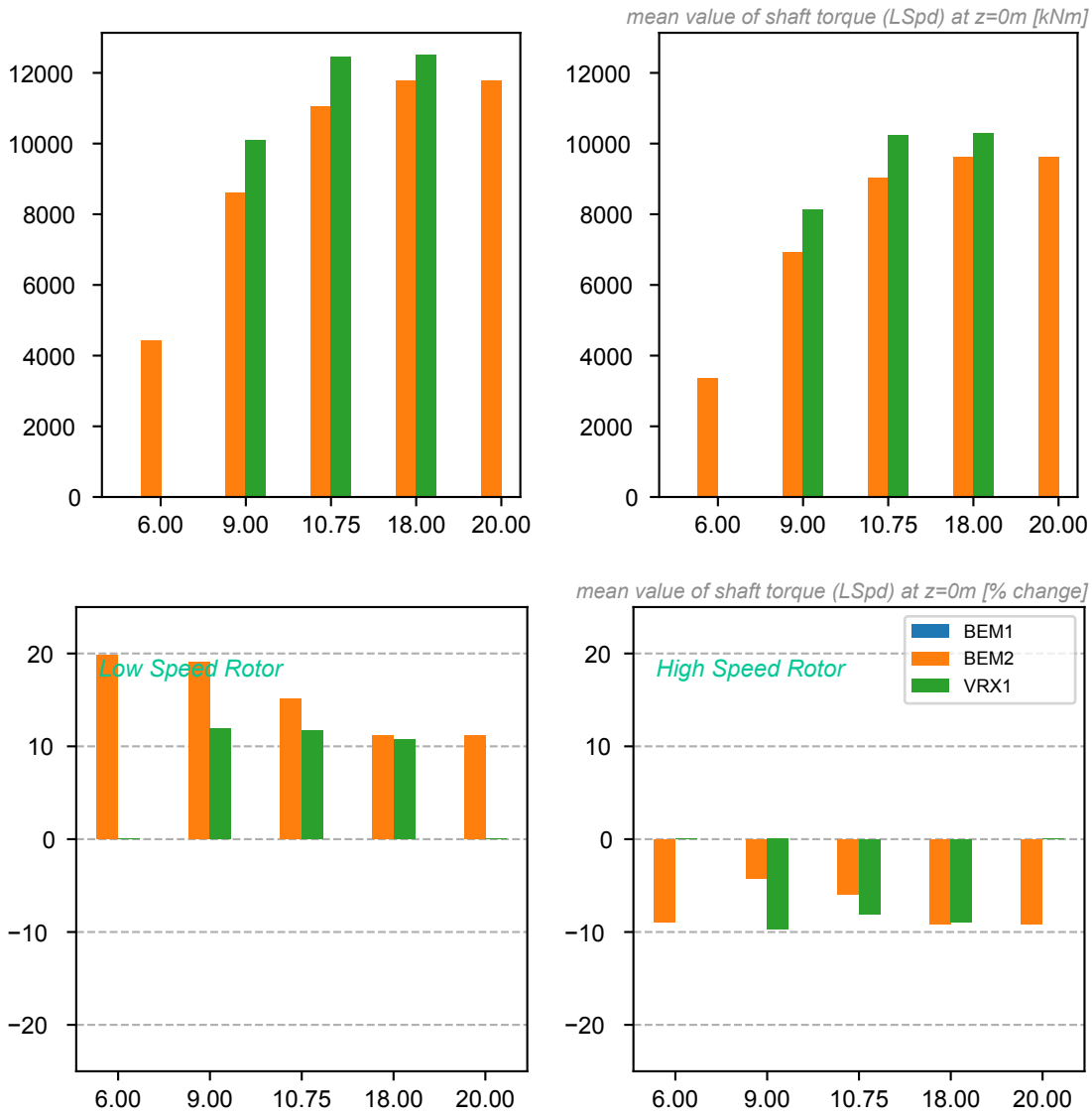

Figure 57: Absolute and Relative effect of rotational speed on the mean value of the shaft torque (LSpd) at z=0m for DLC1.3

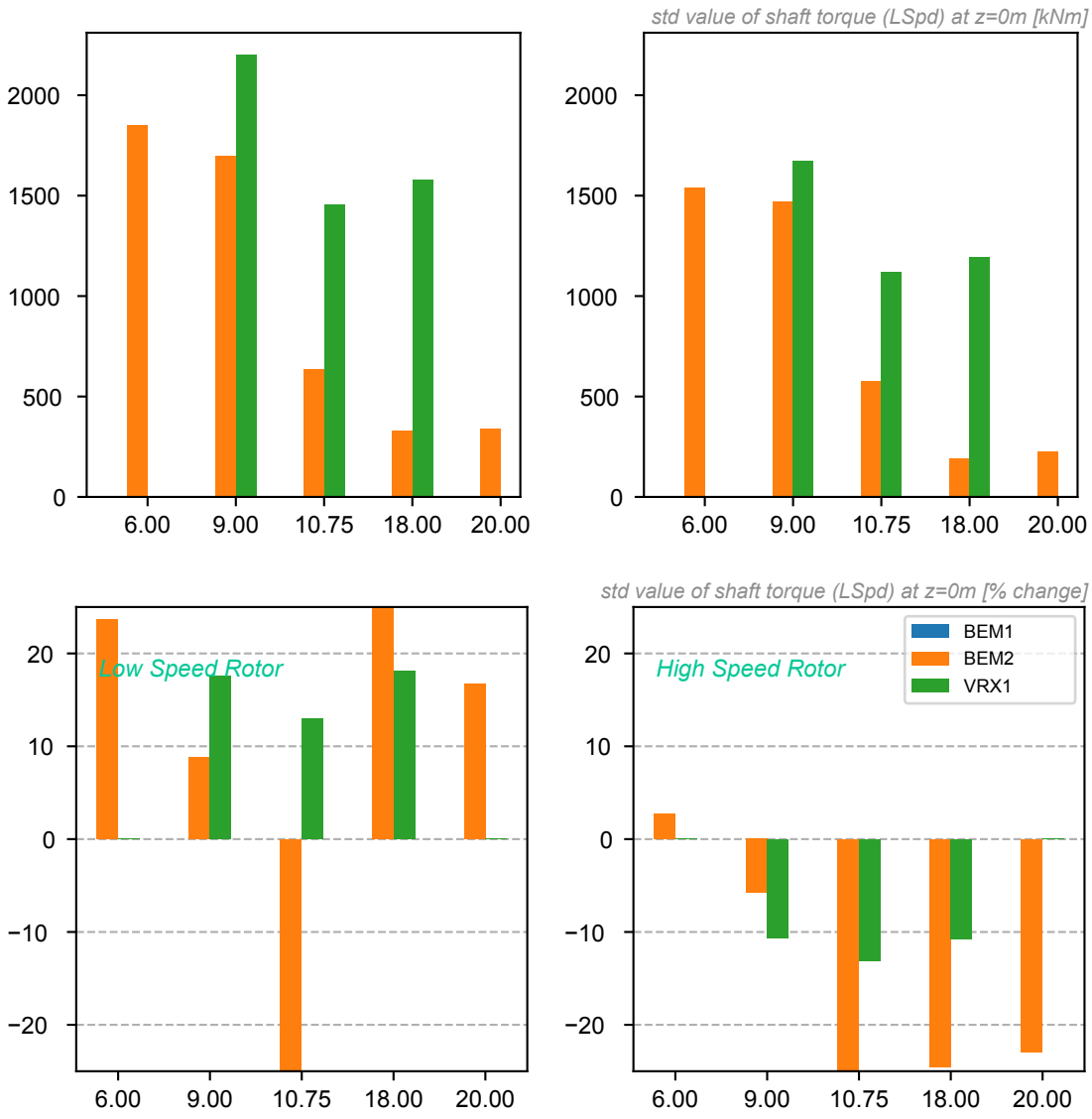

Figure 58: Absolute and Relative effect of rotational speed on shaft torque (LSpd) at z=0m for DLC1.3

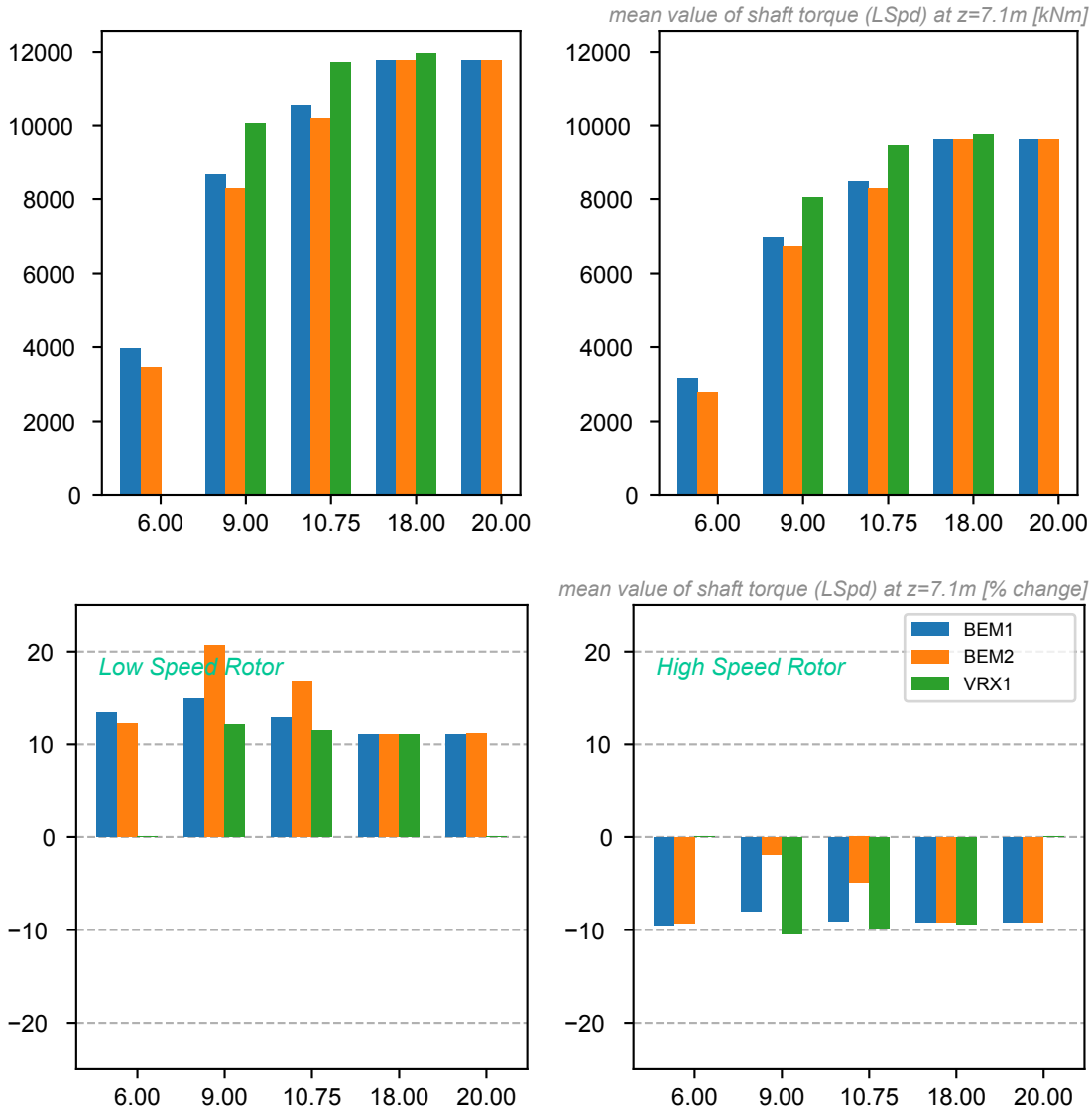

Figure 59: Absolute and Relative effect of rotational speed on the mean value of the shaft torque (LSpd) at z=7.1m for DLC1.2

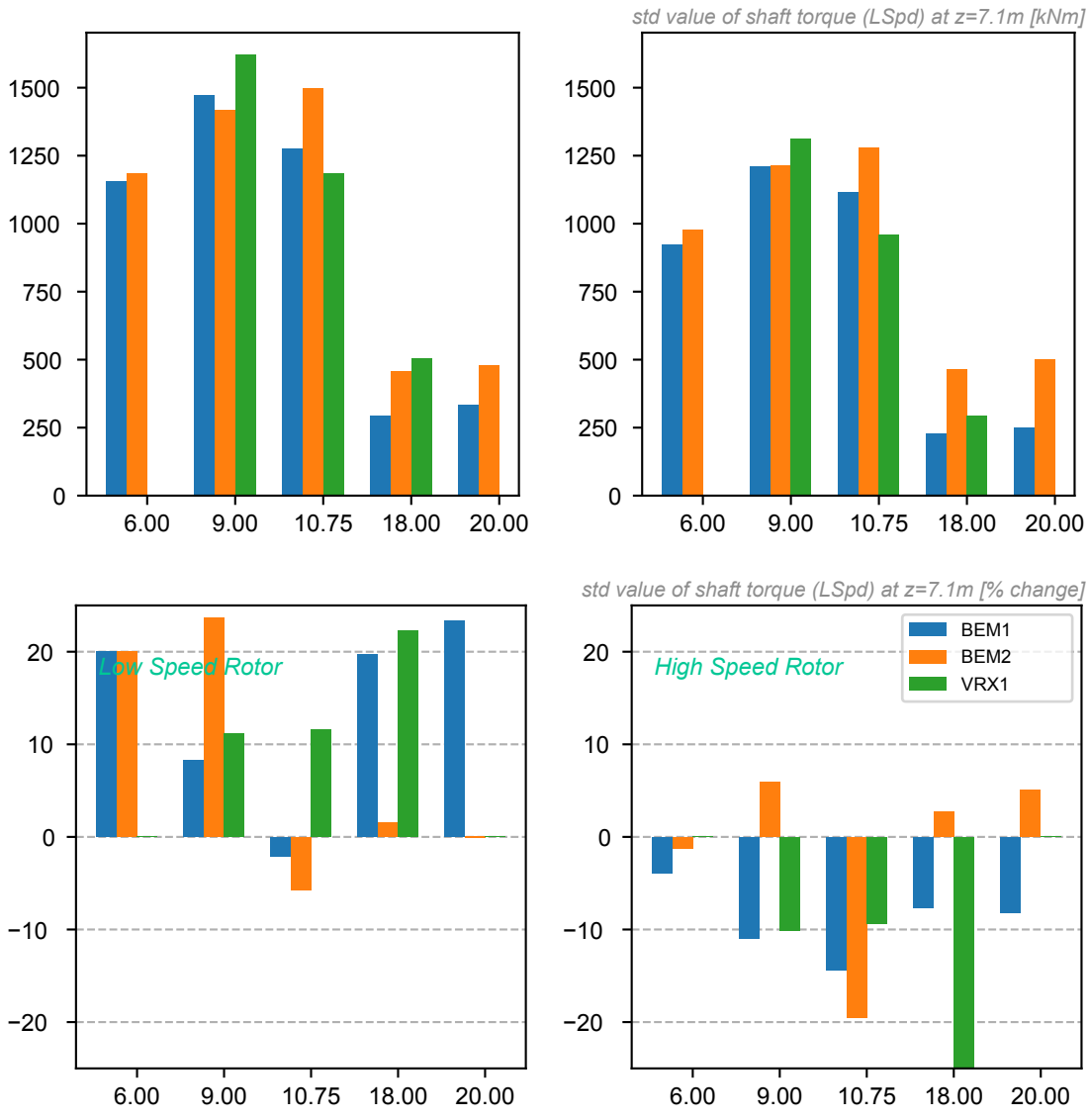

Figure 60: Absolute and Relative effect of rotational speed on shaft torque (LSpd) at z=7.1m for DLC1.2

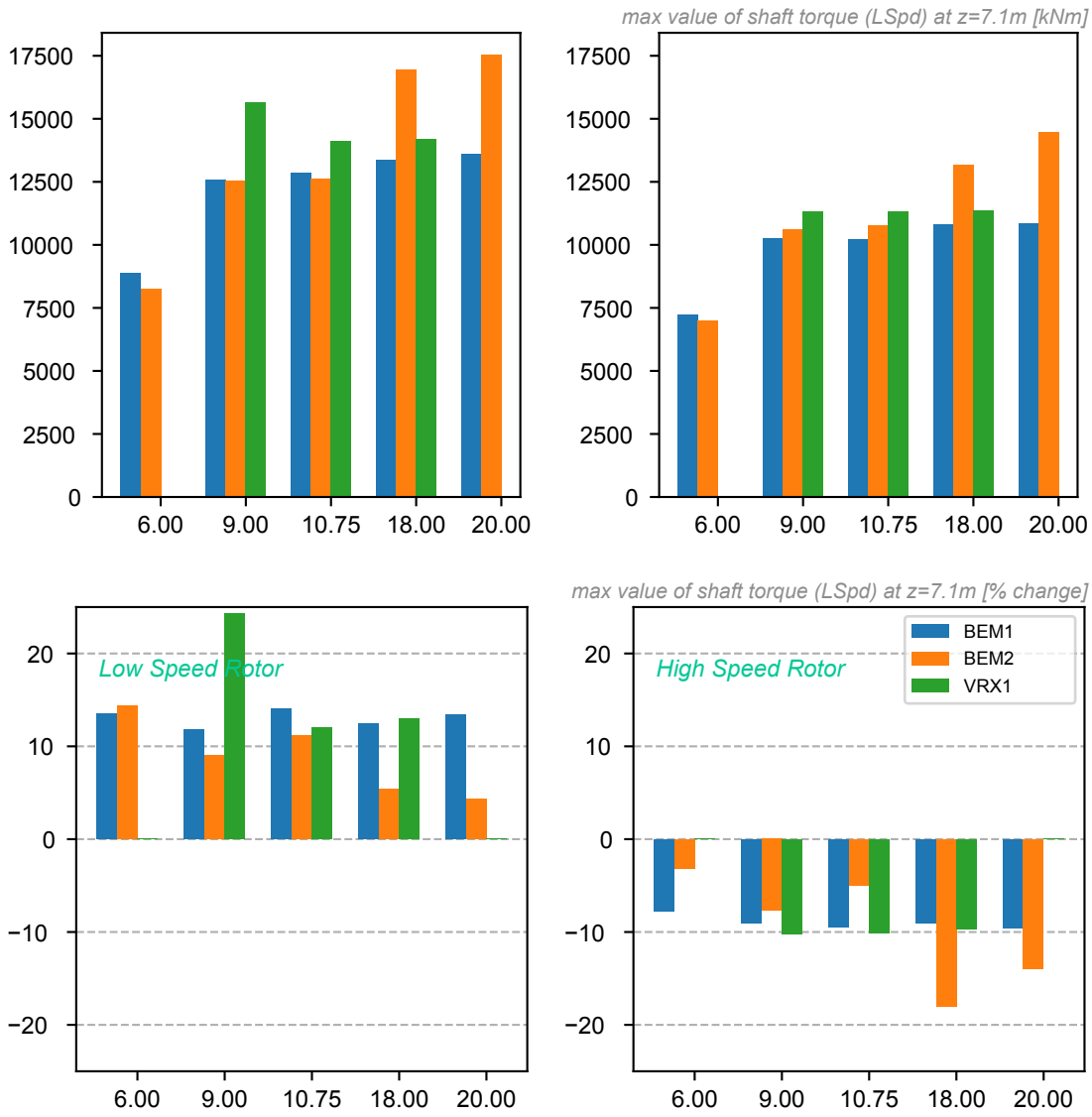

Figure 61: Absolute and Relative effect of rotational speed on the max value of the shaft torque (LSpd) at z=7.1m for DLC1.3

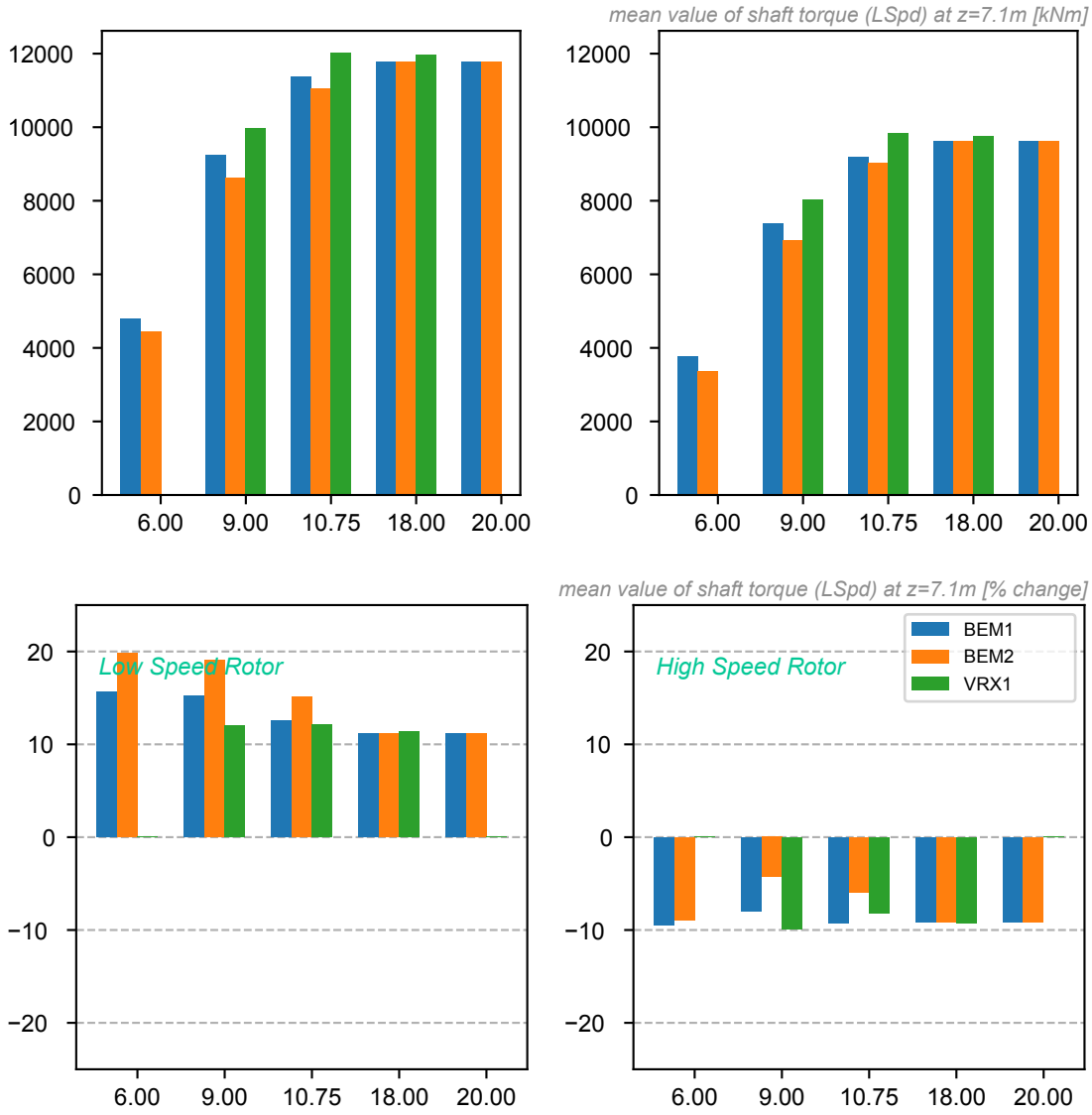

Figure 62: Absolute and Relative effect of rotational speed on the mean value of the shaft torque (LSpd) at z=7.1m for DLC1.3

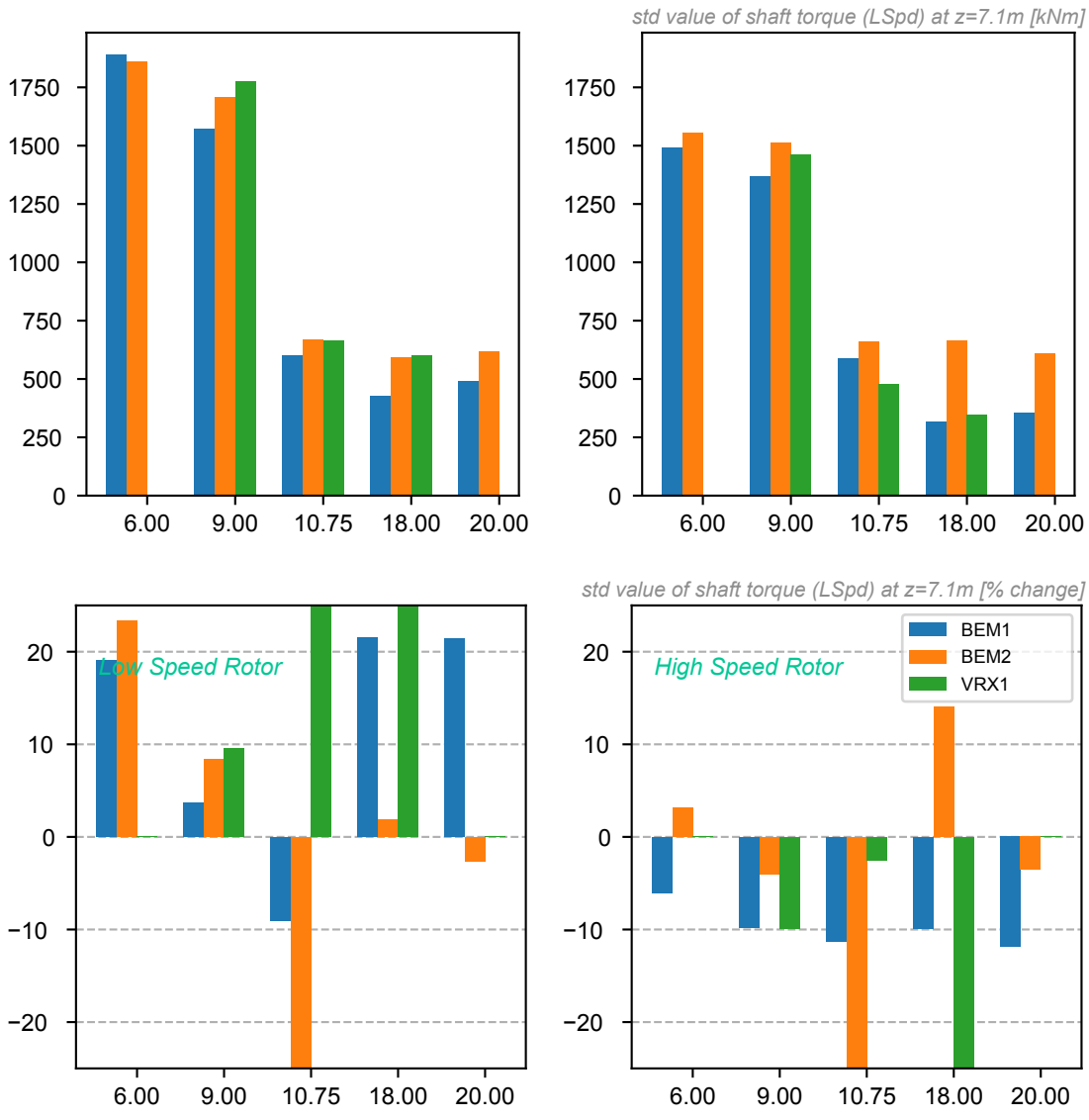

Figure 63: Absolute and Relative effect of rotational speed on shaft torque (LSpd) at z=7.1m for DLC1.3

4.3.4 Blade Loads

The final set of results corresponds to the blade loads. We present the flapwise and edgewise bending moments at the blade root, along with the deflections near the blade tip (at 95 % of the blade). The mean flapwsise loads are not significantly affected by the change in roting speed, as seen in figs. 64 and 67.The maximum value and the standard deviation on the other hand (figs. 65, 66 and 68) decrease with increasing rotating speed.

For the edgewise load, there is a much bigger impact. with mean loads, maximum loads and load variation decreasing with rotating speed (figs. 69 to 73). As the edgewise loads are largely weight driven, it is expected that the heavier low-speed rotor will exhibit larger loads in this direction. For the same reasons the pitching moment increases cosiderably for the low-speed rotor (figs. 74 to 78)

For the blade deflections we see that the flapwise deflection shows an increase in mean value for the lighter high-speed rotor. The edgewise deflection does not show a clear dependence on rotating speed, though the *variation* decreases with speed.

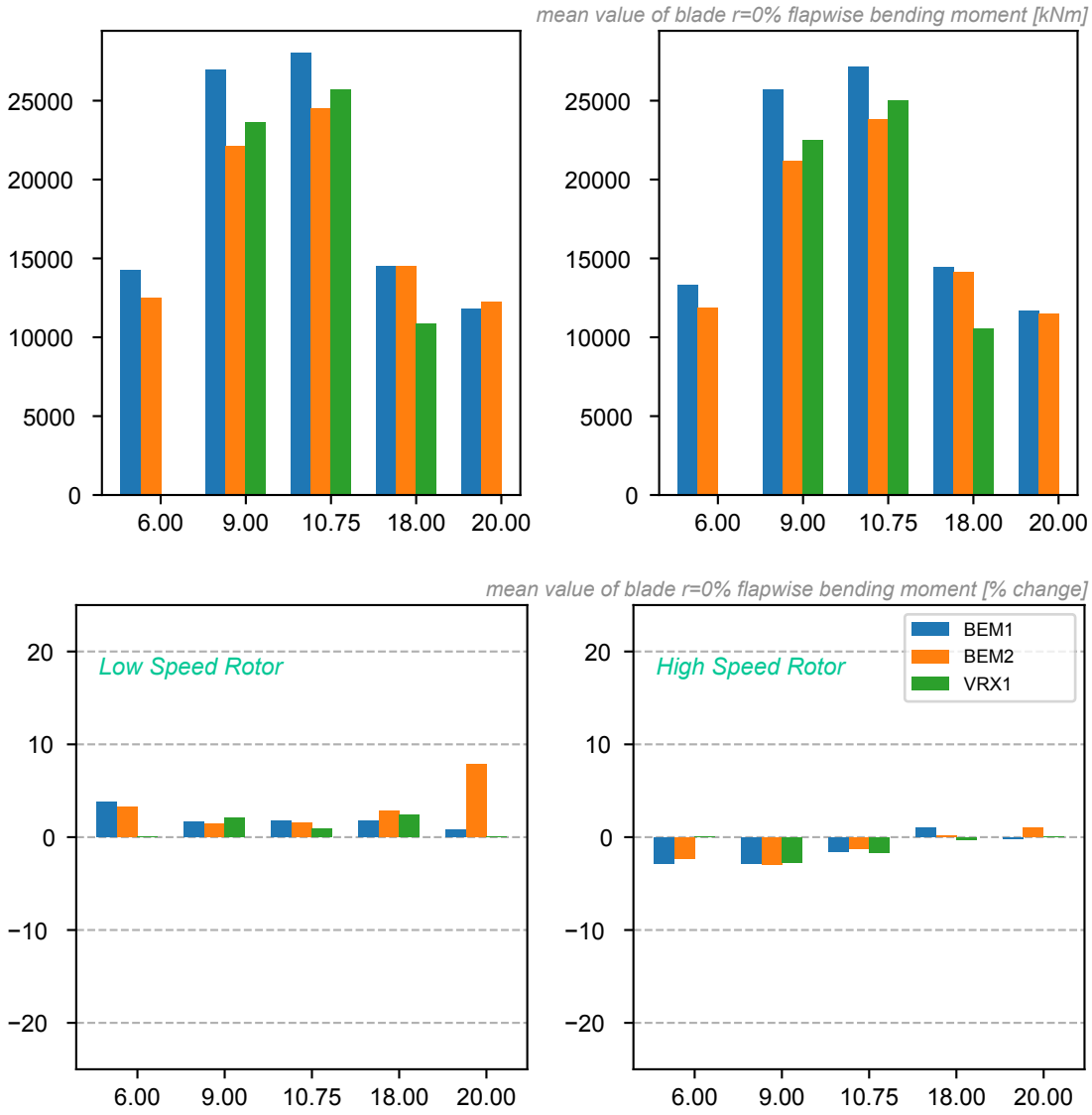

Figure 64: Absolute and Relative effect of rotational speed on the mean value of the blade flapwise bending moment at r=0% for DLC1.2

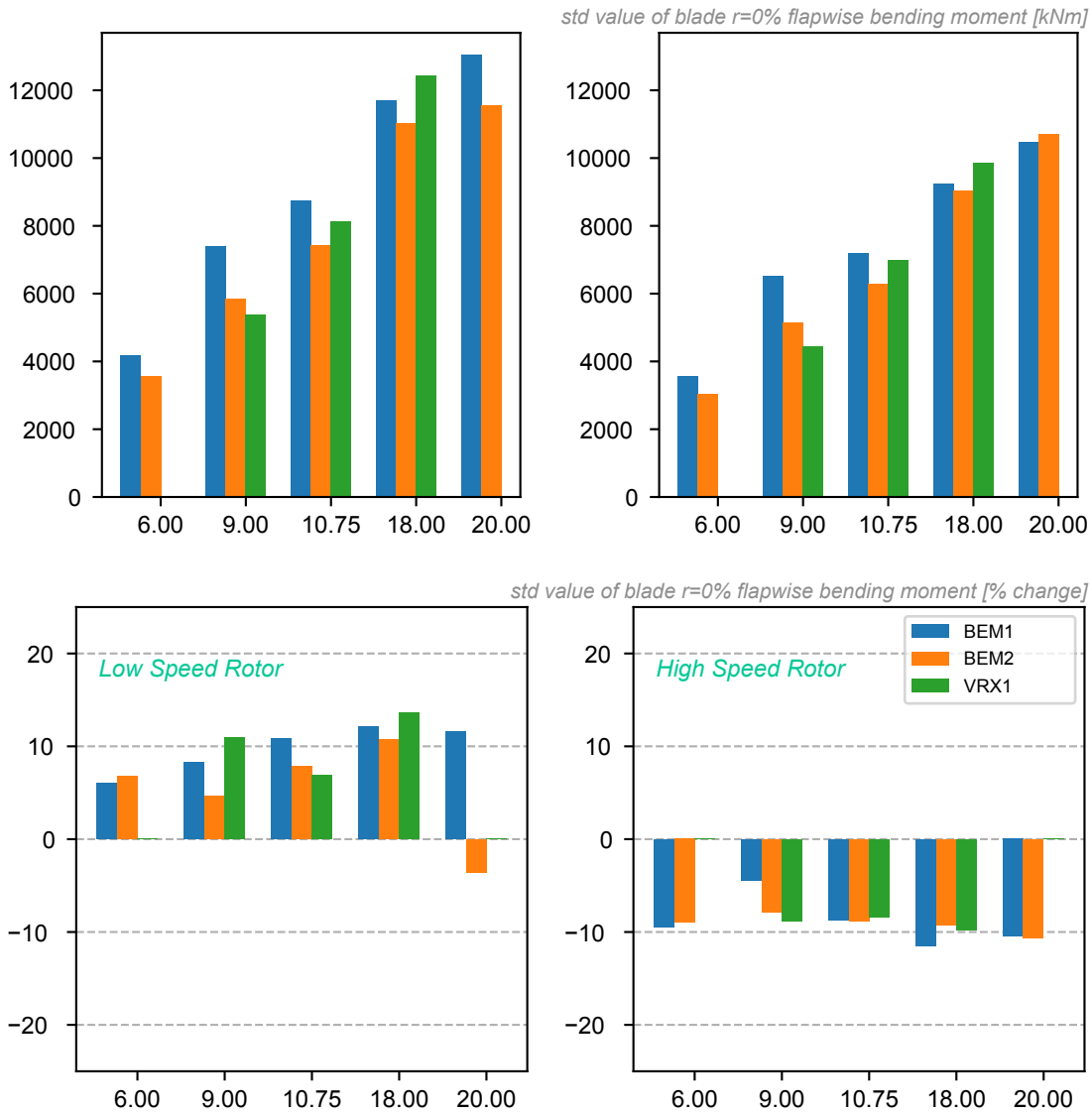

Figure 65: Absolute and Relative effect of rotational speed on blade flapwise bending moment at r=0% for DLC1.2

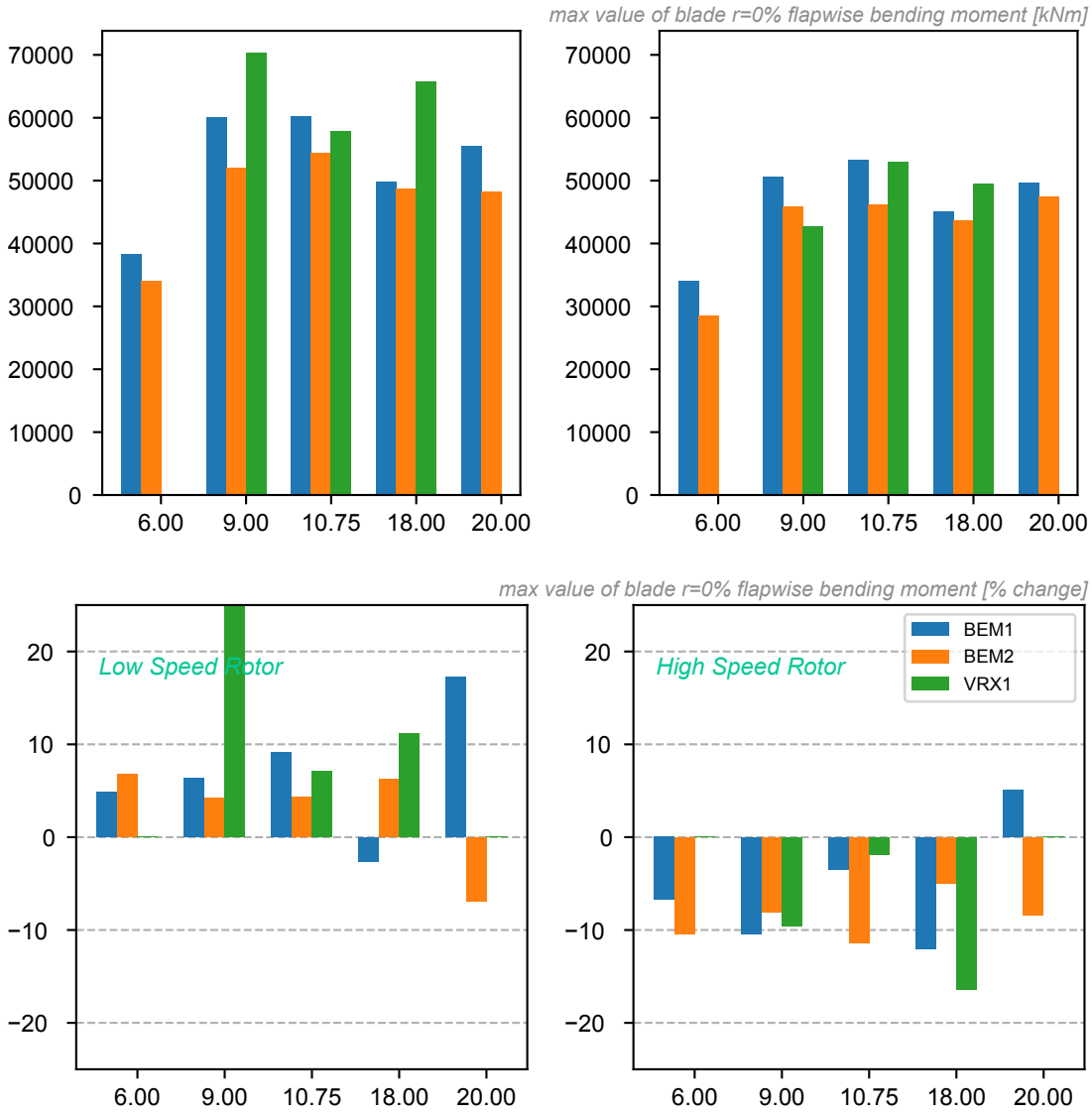

Figure 66: Absolute and Relative effect of rotational speed on the max value of the blade flapwise bending moment at r=0% for DLC1.3

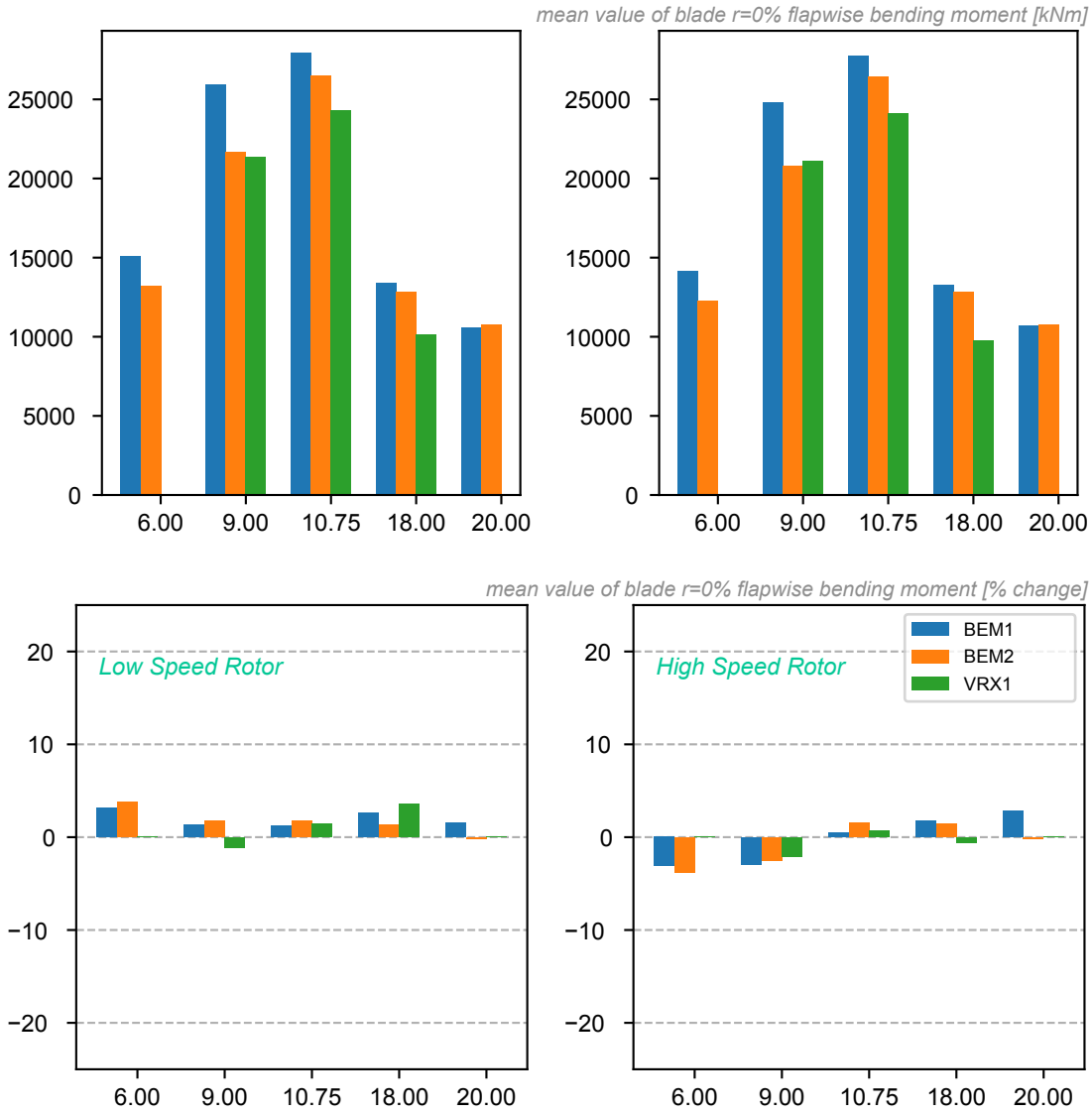

Figure 67: Absolute and Relative effect of rotational speed on the mean value of the blade flapwise bending moment r=0% for DLC1.3

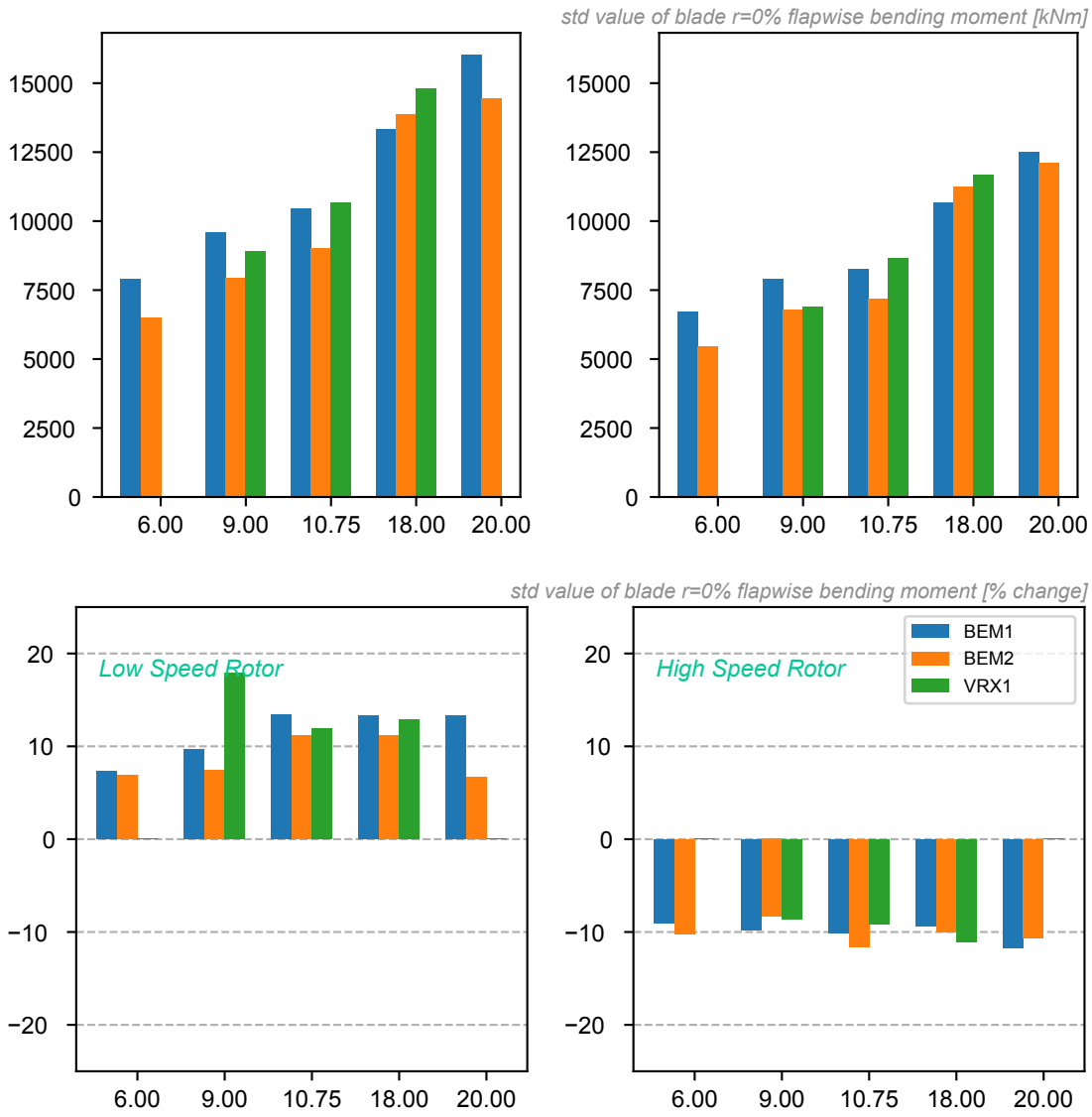

Figure 68: Absolute and Relative effect of rotational speed on blade flapwise bending moment at r=0% for DLC1.3

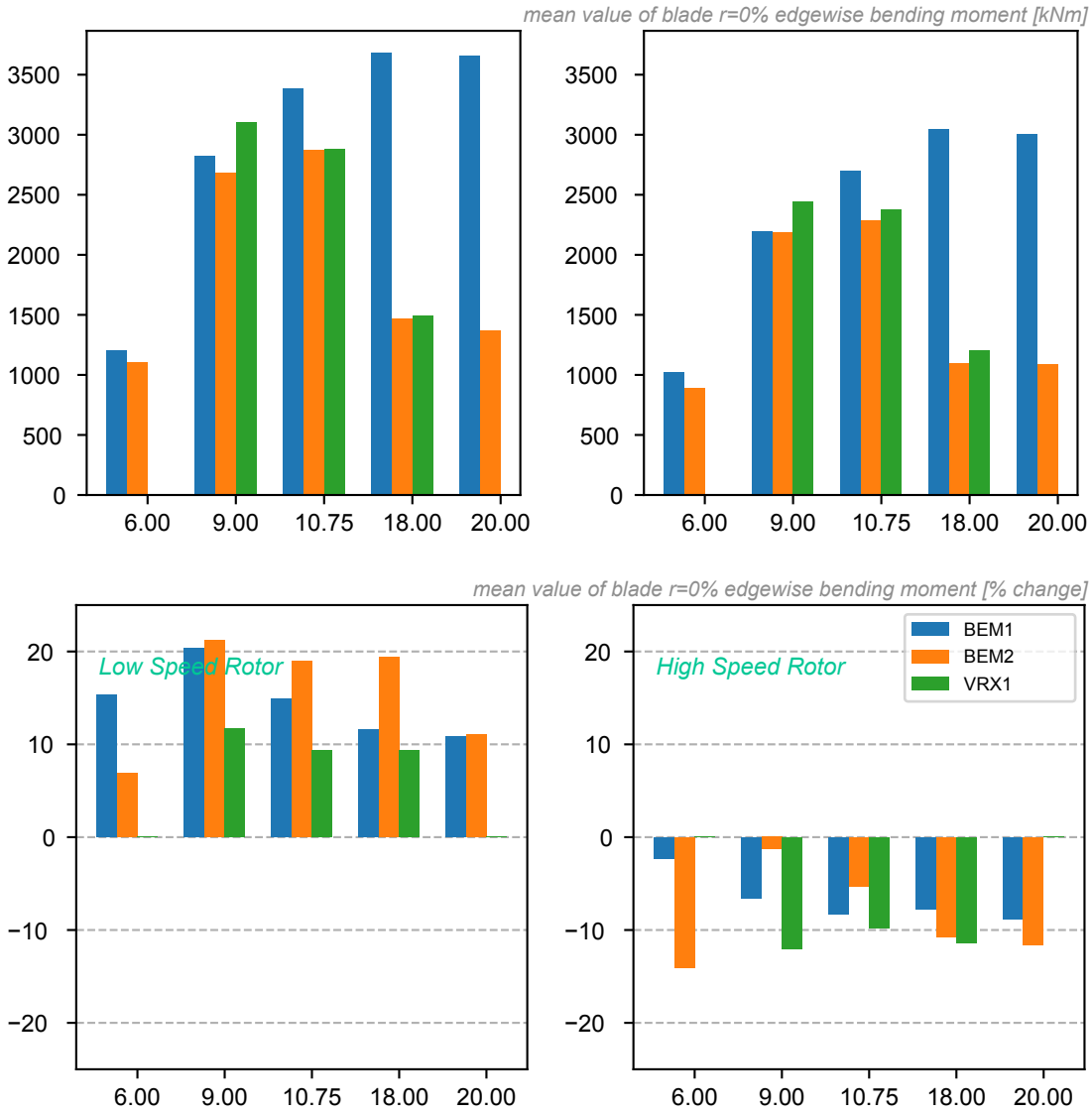

Figure 69: Absolute and Relative effect of rotational speed on the mean value of the blade r=0% edgewise bending moment for DLC1.2

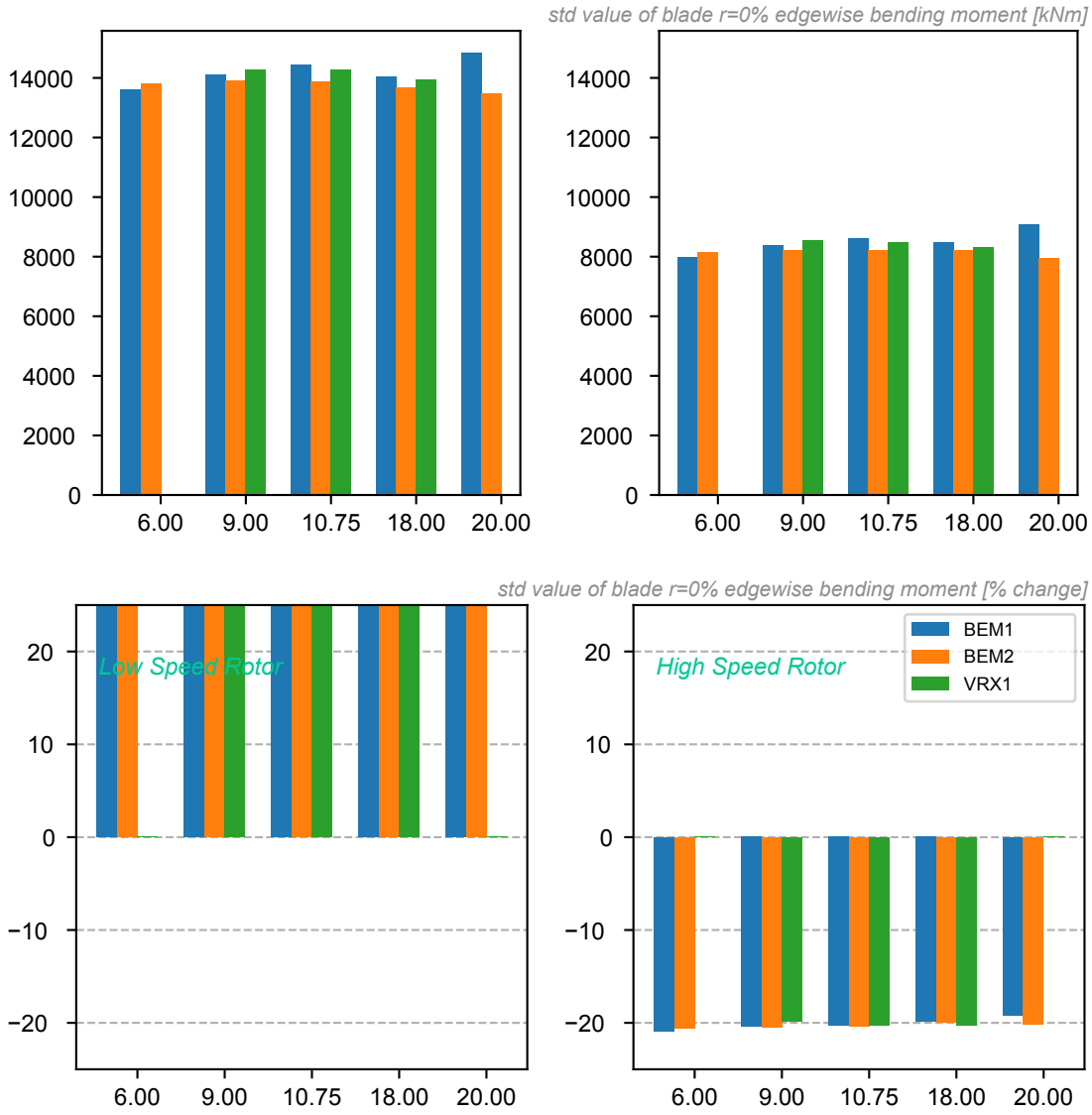

Figure 70: Absolute and Relative effect of rotational speed on blade edgewise bending moment at r=0% for DLC1.2

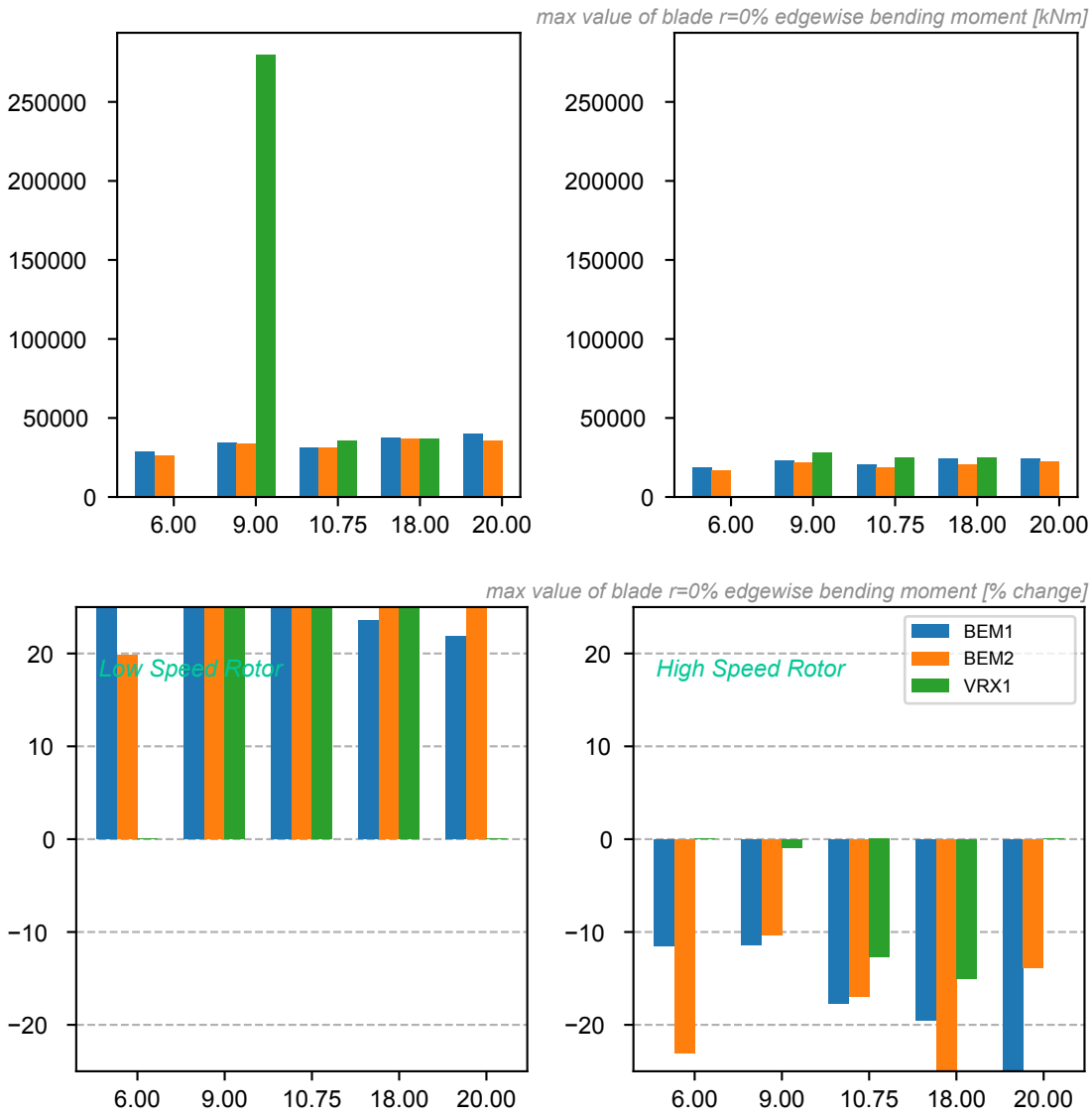

Figure 71: Absolute and Relative effect of rotational speed on the max value of the blade edgewise bending moment at r=0% for DLC1.3

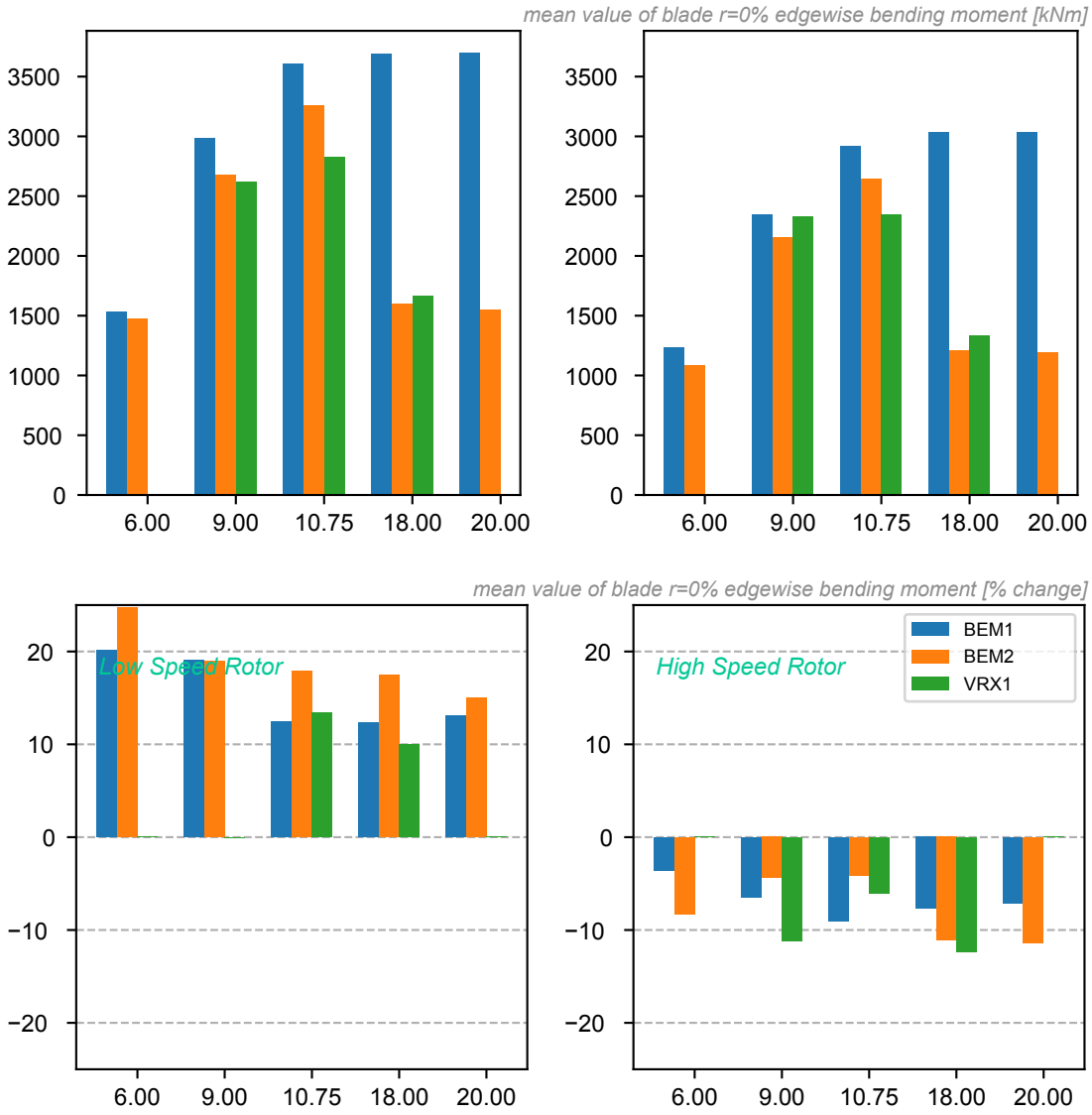

Figure 72: Absolute and Relative effect of rotational speed on the mean value of the blade edgewise bending moment at r=0% for DLC1.3

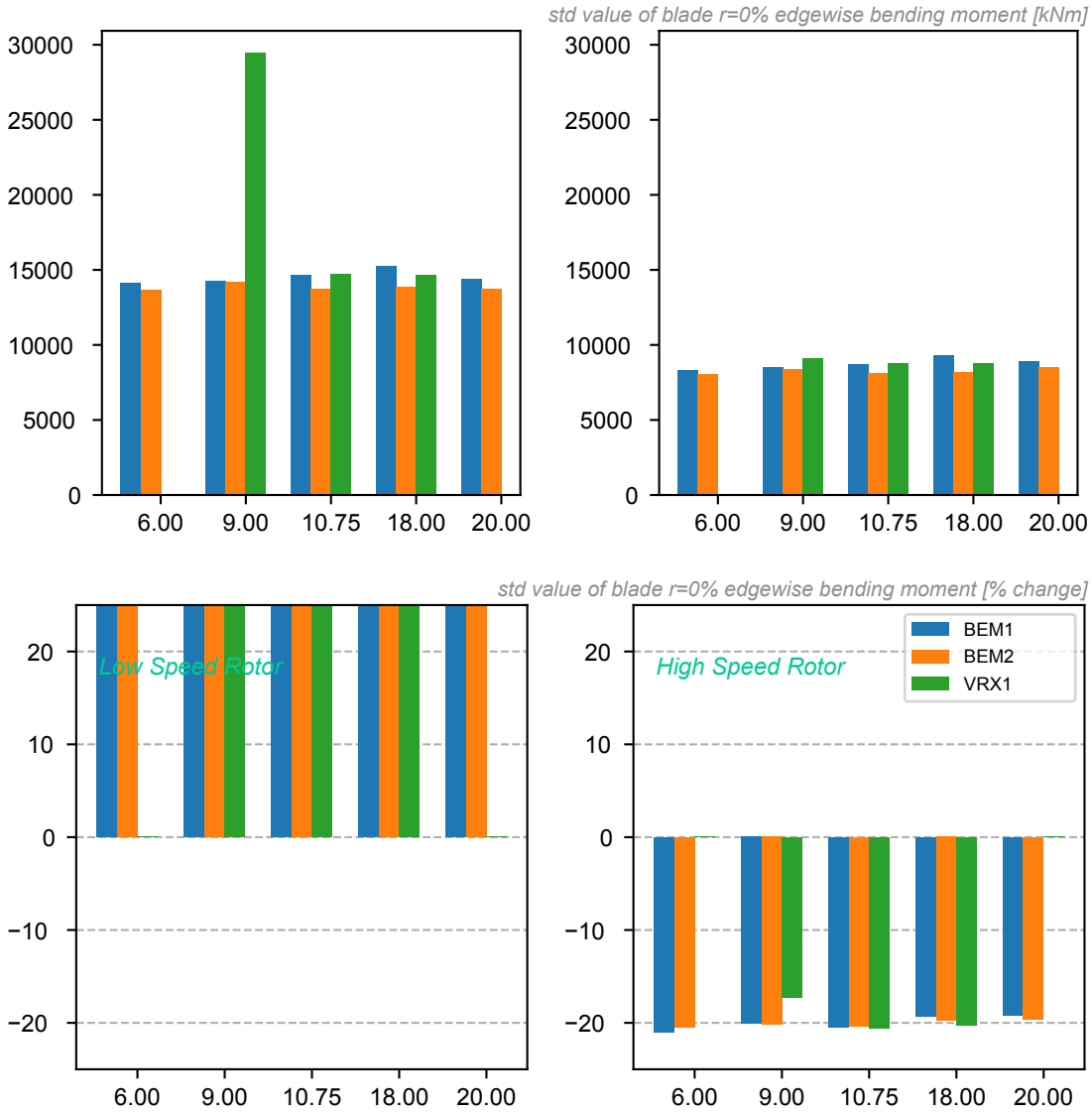

Figure 73: Absolute and Relative effect of rotational speed on blade edgewise bending moment at r=0% for DLC1.3

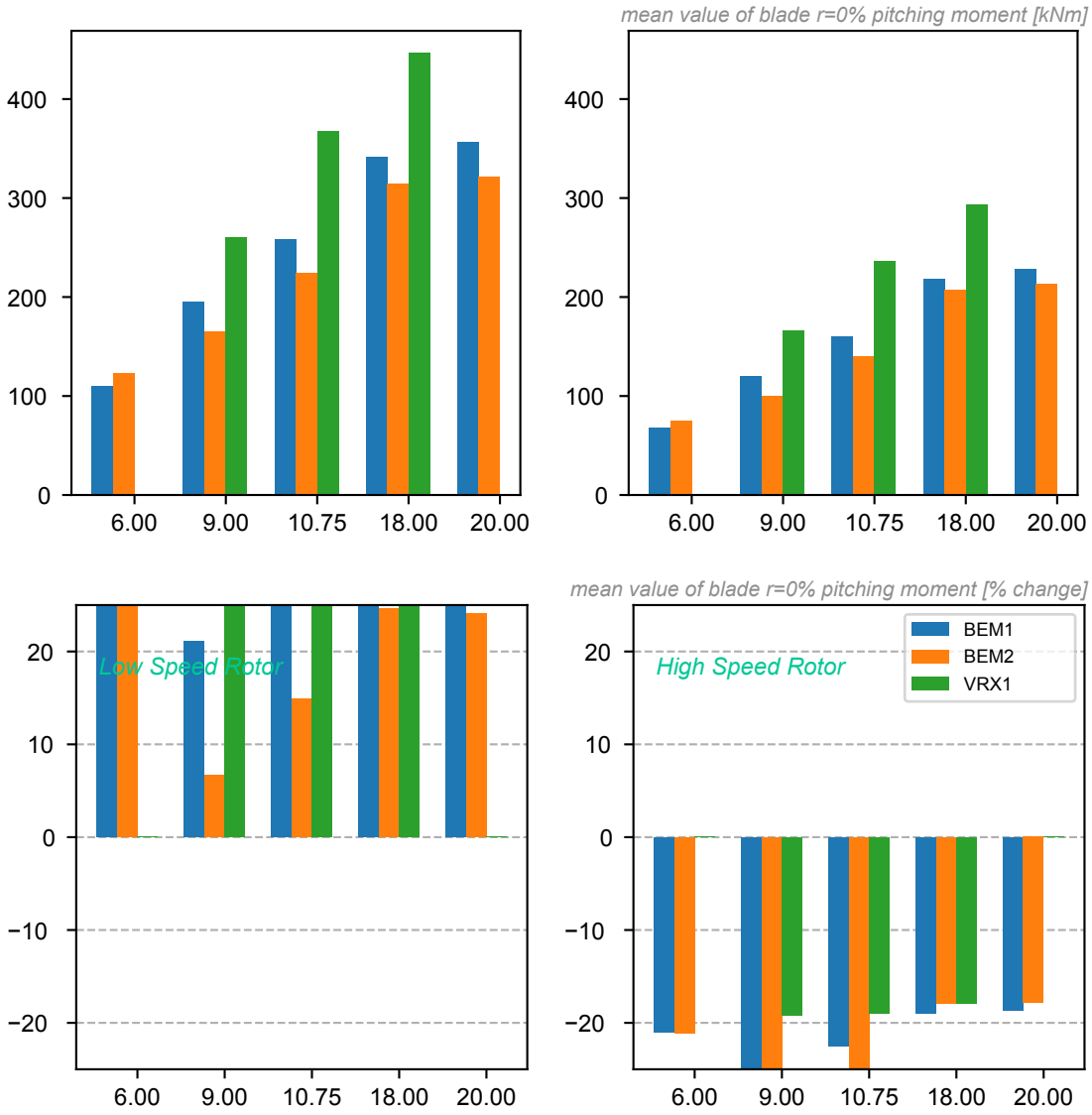

Figure 74: Absolute and Relative effect of rotational speed on the mean value of the blade r=0% pitching moment for DLC1.2

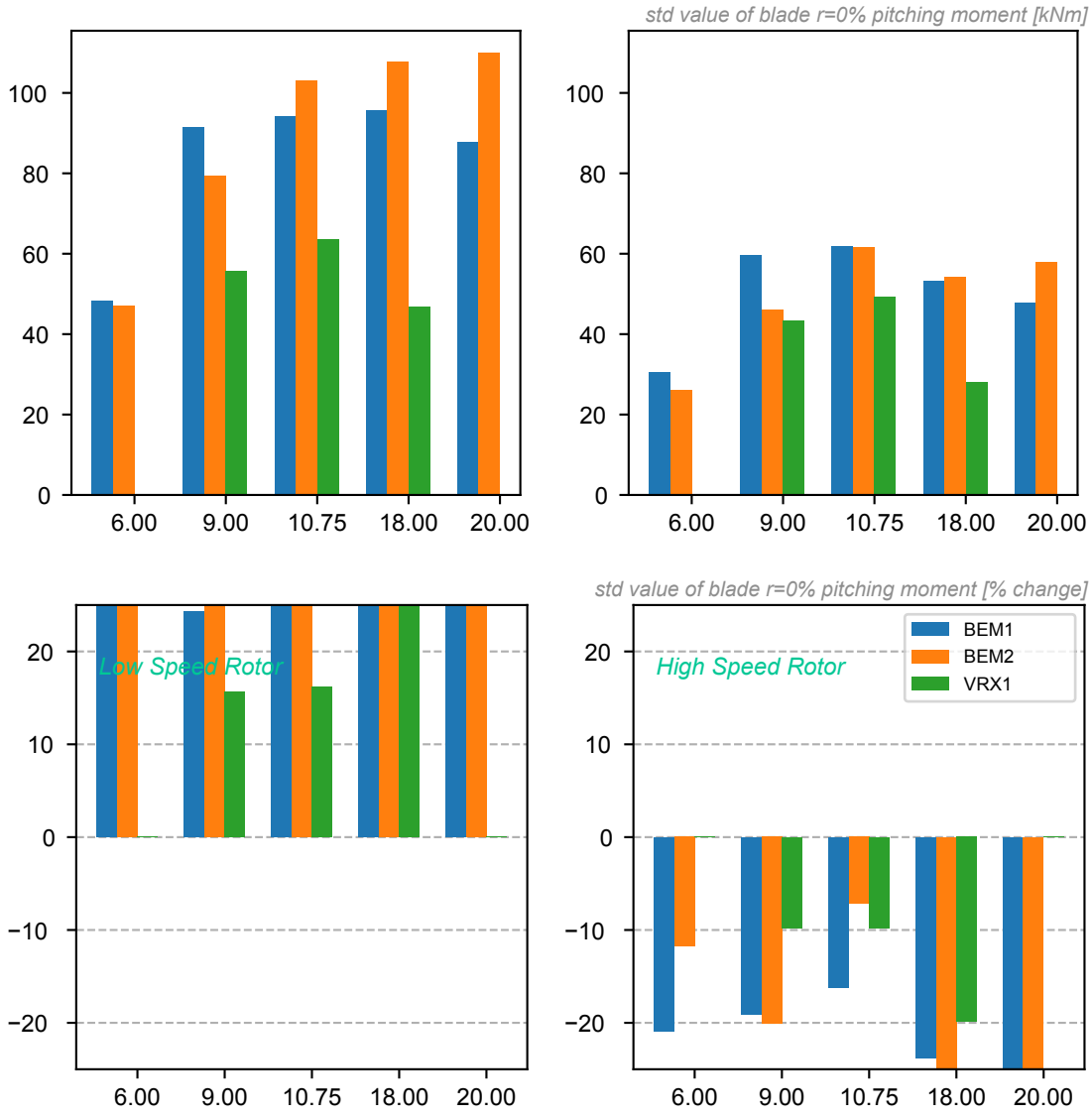

Figure 75: Absolute and Relative effect of rotational speed on blade pitching moment at r=0% for DLC1.2

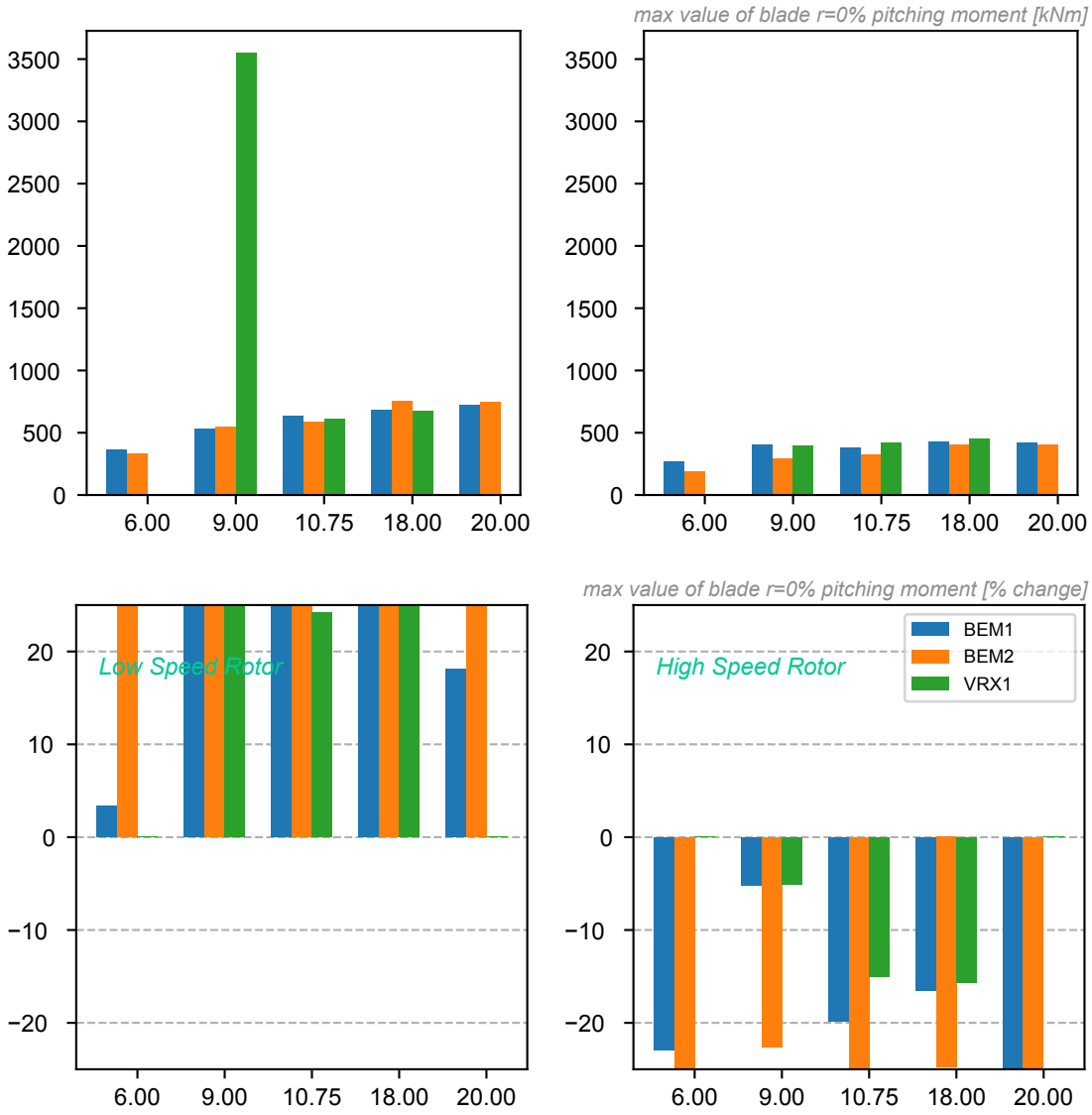

Figure 76: Absolute and Relative effect of rotational speed on the max value of the blade pitching moment at r=0% for DLC1.3

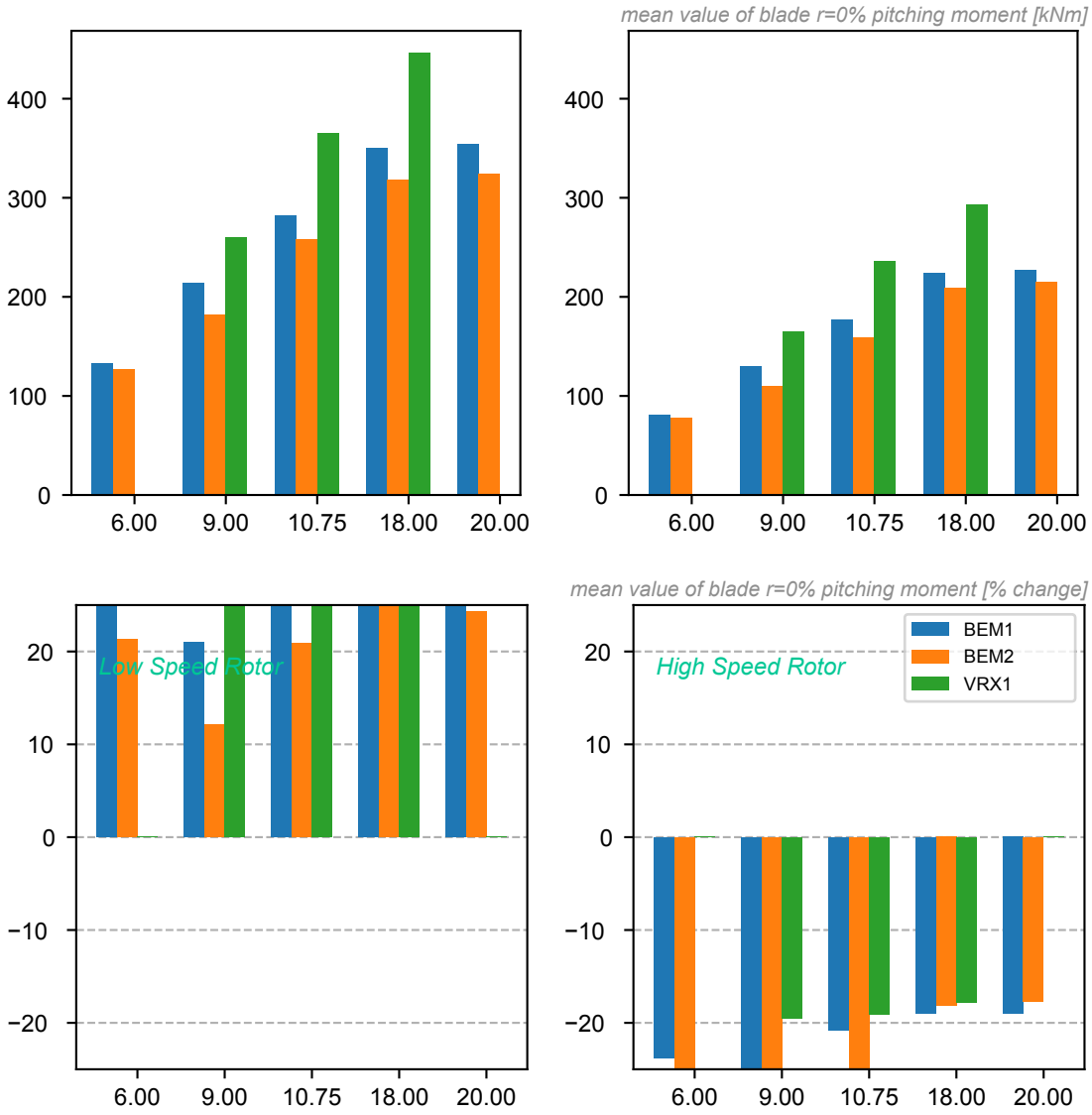

Figure 77: Absolute and Relative effect of rotational speed on the mean value of the blade pitching moment at r=0% for DLC1.3

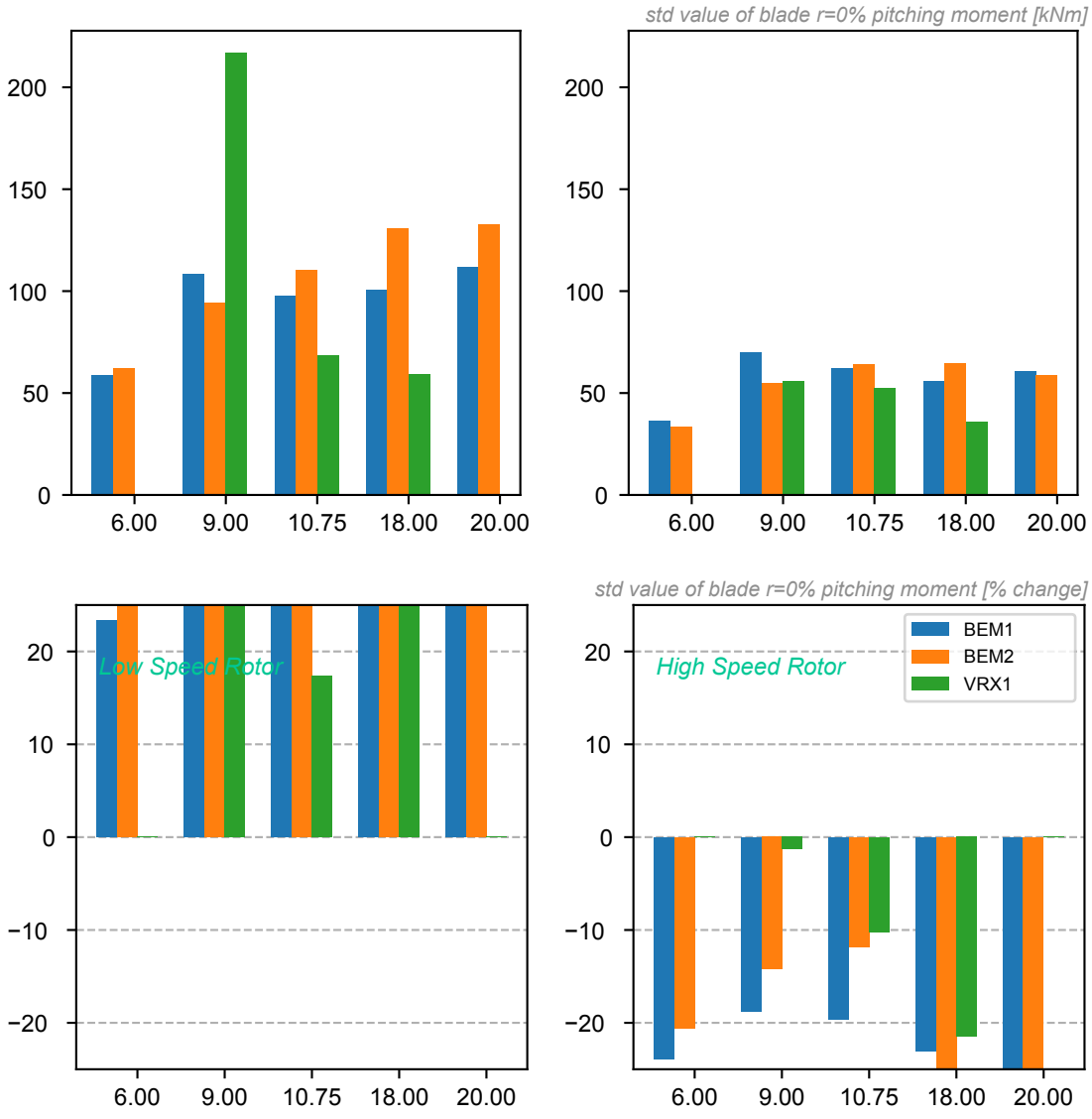

Figure 78: Absolute and Relative effect of rotational speed on blade r=0% pitching moment for DLC1.3

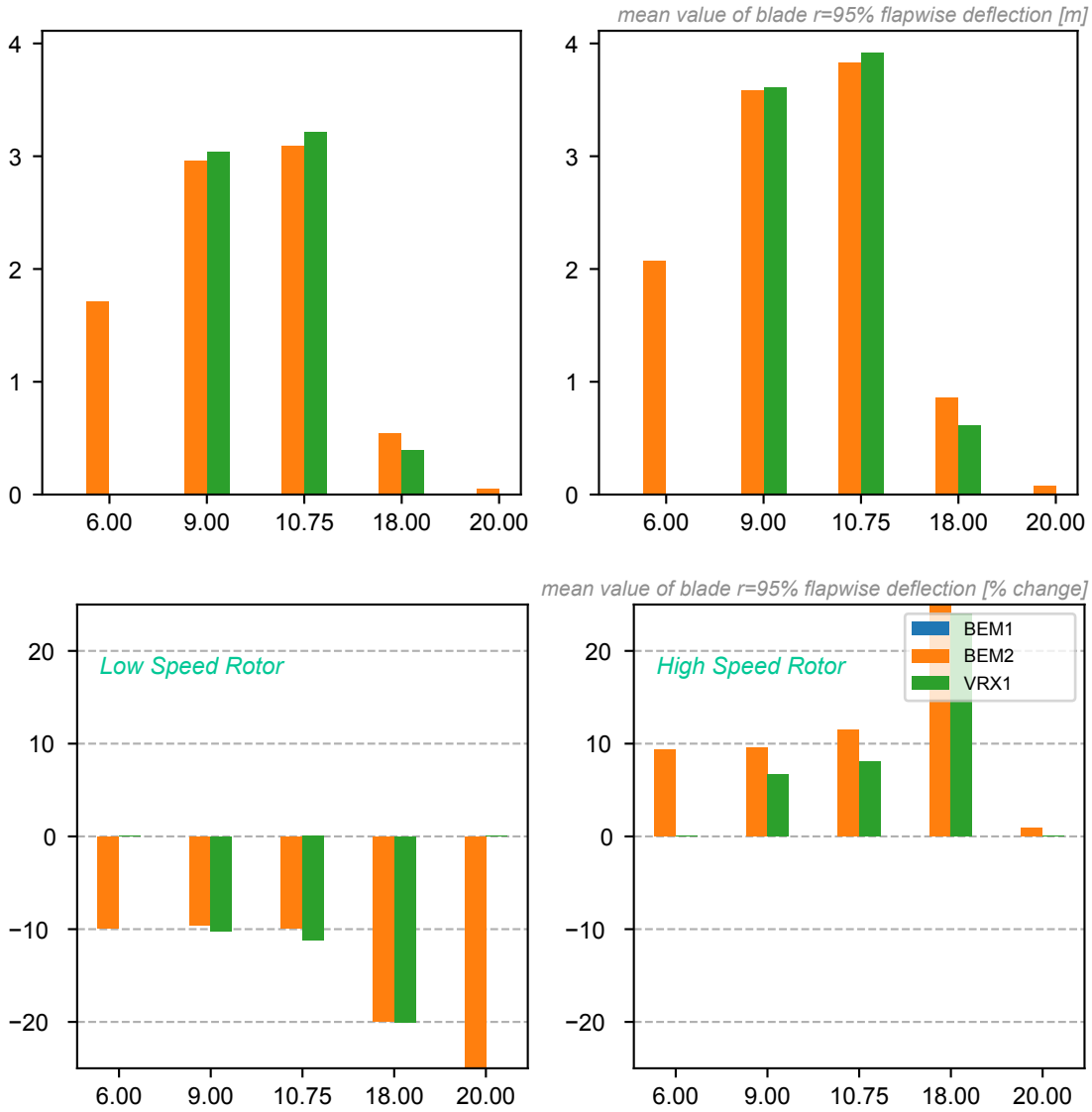

Figure 79: Absolute and Relative effect of rotational speed on the mean value of the blade r=95% flapwise deflection at r=95% for DLC1.2

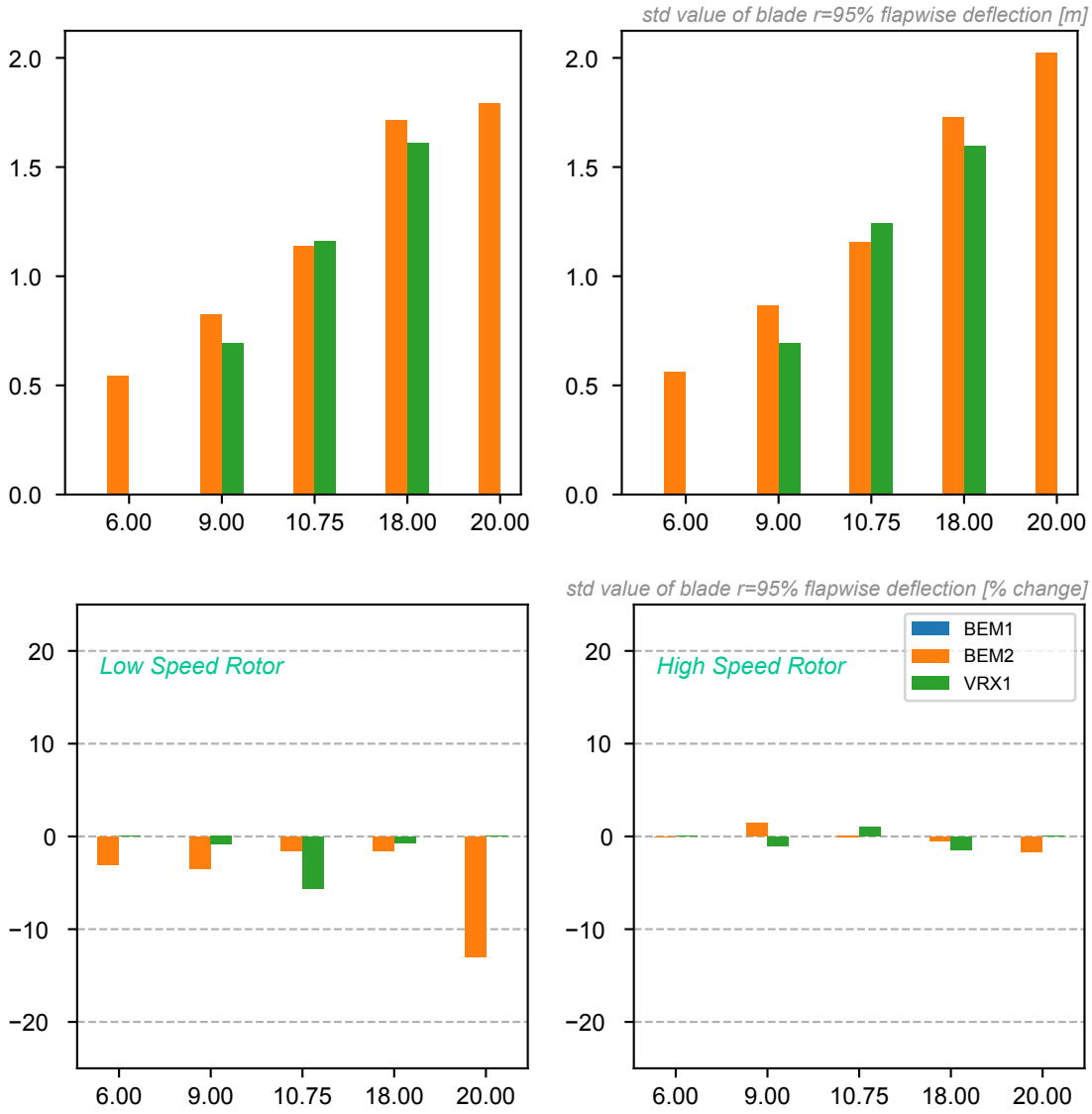

Figure 80: Absolute and Relative effect of rotational speed on blade flapwise deflection at r=95% for DLC1.2

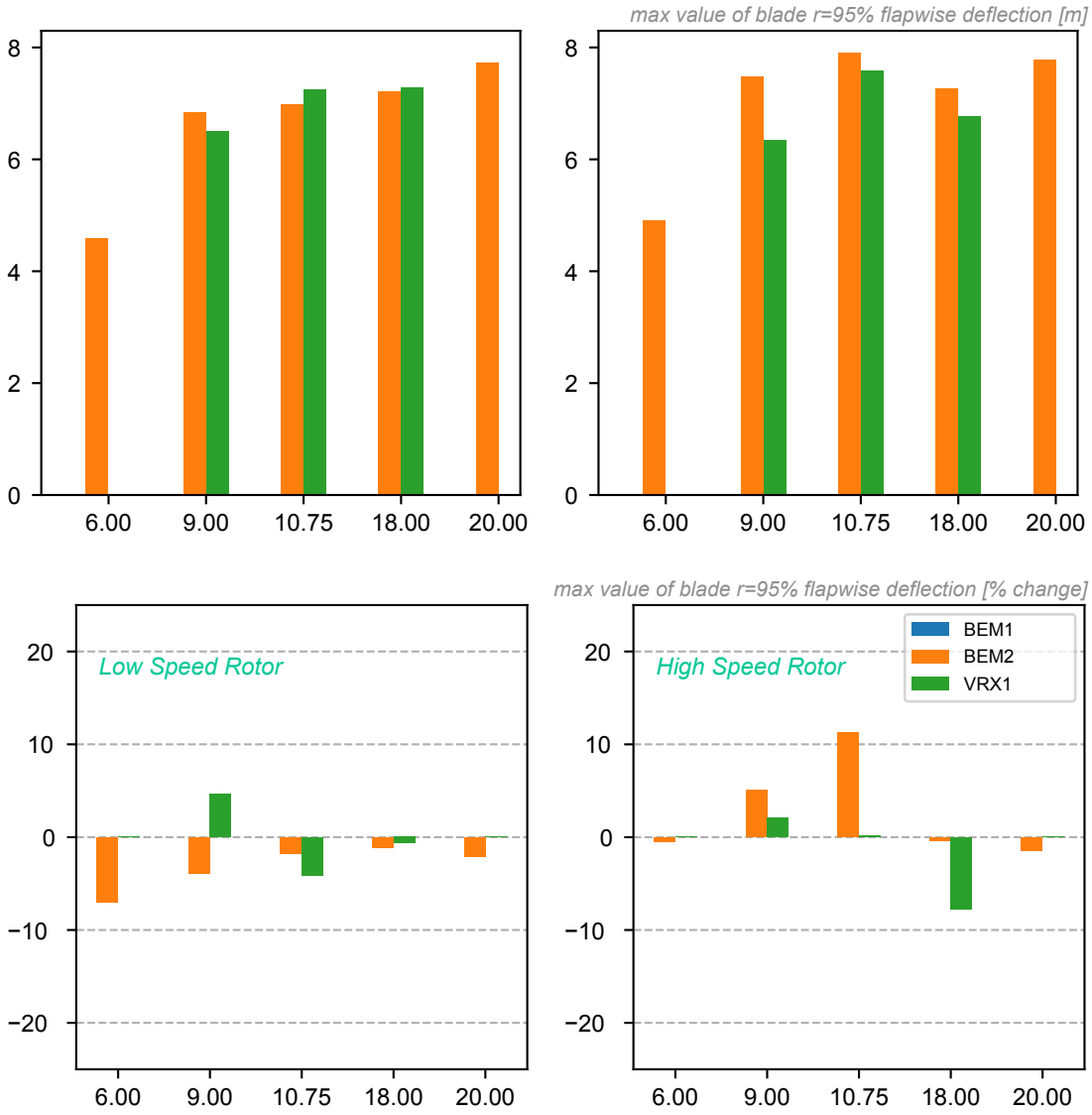

Figure 81: Absolute and Relative effect of rotational speed on the max value of the blade flapwise deflection at r=95% for DLC1.3

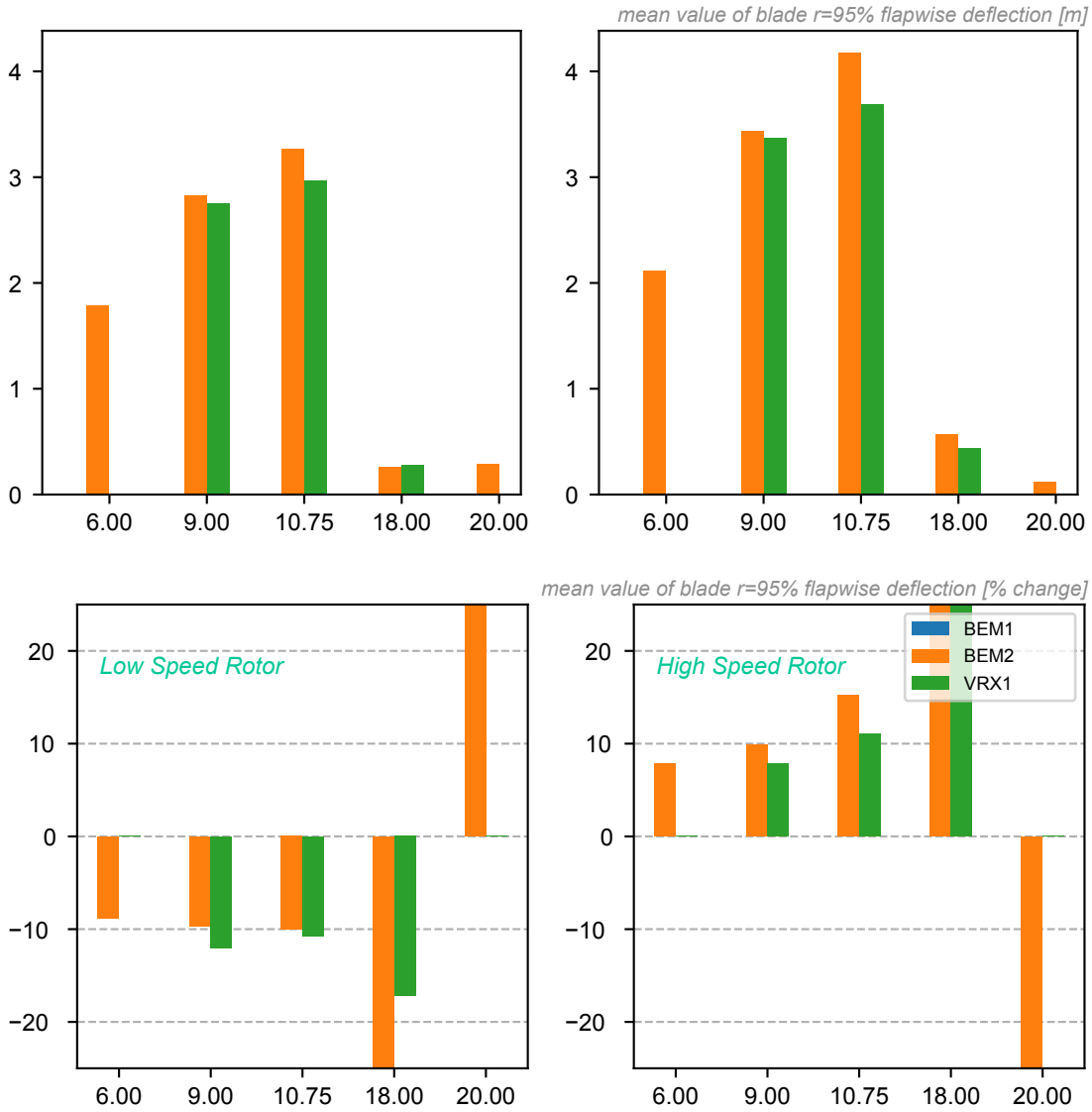

Figure 82: Absolute and Relative effect of rotational speed on the mean value of the blade flapwise deflection at r=95% for DLC1.3

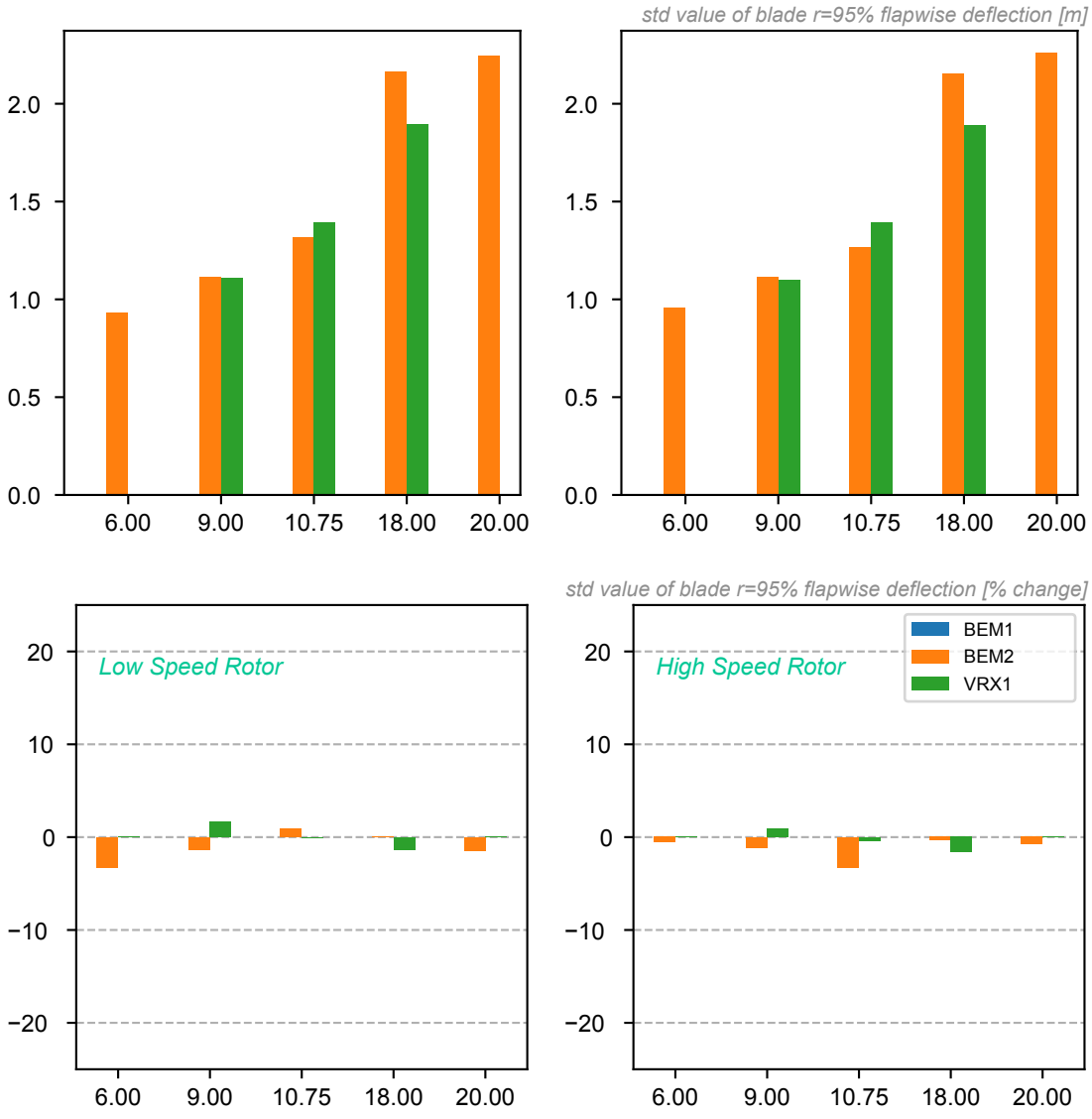

Figure 83: Absolute and Relative effect of rotational speed on blade r=95% flapwise deflection for DLC1.3

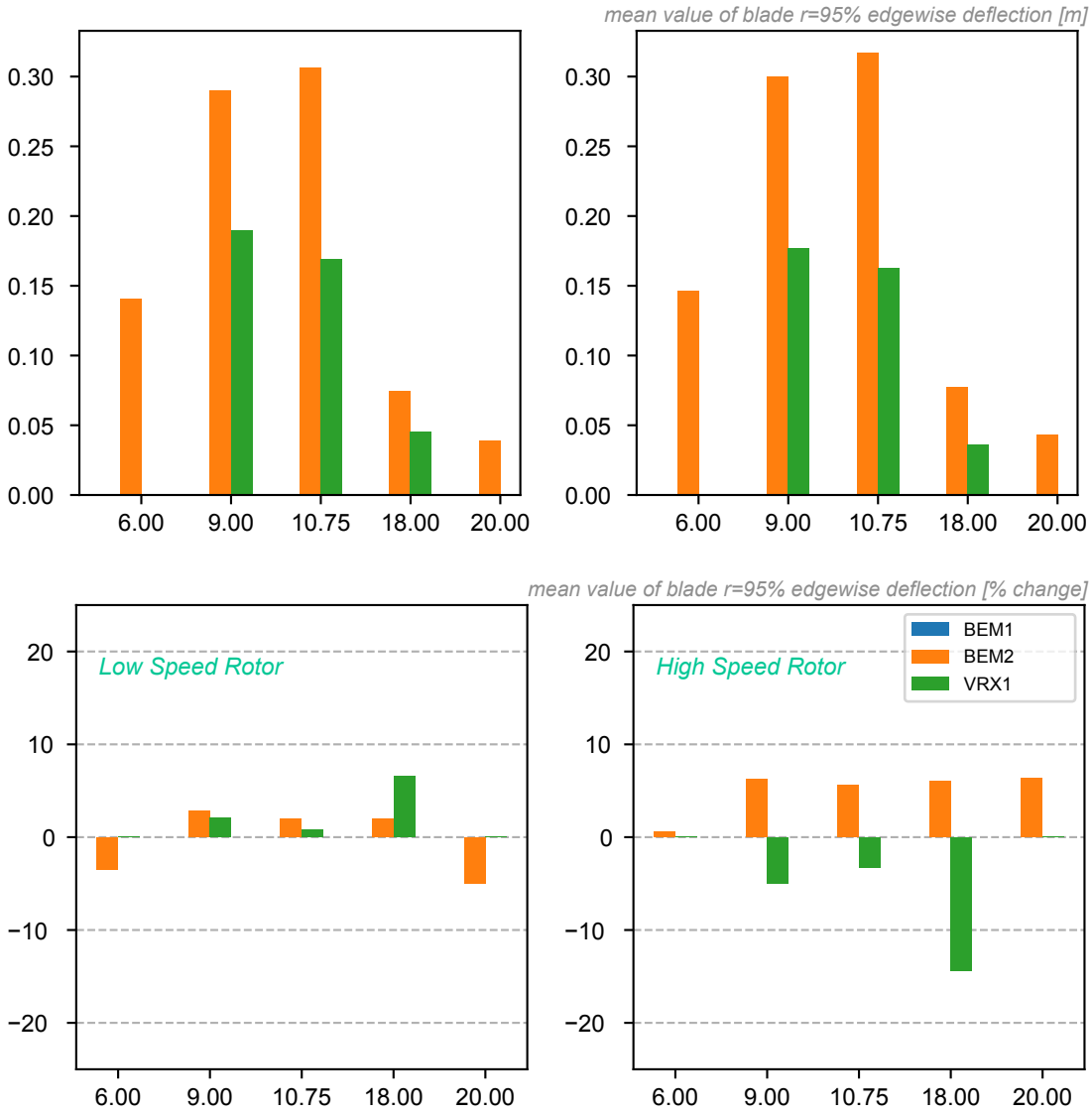

Figure 84: Absolute and Relative effect of rotational speed on the mean value of the blade edgewise deflection at r=95% for DLC1.2

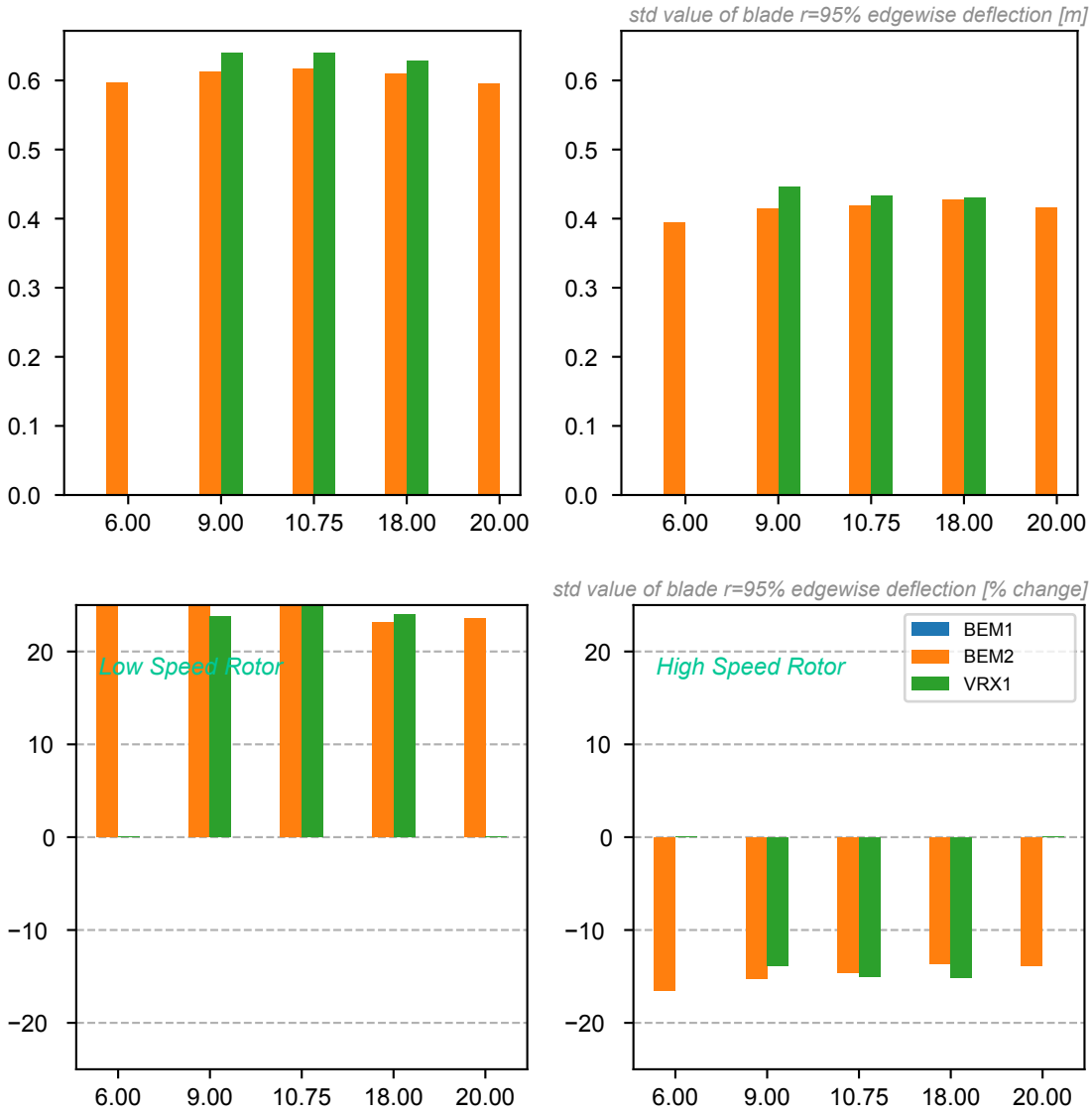

Figure 85: Absolute and Relative effect of rotational speed on blade edgewise deflection at r=95% for DLC1.2

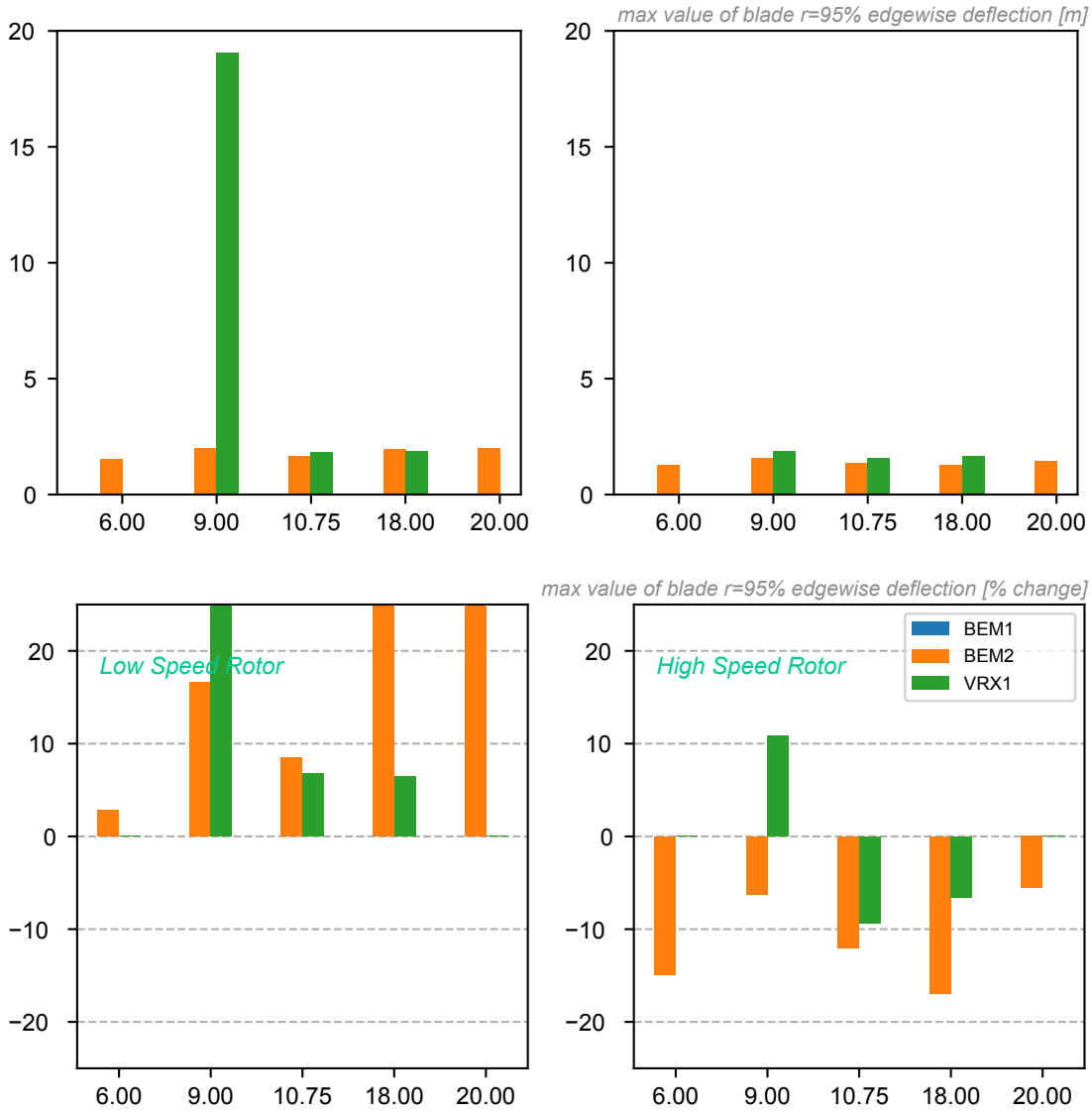

Figure 86: Absolute and Relative effect of rotational speed on on the max value of the blade edgewise deflection at r=95% for DLC1.3

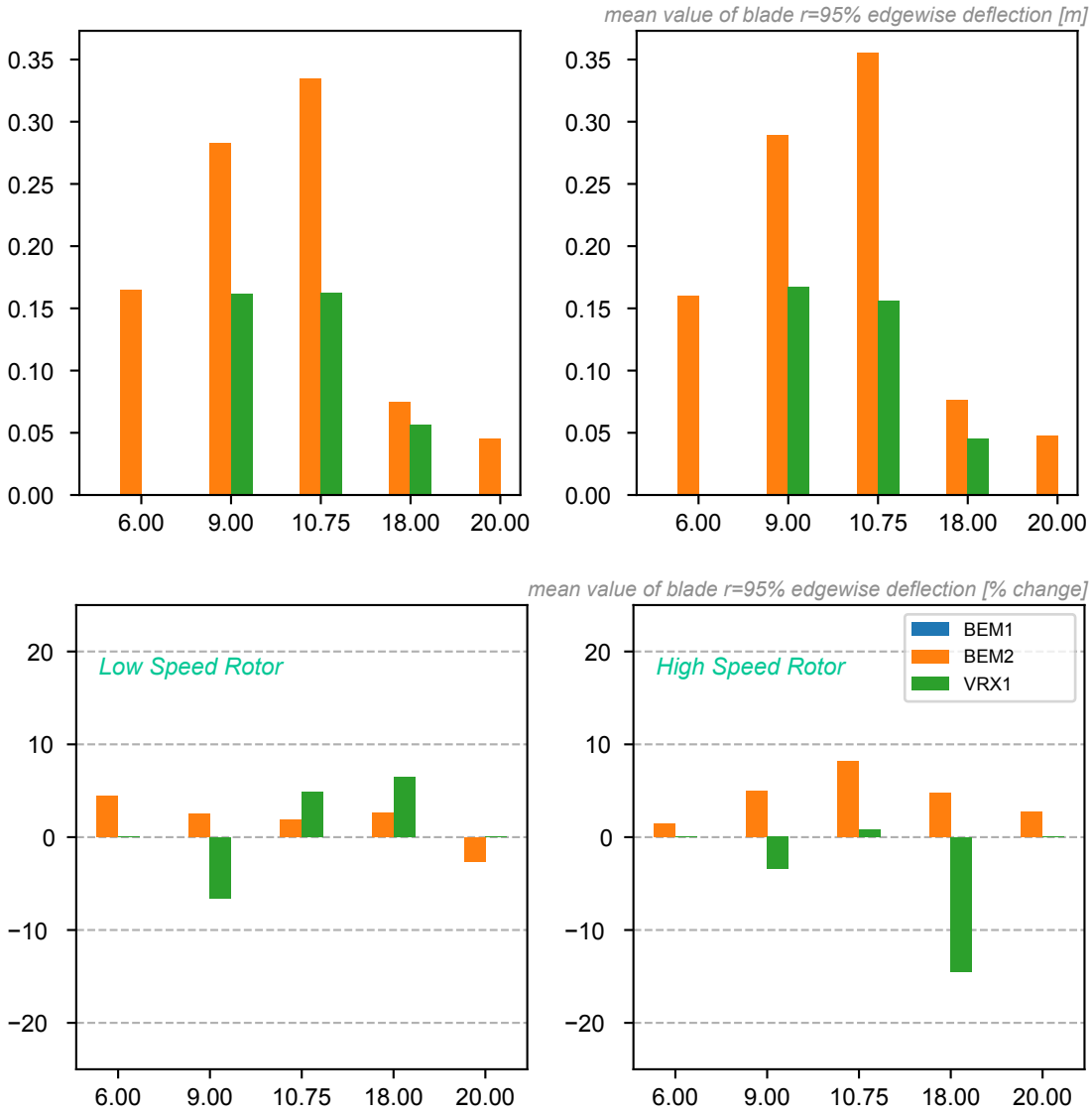

Figure 87: Absolute and Relative effect of rotational speed on the mean value of the blade edgewise deflection at r =95% for DLC1.3

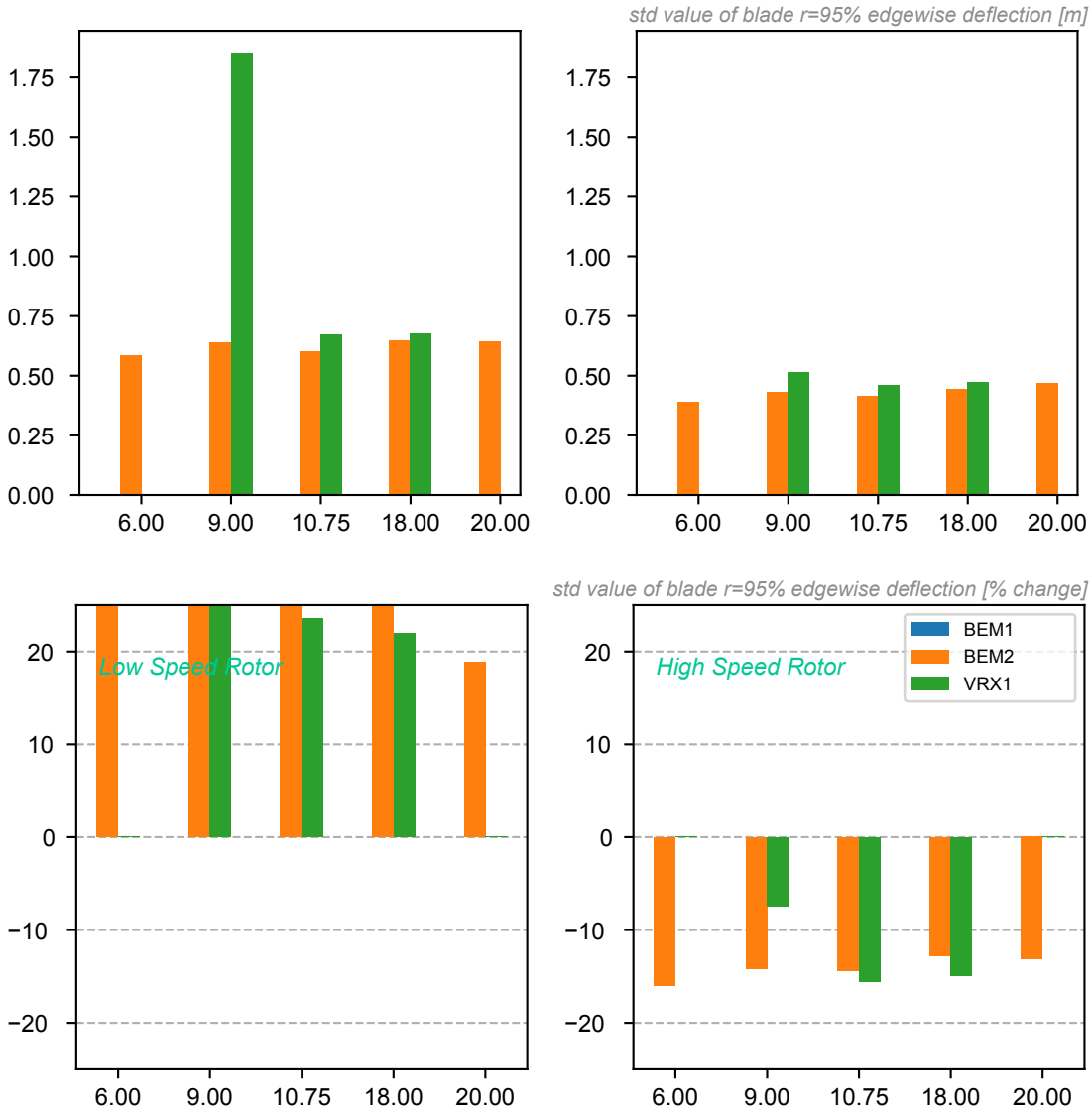

Figure 88: Absolute and Relative effect of rotational speed on blade edgewise deflection at r=95% for DLC1.3

5 Summary and Conclusions

A study of the effect of the rotating speed on the performanc eand loads of the AVATAR rotor wad performed. Two different variations with $\pm 10\,\%$ difference in TSR were examined and compared to the reference design.

A limited set of calculations was performed for the three rotors, with performance, stability and simplified turbulent wind simulations.

- The overall performance of the three rotors is quite similar. This is not unexpected as the design space with respect to the TSR is quite “flat” and similar levels of performance can be achieved for a broad range of values. This is more pronounced in the case of LIR (Low Induction Rotor) rotors, where the sections are not loaded to their maximum anyway.
- Stability is not seriously affected, as long as the design is performed with the proper limitations for each rotating speed
- The main effect of rotating speed on *mean* loads seems to be on
  1) The torque on the shaft, which obviously has a linear variation with the rotating speed, as long as we try to ensure a similar power curve.
  2) The edgewise loading, as the two designs differ considerably in weight and stiffness, with the high-speed design displaying substantially lower values of loads.
- The variation of the loads (as expressed through the standard deviation) seems to decrease with increasing rotating speed for most load cases.

For the proper evaluation of the results we should consider certain limitations of the applied methodology, namely, that

- The results in the unsteady simulations are sensitive to the controller modelling and calibration. As there has been no effort to properly tune the controller either with respect to each of the different codes or for the dynamic response of the specific different rotors, it is always possible that part of the recorded effect can be alleviated with the proper choice of control parameters.
- The structural properties are estimated based on scaling and simplifying assumptions, and are not based on a real design of the blades. It is therefore possible that there are other (possibly better) ways to design the low- and high- speed versions of the rotor. Nevertheless, as the intent of this study was to isolate the effect of speed *only* and not compare optimum high- and low- speed rotors (which might differ in many other ways), this approach remains useful.

References

[1] Bak, C., Zahle, F., Bitsche, R., Kim, T., Yde, A., Henriksen, L. C., Hansen, M. H., Blasques, J. P. A. A., Gaunaa, M., and Natarajan, A. “The DTU 10-MW reference wind turbine”. In: *Danish Wind Power Research 2013*. 2013.

[2] Stettner, M., Ruiz, A. I., Madsen, H. A., Verelst, D. R., Croce, A., Sartori, L., Lunghini, M. S., Reijerkerk, M., and Kooijman, H.-J. *Comparison of the INNWIND and AVATAR Research Wind Turbines*. WP1 Report Deliverable D1.3. AVATAR Project, Apr. 2015.

[3] Kim, T., Hansen, A. M., and Branner, K. “Development of an anisotropic beam finite element for composite wind turbine blades in multibody system”. In: *Renewable Energy* 59 (2013), p. 172.

[4] Larsen, T. J., Madsen, H. A., Larsen, G. C., and Hansen, K. S. “Validation of the dynamic wake meander model for loads and power production in the Egmond aan Zee wind farm”. In: *Wind Energy* 16.4 (2013), pp. 605–624.

[5] Madsen, H. A., Riziotis, V., Zahle, F., Hansen, M. O. L., Snel, H., Grasso, F., Larsen, T. J., Politis, E., and Rasmussen, F. “Blade element momentum modeling of inflow with shear in comparison with advanced model results”. In: *Wind Energy* 15 (Jan. 2012), pp. 63–81.

[6] Hansen, M. H., Gaunaa, M., and Madsen, H. A. *A Beddoes-Leishman type dynamic stall model in state-space and indicial formulations*. Risø-R-1354. Roskilde, Denmark, 2004.

[7] Leishman, J. and Beddoes, T. “A generalized method for unsteady airfol behaviour and dynamic stall using the indicial method”. In: *42nd Annual Forum*. Washington D.C.: American Helicopter Society, June 1986.

[8] Theodorsen, T. “General theory of aerodynamic instability and mechanism of flutter”. In: *National Advisory Committee for Aeronautics – Reports* (1935).

[9] Madsen, H. A., Bak, C., Døssing, M., Mikkelsen, R., and Øye, S. “Validation and modification of the Blade Element Momentum theory based on comparisons with actuator disc simulations”. In: *Wind Energy* 13.4 (May 1, 2010), pp. 373–389.

[10] Glauert, H. *A General Theory of the Autogyro*. ARC R&M No.1111. ARC R&M, 1926.

[11] Chasapogiannis, P., González, A., Irisarri, A., Madsen, H. A., Larsen, T. J., Boorsma, K., Schwarz, M., Reijekerk, M., and Manolas, D. *Comparison of models with respect to Load analysis in extreme yaw of the INNWIND.EU and AVATAR RWT’s*. WP4 Report Deliverable D4.3. AVATAR Project, June 2016.

[12] Ramos-García, N., Sørensen, J. N., and Shen, W. Z. “A strong viscous–inviscid interaction model for rotating airfoils”. In: *Wind Energy* 17.12 (2014), pp. 1957–1984.

[13] Ramos-García, N., Sørensen, J. N., and Shen, W. Z. “Validation of a three-dimensional viscous–inviscid interactive solver for wind turbine rotors”. In: *Renewable Energy* 70 (2014), pp. 78–92.

[14] Mack, L. M. “Transition and Laminar Instability. Jet Propulsion Laboratory Pub”. In: *Pasadena, CA* (1977), pp. 77–15.

[15] Hansen, M. H. “Aeroelastic stability analysis of wind turbines using an eigenvalue approach”. In: *Wind Energy* 7.2 (2004), pp. 133–143.

[16] Hansen, M. H. “Aeroelastic properties of backward swept blades”. In: *49th AIAA Aerospace Sciences Meeting including the New Horizons Forum and Aerospace Exposition, Orlando, Florida*. 2011.

[17] Sønderby, I. and Hansen, M. H. “Open-loop frequency response analysis of a wind turbine using a high-order linear aeroelastic model”. In: *Wind Energy* 17.8 (2014), pp. 1147–1167.

[18] Tibaldi, C., Henriksen, L. C., Hansen, M. H., and Bak, C. “Wind turbine fatigue damage evaluation based on a linear model and a spectral method”. In: *Wind Energy* 19.7 (July 1, 2016), pp. 1289–1306.

[19] Manolas, D., Riziotis, V., and Voutsinas, S. “Assessment of 3D aerodynamic effects on the behaviour of floating wind turbines”. In: *The Science of Making Torque from Wind*. Oldenburg, Germany, 2012.

[20] Belessis, M., Chasapogiannis, P., and Voutsinas, S. “Free-wake modellng of rotor aerodynamics: recent developments and future perspectives”. In: *EWEC 2001*. Copenhagen, Denmark, July 2001.

[21] Heinz, J., Sørensen, N. N., Riziotis, V. A., Chasapogiannis, P., Schwarz, M., Gomez-Iradi, S., and Stettner, M. *Aerodynamics of Large Rotors*. WP4 Report Deliverable D4.5. AVATAR Project, Aug. 2016.

[22] Meng, F., Reijekerk, M., Manolas, D., Chasapogiannis, P., Madsen, H. A., Larsen, T. J., Salcedo, A., and Boorsma, K. *Comparison of models with respect to loads analysis in extreme shear and half wake of the INNWIND.EU and AVATAR RWTs*. WP4 Report Deliverable D4.4. AVATAR Project, June 2016.

[23] Riziotis, V. A., Voutsinas, S. G., Politis, E. S., and Chaviaropoulos, P. K. “Aeroelastic stability of wind turbines: the problem, the methods and the issues”. In: *WIND ENERGY* 7.4 (2004), pp. 373–392.

[24] Riziotis, V. A., Voutsinas, S. G., Politis, E. S., and Chaviaropoulos, P. K. “Assessment of passive instability suppression means on pitch-regulated wind turbines”. In: *Wind Energy* 11.2 (Mar. 2008), pp. 171–192.

[25] Riziotis, V. A. and Voutsinas, S. G. “GAST: A general aerodynamic and structural prediction tool for wind turbines”. In: *EWEC-CONFERENCE*. Dublin, Ireland, 1997, pp. 448–452.

[26] Chaviaropoulos, P. K. “Flap/lead–lag aeroelastic stability of wind turbine blades”. In: *Wind Energy* 4.4 (Oct. 1, 2001), pp. 183–200.

[27] Moriarty, P. J. and Hansen, A. C. *AeroDyn theory manual*. NREL/TP-500-36881. 1617 Cole Boulevard Golden, Colorado 80401-3393: National Renewable Energy Laboratory, Jan. 2005.

[28] Øye, S. “Unsteady wake effects caused by pitch–angle changes”. In: *IEA R&D WECS Joint Action on Aerodynamics of Wind Turbines, 1st Symposium*. 1986, pp. 58–79.

[29] Sieros, G. *Speed Effect Details*. Supporting Material Deliverable D4.11. AVATAR Project, May 2017.

[30] Stettner, M., Reijerkerk, M. J., Lünenschlo{\textbackslash}s s, A., Riziotis, V., Croce, A., Sartori, L., Riva, R., and Peeringa, J. M. “Stall-Induced Vibrations of the AVATAR Rotor Blade”. In: *Journal of Physics: Conference Series*. Vol. 753. IOP Publishing, 2016, p. 042019.

[31] Jamieson, P. *Innovation in Wind Turbine Design*. 1 edition. Chichester, West Sussex ; Hoboken, N.J: John Wiley & Sons, Sept. 7, 2011. 318 pp.

A Theoretical Background

Theoretical background from “Peter Jamieson, Innovation in Wind Turbine Design, A John Wiley & Sons, Ltd., Publication, ISBN 978-0-470-69981-2, 2011”

Jamieson, P. *Innovation in Wind Turbine Design*. 1 edition. Chichester, West Sussex ; Hoboken, N.J: John Wiley & Sons, Sept. 7, 2011. 318 pp.

We introduce the definitions of the TSR, of the blade section lift to drag ratio k and the radius fraction x according to A.1. Note that V is the ambient wind speed, ω the rotational speed, R the rotor radius, and B the number of rotor blades.

$$\lambda = \frac{\omega R}{V},\ k = \frac{C_L}{C_D},\ x = \frac{r}{R} \tag{A.1}$$

Assuming a (uniform on the rotor disc) induction factor a, the span-wise distribution of the circumferential induction a' can be expressed as a function of a, k, λ *and* x:

$$a' = \frac{\sqrt{(k\lambda x)^2 + 2k\lambda x - 4ak\left[\lambda x - k\left(1-a\right) + 1\right]} - (k\lambda x + 1)}{2k\lambda x} \tag{A.2}$$

Using Prandtl’s tip factor

$$F = \frac{2}{\pi}\arccos\left[e^{-\frac{(1-x)B\lambda}{2(1-a)}}\right] \tag{A.3}$$

And introducing the non-dimensional lift distribution $\Lambda(\lambda, x)$ where $c(\lambda, x)$ is the chord distribution,

$$\Lambda(\lambda, x) = \frac{c(\lambda, x)C_L}{R} \tag{A.4}$$

it can be shown that $\Lambda(\lambda, x)$ which for selected values of λ and B corresponds to the axial induction value a, is given by Eq. A.5

$$\Lambda(\lambda, x) = \frac{8\pi a\left(1-a\right)}{B\lambda\left(1+a'\right)\sqrt{\left(1-a\right)^2 + \lambda^2 x^2\left(1+a'\right)^2}}\frac{F}{1+\frac{(1-a)}{k\lambda x(1+a')}} \tag{A.5}$$

For given design C_L value(s) Eq. A.5 can be used for defining the blade chord distribution which yields a given axial induction factor, while the blade twist distribution will derive from the flow angle φ distribution, as given from the classical BEM velocity triangle,

$$\tan\varphi = \frac{\left(1-a\right)}{\lambda x\left(1+a'\right)} \tag{A.6}$$

by subtracting the design angle of attack (corresponding to the design C_L value(s)).

The C_P (Power Coefficient), C_T (Rotor Thrust Coefficient) and C_T at arbitrary radial distance r are given by Eq. A.7-A.9

$$C_P(\lambda) = \int_0^1 \frac{8a(1-a)F\left[k(1-a) - \lambda x(1+a')\right]\lambda x^2}{\left[(1-a) + k\lambda x(1+a')\right]} dx \tag{A.7}$$

$$C_T = \int_0^1 8a(1-a)Fx dx \tag{A.8}$$

$$C_M(r) = \frac{8a(1-a)}{B}\int_x^1 \frac{F(y)}{\left[\frac{(1-a)}{k} + \lambda y(1+a')\right]}\left[\lambda y + \frac{(1-a)}{k}\right](y-x)\,dy \tag{A.9}$$

where the above coefficients are defined as non-dimensional representations of the Power (P), Thrust (T) and Bending Moment $M(r)$ through Eq. A.10-A.12

$$P = \frac{1}{2}\rho\pi R^2 V^3 C_P \tag{A.10}$$

$$T = \frac{1}{2}\rho\pi R^2 V^2 C_T \tag{A.11}$$

$$M(r) = \frac{1}{2}\rho\pi R^3 V^2 C_M(r) \tag{A.12}$$

B Controller Parameters

Controller Characteritics

No	INNWIND	AVATAR	High Speed (D4.11)	Low Speed (D4.11)	High Speed (D4.11)	Low Speed (D4.11)	
General					AVATAR Based	AVATAR Based	
1	10638,3	10638,3	10638,3	10638,3	10638,3	10638,3	Rated power [kW]
2	0,6280	0,6280	0,6911	0,5760	0,6911	0,5760	Minimum rotor speed [rad/s]
3	1,0050	1,0050	1,1058	0,9048	1,1058	0,9048	Rated rotor speed [rad/s]
4	1,56E+07	1,56E+07	1,41E+07	1,73E+07	1,41E+07	1,73E+07	Maximum allowable generator torque [Nm]
5	0,00	0,00	0,00	0,00	0,00	0,00	Minimum pitch angle, PitchMin [deg] – if [PitchMin] >90, then a table of <wsp,PitchMin> is read from a file named 'wptable.n', where n=int(PitchMin)
6	90,00	90,00	90,00	90,00	90,00	90,00	Maximum pitch angle [deg]
7	10,00	10,00	10,00	10,00	10,00	10,00	Maximum pitch velocity operation [deg/s]
8	0,20	0,40	0,20	0,20	0,40	0,40	Frequency of generator speed filter [Hz]
9	0,70	0,70	0,70	0,70	0,70	0,70	Damping ratio of speed filter [-]
10	3,33	1,64	3,33	3,33	1,64	1,64	Frequency of free-free DT torsion mode [Hz]
Partial Load Control Parameters							
11	1,000E+07	9,650E+06	8,990E+06	1,599E+07	8,990E+06	1,599E+07	Optimal Cp tracking K factor [Nm/(rad/s)^2]
12	6,830E+07	1,050E+08	6,830E+07	6,830E+07	1,050E+08	1,050E+08	Proportional gain of torque controller [Nm/(rad/s)]
13	1,530E+07	1,530E+07	1,530E+07	1,530E+07	1,530E+07	1,530E+07	Integral gain of torque controller [Nm/rad]
14	0,000E+00	0,000E+00	0,000E+00	0,000E+00	0,000E+00	0,000E+00	Differential gain of torque controller [Nm/(rad/s^2)]
Full Load Control Parameters							

								1	Generator control switch [1=constant power, 2=constant torque]
15	2	1	2	2	1				
								0,762	Proportional gain of pitch controller [rad/(rad/s)]
16	0,524	0,762	0,524	0,524	0,762				
								0,224	Integral gain of pitch controller [rad/rad]
17	0,141	0,224	0,141	0,141	0,224				
								0,000	Differential gain of pitch controller [rad/(rad/s^2)]
18	0,000	0,000	0,000	0,000	0,000				
								4,000E-09	Proportional power error gain [rad/W]
19	4,000E-09	4,000E-09	4,000E-09	4,000E-09	4,000E-09				
								4,000E-09	Integral power error gain [rad/(Ws)]
20	4,000E-09	4,000E-09	4,000E-09	4,000E-09	4,000E-09				
								10,68	Coefficient of linear term in aerodynamic gain scheduling, KK1 [deg]
21	198,00	10,68	198,00	198,00	10,68				
								601,25	Coefficient of quadratic term in aerodynamic gain scheduling, KK2 [deg^2], (if zero, KK1 = pitch angle at double gain)
22	693,00	601,25	693,00	693,00	601,25				
								1,30	Relative speed for double nonlinear gain [-]
23	1,30	1,30	1,30	1,30	1,30				
Cut-in Control Parameters									
24	0	0	0	0	0			0	Cut-in time [s]
								1	Time delay for soft start of torque [1/1P]
25	4	1	4	4	1				
Cut-out Control Parameters									
26	0,00	0,00	0,00	0,00	0,00			0,00	Cut-out time [s]
								5,00	Time constant for linear torque cut-out [s]
27	5,00	5,00	5,00	5,00	5,00				
								1,00	Stop type [1=normal, 2=emergency]
28	1,00	1,00	1,00	1,00	1,00				
								1,00	Time delay for pitch stop after shut-down signal [s]
29	1,00	1,00	1,00	1,00	1,00				

								Maximum pitch velocity during initial period of stop	
30	20,00	3,00	20,00	20,00	3,00	3,00	[deg/s]		
							Time period of initial pitch		
31	1,00	3,00	1,00	1,00	3,00	3,00	stop phase [s]		
							Maximum pitch velocity during final phase of stop		
32	10,00	4,00	10,00	10,00	4,00	4,00	[deg/s]		
Expert Control Parameters									
							Lower angle above lowest minimum pitch angle for		
33	0,50	2,00	0,50	0,50	2,00	2,00	switch [deg]		
							Upper angle above lowest minimum pitch angle for		
							switch [deg], if equal then		
34	0,50	2,00	0,50	0,50	2,00	2,00	hard switch		
							Ratio between filtered speed and reference speed for fully		
35	95,00	95,00	95,00	95,00	95,00	95,00	open torque limits [%]		
							Time constant of 1st order filter on wind speed used for		
36	5,00	2,00	5,00	5,00	2,00	2,00	minimum pitch [1/1P]		
							Time constant of 1st order filter on pitch angle used for		
37	5,00	1,00	5,00	5,00	1,00	1,00	gain scheduling [1/1P]		
Drivetrain Damper									
							Proportional gain of active DT damper [Nm/(rad/s)], requires		
38	1.800E+07	0,000E+00	1.800E+07	1.800E+07	0,000E+00	0,000E+00	frequency in input 10		
Overspeed									
							Overspeed percentage before initiating turbine controller		
39	1500,00	25,00	10,00	10,00	25,00	25,00	alarm (shut-down) [%]		
Additional non-linear terms									
40	0	0	0	0	0	0	Err0 [rad/s]		
41	0	0	0	0	0	0	ErrDot0 [rad/s^2]		
42	0	0	0	0	0	0	PitNonLin1 [rad/s]		